

Summer 2016

Computational micro-flow with spectral element method and high Reynolds number flow with discontinuous Galerkin Finite Element Method

Haibo Zhang

Follow this and additional works at: <https://digitalcommons.latech.edu/dissertations>

 Part of the [Applied Mathematics Commons](#)

**COMPUTATIONAL MICRO-FLOW WITH SPECTRAL ELEMENT
METHOD AND HIGH REYNOLDS NUMBER FLOW WITH
DISCONTINUOUS GALERKIN FINITE ELEMENT METHOD**

by

Haibo Zhang, B. S., M. S.

A Dissertation Presented in Partial Fulfillment
of the Requirements of the Degree
Doctor of Philosophy

COLLEGE OF ENGINEERING AND SCIENCE
LOUISIANA TECH UNIVERSITY

August 2016

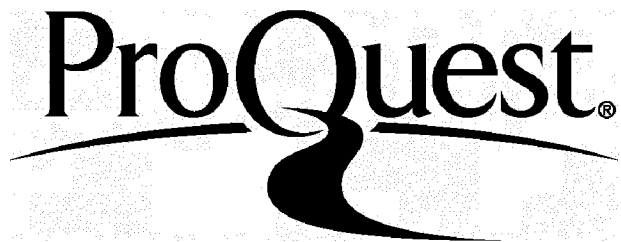
ProQuest Number: 10301617

All rights reserved

INFORMATION TO ALL USERS

The quality of this reproduction is dependent upon the quality of the copy submitted.

In the unlikely event that the author did not send a complete manuscript and there are missing pages, these will be noted. Also, if material had to be removed, a note will indicate the deletion.



ProQuest 10301617

Published by ProQuest LLC(2017). Copyright of the Dissertation is held by the Author.

All rights reserved.

This work is protected against unauthorized copying under Title 17, United States Code.
Microform Edition © ProQuest LLC.

ProQuest LLC
789 East Eisenhower Parkway
P.O. Box 1346
Ann Arbor, MI 48106-1346

LOUISIANA TECH UNIVERSITY

THE GRADUATE SCHOOL

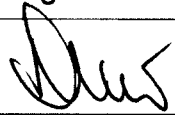
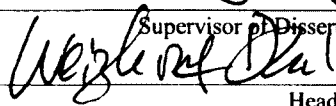
May 19, 2016

Date

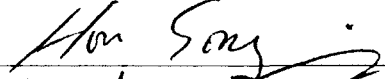
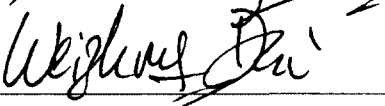

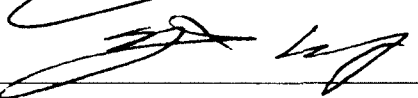
We hereby recommend that the dissertation prepared under our supervision
by Haibo Zhang, M. S.

entitled Computational Micro-Flow with Spectral Element Method and High Reynolds
Number Flow with Discontinuous Galerkin Finite Element Method

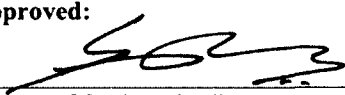
be accepted in partial fulfillment of the requirements for the Degree of
Doctor of Philosophy in Computational Analysis and Modeling

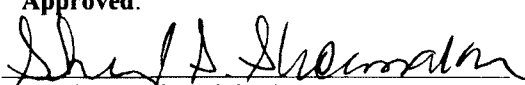

Supervisor of Dissertation Research

Head of Department
Computational Analysis and Modeling
Department

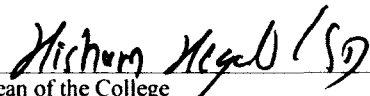
Recommendation concurred in:

Advisory Committee

Approved:

Director of Graduate Studies

Approved:

Dean of the Graduate School


Dean of the College

ABSTRACT

In this dissertation, two numerical methods with high order accuracy, Spectral Element Method (SEM) and Discontinuous Galerkin Finite Element Method (DG-FEM), are chosen to solve problems in Computational Fluid Dynamics (CFD). The merits of these two methods will be discussed and utilized in different kinds of CFD problems. The simulations of the micro-flow systems with complex geometries and physical applications will be presented by SEM. Moreover, the numerical solutions for the Hyperbolic Flow will be obtained by DG-FEM. By solving problems with these two methods, the differences between them will be discussed as well.

Compressible Navier-Stokes equations with Electro-osmosis body force and slip boundary conditions are solved to simulate two independent models. The third order Adams-Bashforth method on time splitting, and up to the eighth order SEM on space analysis are utilized in our cases of the electro-osmosis flow (EOF). To solve the body force caused by EOF, simplification of the Poisson-Boltzmann is discussed in details. Results show that SEM can clearly simulate the electric double layers in EOF. Compared with the finite element method, which uses h-refinement to increase resolution, SEM has obvious advantages by using hp-refinement.

The other case for SEM is the simulations of drug delivery through the micro needle. The drug flowing inside the needle is treated as a micro-flow system with complex geometry, while the process of drug fluxing in human skin is developed as in the

case of CFD problem in porous media. Incompressible Navier-Stokes equations and Darcy-Brinkman equations are solved to simulate the drug flowing inside the needle and diffusing in human skin, respectively. Results are compared with COMSOL simulation, experimental data, and numerical solutions from Smoothed Particle Hydrodynamics (SPH). The high order DG-FEM method is chosen to do research on Hyperbolic Flow.

APPROVAL FOR SCHOLARLY DISSEMINATION

The author grants to the Prescott Memorial Library of Louisiana Tech University the right to reproduce, by appropriate methods, upon request, any or all portions of this Dissertation. It is understood that "proper request" consists of the agreement, on the part of the requesting party, that said reproduction is for his personal use and that subsequent reproduction will not occur without written approval of the author of this Dissertation. Further, any portions of the Dissertation used in books, papers, and other works must be appropriately referenced to this Dissertation.

Finally, the author of this Dissertation reserves the right to publish freely, in the literature, at any time, any or all portions of this Dissertation.

Author Haibo Zhang

Date 8/1/2016

DEDICATION

This is dedicated to my wife, Ying Zhang, our parents, Shulin Zhang, Jianhua Wu, Ruojun Zhang, and Xianzhen Wang, who love me, believe in me, inspire me, and have supported me every step of the way. Without their support and encouragement, I could never have walked this far.

TABLE OF CONTENTS

ABSTRACT.....	iii
DEDICATION.....	vi
LIST OF TABLES.....	x
LIST OF FIGURES.....	xi
NOMENCLATURE.....	xiii
ACKNOWLEDGMENTS.....	xiv
CHAPTER 1 INTRODUCTION.....	1
1.1 Motivation and Background.....	1
1.2 Objectives.....	4
1.3 Outline of Dissertation.....	5
CHAPTER 2 LITERATURE REVIEW.....	6
2.1 Spectral Element Method.....	6
2.1.1 Basis Function.....	8
2.1.2 System Matrices.....	11
2.1.3 Time Splitting.....	14
2.2 Discontinuous Galerkin Finite Element Method.....	14
2.2.1 Numerical Flux.....	16
2.2.2 Basis Functions.....	17
2.2.3 Elemental Matrix.....	18
2.2.4 Time Splitting.....	19

CHAPTER 3 THE NAVIER-STOKES EQUATIONS AND SIMULATIONS OF ENVIRONMENTAL FLOWS	20
3.1 The Navier-Stokes Equations	20
3.2 Simulations with Incompressible Navier-Stokes Equations.....	22
3.2.1 Submerged Cylinder in Rectangular Channel.....	23
3.2.2 A sphere Inside an L-turn Channel	26
CHAPTER 4 ELECTROOSMOTIC DRIVEN MICRO FLOWS	32
4.1 Introduction.....	32
4.2 Methodology	34
4.3 Results and Discussion	39
4.3.1 Grooved-channel.....	41
4.3.2 Curvature-channel.....	45
4.4 Conclusions.....	46
CHAPTER 5 CONTINUOUS AND DISCRETE SIMULATIONS OF MICRO-NEEDLES FOR EPIDERMAL DRUG DELIVERY	48
5.1 Introduction.....	48
5.2 Methodology	50
5.2.1 Continuous Modeling.....	50
5.2.1.1 Part 1: Medicine Liquid Flow through Micro-Needle	51
5.2.1.2 Part 2: Medicine Diffusion Under Skin	52
5.2.2 Discrete Modeling.....	53
5.2.2.1 Drug Particles.....	54
5.2.2.2 Solid Particles	55
5.2.2.3 Particles Interaction	56
5.2.2.4 Velocity Evaluation	56
5.3 Results and Discussion	57

5.3.1	Results for the SEM.....	57
5.3.1.1	Solution for Simulation of Micro-Needle.....	57
5.3.1.2	Solution for Simulation of Human Skin	63
5.3.1.2.1	Single Needle	63
5.3.1.2.2	Multiple Needles	66
5.3.2	Results for SPH.....	68
5.4	Conclusions.....	71
CHAPTER 6 DISCONTINUOUS GALERKIN SIMULATION OF HYPERBOLIC FLOW		73
6.1	Introduction.....	73
6.2	Numerical Methods.....	73
6.2.1	Time Splitting.....	73
6.2.2	Internal Penalty Flux.....	74
6.3	Results and Discussions.....	75
6.3.1	Two-dimensional Simulation of a Low Reynolds Number Flow	75
6.3.2	Three-dimensional Simulation with a Flow with Reynolds Number of 200	77
6.4	Conclusions.....	80
CHAPTER 7 CONCLUSIONS AND FUTURE WORK.....		82
7.1	Conclusions.....	82
7.2	Future Work.....	82
APPENDIX IMPORTANT FUNCTIONS AND LIBRARY		84
BIBLIOGRAPHY.....		97

LIST OF TABLES

Table 1-1: Comparison of the FDM, FEM, SEM, FVM and DG-FEM	4
Table 2-1: Two-dimensional Poisson equation with exact solution of $\sin(xy)$	15
Table 3-1: Heat Capacity Ratio for Some Gases [40, 41].....	22
Table 3-2: The comparison of the numerical solutions with 20,001 time steps	31
Table 4-1: The important subroutines used for solving the compressible Navier-Stokes equations by the SEM	41
Table 5-1: Reference parameters of simulations.....	50
Table 6-1: The maximum velocity (m/s) and pressure (Pa) on cross section of $x = 3$ due to different order of basis function.....	78

LIST OF FIGURES

Figure 2-1: The SEM solution of two-dimensional Helmholtz equation with Dirichlet boundary condition	7
Figure 2-2: The h-convergence test with increasing number of elements	8
Figure 2-3: The Lobatto polynomials as the basis functions of the modal SEM.....	9
Figure 2-4: Mass matrix of Helmholtz equation solving by the nodal SEM	13
Figure 2-5: Stiffness matrix of Helmholtz equation solving by the nodal SEM	13
Figure 2-6: Numerical solution of one-dimensional Burger's equation	16
Figure 2-7: The nodal basis functions in the triangle element.....	18
Figure 3-1: The three-dimensional environment flow in rectangular channel	24
Figure 3-2: The three-dimensional environmental flow: meshes on xz- and yz-cross sections at $y = 0.01$, $x = 0.01$ and $x = 5.01$, respectively	错误!未定义书签。
Figure 3-3: The three-dimensional environmental flow: velocity contour on z-direction in yz-planes of $x = 0.01$, 1.99 , 4.01 , and 5.99	26
Figure 3-4: The three-dimensional environmental flow in a rectangular L-Turn channel	27
Figure 3-5: The mesh of the three-dimensional environmental flow in a rectangular L-Turn channel at xz-cross section on $y = 0.01$	28
Figure 3-6: The velocity on z-direction of a three-dimensional environmental flow in a rectangular L-Turn channel at xz-cross section on $y = 0.01$, 1.01 , and 1.99	29
Figure 3-7: The contours of velocities on x, y, z direction (u, v, w) and the pressure (p) of three-dimensional environmental flow in a rectangular L-Turn channel at xz-cross section on $y = 0.01$	30
Figure 4-1: Normalized Electro-osmotic potential and its related body force on cross section of wall boundary	36
Figure 4-2: Normalized Electro-osmotic potential with opposite values on each side and its related body force on the cross section of wall's boundary	36
Figure 4-3: The SEM simulation: numerical solution of Eq. 4-5	37

Figure 4-4: The lines of the electric field and velocity contour for the model of Grooved-channel on y-direction.	42
Figure 4-5: Velocities track over five history points.	43
Figure 4-6: The SEM simulation: the contours for velocity of y-direction (u), density (Rho), energy (e), and temperature (Temp) at critical area	44
Figure 4-7: Electric field and contour for velocity on y-direction.....	45
Figure 5-1: The models of needles with circular and rectangular cross sections	58
Figure 5-2: The velocity on z direction on xz-cross section.....	59
Figure 5-3: The pressure on xz-cross section	60
Figure 5-4: The contours of velocity on z-direction at the inlet (up) and outlet (down).	61
Figure 5-5: The contours of pressure at the inlet (up) and outlet (down).	62
Figure 5-6: The initial contours of concentration with a different ratio of a needle's input area to the area of x-y cross section of model	64
Figure 5-7: Contour maps for single-needle model at t = 60 sections with different ratios of needle input area to the area of the x-y cross section	65
Figure 5-8: The initial models of human skin with 4 needles	67
Figure 5-9: Contour maps for 4-needle model at t = 60 sections	68
Figure 5-10: The motion process of drug molecules	70
Figure 5-11: The number of particles that has a depth beyond 2000 μm	71
Figure 6-1: The velocity on x-direction at t = 2s	76
Figure 6-2: The velocity on y-direction at t = 2s	76
Figure 6-3: The pressure at t = 2s	77
Figure 6-4: The Three-dimensional model of flow passing a sphere inside a straight channel	79
Figure 6-5: The contours of velocity on the z-direction and its streamline.....	80

NOMENCLATURE

$\mathbf{u} \cdot \mathbf{v}$ or $(\mathbf{u} \cdot \mathbf{v})$ Inner Product or Tensor Product

Ω_{st} Standard Element

Ω_e local Element

$\mathbf{M} \otimes \mathbf{N}$ Tensor Product of Two Matrices

\mathbf{u} velocity vector

$\nabla \mathbf{u}$ Gradient (u_x, u_y, u_z)

$\nabla \cdot \mathbf{u}$ Divergence $u_x + v_y + w_z$

$\nabla \times \mathbf{u}$ Curl of Vector Field \mathbf{u}

\mathbf{n} Unit Normal Vector

Δt Time Step Size

$P_n(x)$ Jacobi Polynomial

$l(x)$ Lagrangian Polynomial

$L(x)$ Legendre Polynomial

f^* Numerical Flux

ACKNOWLEDGMENTS

First of all, I wish to thank my advisor, Dr. Don Liu for leading me into the fantastic world of Applied Mathematics, continually guiding me and giving me knowledge, enthusiasm, and confidence on this road. Without his encouragement and support, I would not have fulfilled my Ph.D. study.

Special thanks to my committee: Dr. Weizhong Dai, Dr. Songming Hou, Dr. Box Leangsuksun, and Dr. Shengnian Wang, as well as all others in COES of Louisiana Tech University for their precious advice and kind help.

I am grateful to my beloved families for their sacrifice and their love. They have supported me throughout these years. I also want to take this opportunity to thank all my colleagues and friends: Wenyuan Ma and Yifan Wang, whom I have been working with closely and have built a deep friendship.

My Ph.D. study is supported by grants to Dr. Don Liu from National Science Foundation (DMS-1115546, DMS-1318988, NSF/LEQSF(2010-13)-Track-2-LSU). The computational resources were provided by XSEDE (which is supported by National Science Foundation grant ACI-1053575), Louisiana Optical Network Initiative, and High-Performance Computing at Louisiana State University.

CHAPTER 1

INTRODUCTION

1.1 Motivation and Background

The errors in numerical methods are defined by two sources: round-off error and truncation error. Since round-off error is generated by computer rounding of decimal quantities, it happens to all computer based numerical analysis. Moreover, truncation error is the difference between the numerical solution of partial differential equations (PDEs) and their exact quantities. To reduce this truncation error and get a higher order of accuracy, there are three main approaches: h-refinement, p-refinement, and hp-refinement. The h-refinement stands for introducing more elements while fixing the order of interpolating polynomials. As an alternative, the p-refinement [1] stands for increasing the order of the basis functions and keeping the number of sub domains. Then by combining the advantages of both refinements, an hp-version of the finite element is implemented by [2]. In this version, the number of elements and order of the basis functions can be increased simultaneously.

There are many numerical methods that can be used to solve problems of computational fluid dynamics. The Finite Difference Method (FDM), one of an h-refinement method, is treated as the dominant approach to get the numerical solution for PDEs [3]. Deriving from Taylor's polynomial, FDM is efficient to obtain a high resolution scheme by requiring a larger number of elements. Moreover, the Compact

Finite Difference Method (CFDM) [4-7] is frequently chosen to solve problems based on Navier-Stokes equations, and hyperbolic equations as well. The first order accuracy can be obtained by both forward and backward difference formulae, and the second order of accuracy can be achieved by the central difference formulae.

The Finite Element Method (FEM), developed from the variation method, is also a kind of h-refinement method. The merits of FEM are discussed in [8, 9] as: Flexibility for complex geometry and physics, suitable for materials with different properties, clear representation of whole simulation and critical areas. This method was first introduced to CFD problems in the 1970s [10, 11]. Till now, it becomes a basic algorithm for most of the numerical simulation software such as COMSOL and ANSYS. However, FEM is limited by its availability in h-refinement. To achieve higher resolution, the mesh of the model needs to be refined, that is to say, more elements will be introduced to critical areas.

Besides methods of h-convergence, spectral method, a formulation of h-version, was developed by [1] in 1977. In this method, the tensor product of one-dimensional discretizations in different coordinate axes is formulated to build matrices for multi-dimensional simulations. Then this method was introduced to CFD in 1988 [12] by Canuto et al. Simultaneously, four years before Canuto's research, Patera [13] in his paper illustrated the Spectral Element Method (SEM). In [14-16], the numerical solution of the Navier-Stokes equations is stated in detail. Compared with the FEM, the SEM spans tensor product space by nodal basis functions supporting inside elements associated with Gauss-Lobatto points. Because of these zero points on both ends of the integration domain, it will be much easier for SEM to impose boundary conditions. Due to its high

performances in simulations of complex geometries and physics, SEM becomes a popular choice for numerical analysis of CFD [17-20].

However, the SEM has its limitation. In [21], it claims that due to the lack of upwind treatment, the SEM may carry out unstable results for strong hyperbolic problems. In this situation, the Finite Volume Method (FVM) [22], a formulation with close relation to FDM, is introduced. This method provides a good way to deal with strong advection problems, meanwhile, retains flexibility for complex geometries. In FVM, it images the numerical flux entering the volume surrounding each nodal point on the mesh identically leaving its contiguous volume. So the FVM is conservative, and integrates the solution by the cell's average. Nevertheless, this method is still short of high-order accuracy and hp-adaptivity. This drawback had continuously remained, until a genius opinion about the combination of the FEM and the FVM came out. In [23-27], Discontinuous Galerkin Finite Element Method (DG-FEM) is created to satisfy the requirement of high-order accuracy as well as the flux similar to the FVM. The **Table 1-1** shows the overall comparison of those methods mentioned in this section. A "Y" mark means the method is suitable for holding such kind of models, while an "N" mark stands for a short-coming, and an "NF" indicates that the method, with some adjustment, can solve these problems, but when compared with the other methods on the list, it is not for the first choice.

Table 1-1: Comparison of the FDM, FEM, SEM, FVM and DG-FEM.

	Complex Geometries	Complex Physics	High-order Accuracy	Explicit semi-discrete form	Conservation Laws	Elliptic Problems
FDM	N	Y	Y	Y	Y	Y
FEM	Y	Y	Y	N	NF	Y
FVM	Y	Y	N	Y	Y	NF
SEM	Y	Y	Y	Y	NF	Y
DG-FEM	Y	Y	Y	Y	Y	NF

1.2 Objectives

The objective of this dissertation is to solve some CFD problems using the SEM and the DG-FEM. Based on our self-generated codes, the main goals are indicated in details by the following:

1. Show the accuracy of our codes. By comparison our numerical solution with exact solution or solution from the published paper, the accuracy of our codes will be proved.
2. Implement the miu-flow code with complex geometries. The compressible Navier-Stokes equations with Electroosmosis body force will be solved in complex geometries.
3. Provide the numerical simulation of the Micro-needle with the SEM. The model of the Micro-needle will be built and simulated by solving Navier-Stokes equations with slip boundary conditions and Darcy-Brinkman

equations. The results will be compared with the one from COMSOL and the Smoothed Particle Hydrodynamics method.

4. Illustrate the advantages and drawbacks of the DG-FEM. The numerical solution of a particular model of CFD problem will be compared with the SEM.

1.3 Outline of Dissertation

The Chapter 1 introduces the motivation and some overall background knowledge of this research work. The research goal and the structure of this dissertation are indicated. The Chapter 2 gives a brief literature review covering the background required for this dissertation: the SEM and the DG-FEM. The Chapter 3 gives two three-dimensional cases of the environmental flow presented to show the high order accuracy of the SEM for solving the Navier-Stokes equations. The Chapter 4 describes the modeling of electroosmotic flow by the SEM. Here, the slip boundary condition and body force caused by electrical potential are imposed to the two-dimensional Navier-Stokes equations. The Chapter 5 describes a three-dimensional simulation of medical application. The result is compared with the reference data and our discrete modeling. The Chapter 6 gives simulation of the CFD problems with high Reynolds number. the DG-FEM scheme is chosen and discussed. The Chapter 7 concludes the results of the dissertation, and recommends some future works.

CHAPTER 2

LITERATURE REVIEW

2.1 Spectral Element Method

In 1984, the SEM was first introduced by [13], who combined the generality of the FEM with h-refinement with the high order accuracy of the spectral method to solve Laminar flow in a channel expansion, and further developed into the CFD problems by [15, 28-32].

Since the SEM is an hp-refinement approach, the convergence of simulation can either be achieved by introducing finer meshes or by increasing the polynomial order of the basis functions. **Figure 2-1** is the 15th order accurate numerical solution of two-dimensional Helmholtz equation with Dirichlet boundary condition. The original equation is set as $U_{xx} + U_{yy} + U = f$, and the exact solution is $U = e^{\cos(x) + \cos(y)}$.

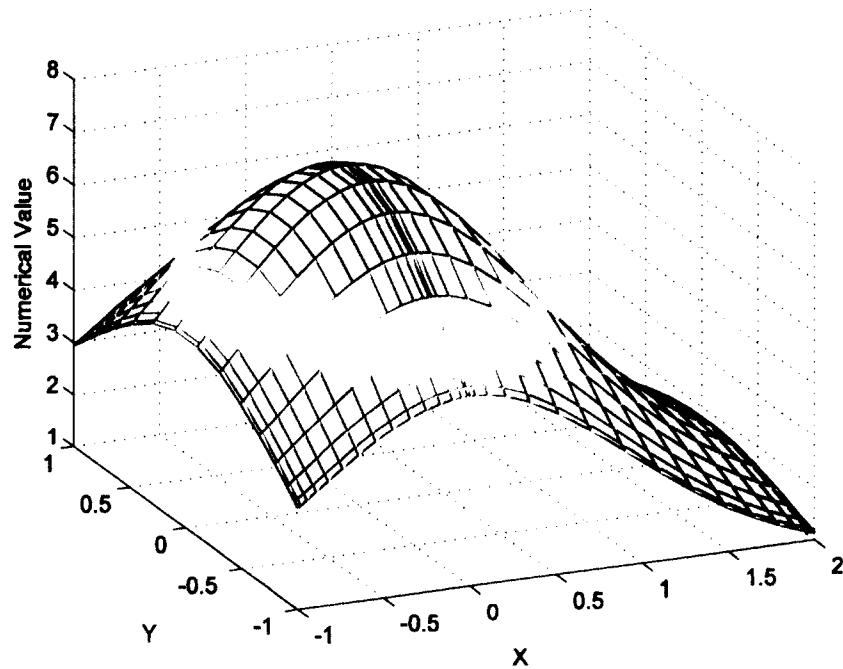


Figure 2-1: The SEM solution of two-dimensional Helmholtz equation with Dirichlet boundary condition.

Figure 2-2 is the log-scale of L2 error of Helmholtz equation with p-refinement and h-refinement, respectively. From this figure, it seems that, due to the round-off error, when the order of the basis functions increases to eight and higher, the accumulated error will not decrease any more. At the same time, it shows that the results get convergent faster in the way of p-refinement than h-refinement. Moreover, from the line of 20 elements, we can find that the more elements we have, the accuracy limitation due to the round-off error will show earlier. In the case with five elements, the log-scale of L2 error will not reduce until the 11th order of Legendre polynomials; however, when the number of elements increases to 20, the convergent result appears at

the fifth polynomial order.

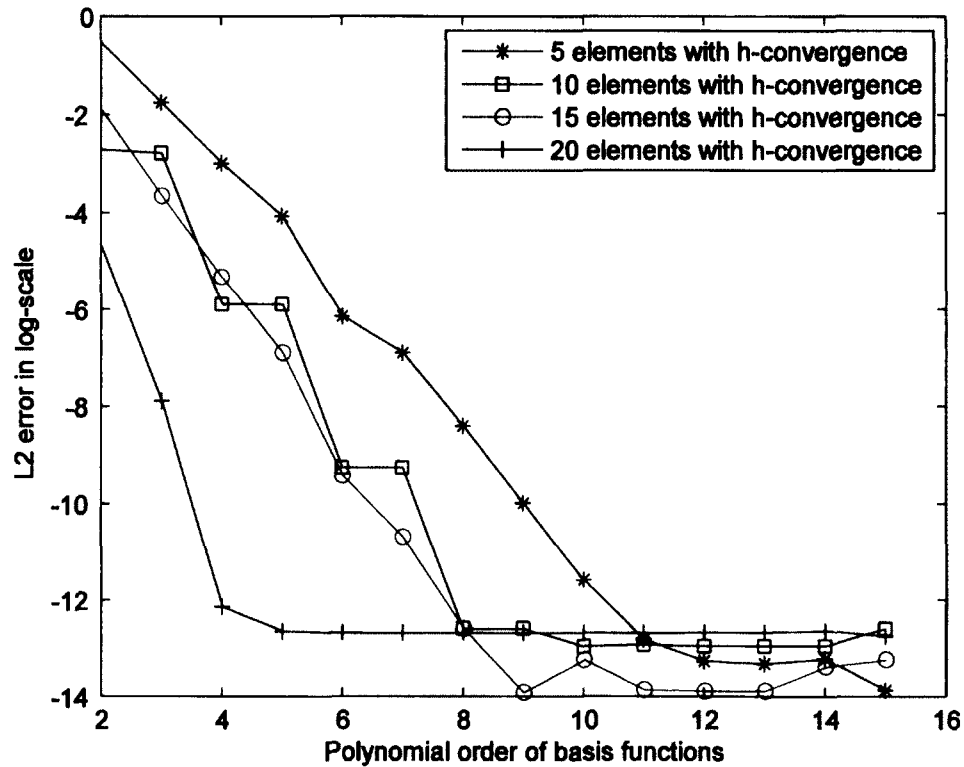


Figure 2-2: The h-convergence test with increasing number of elements.

2.1.1 Basis Function

There are two types of basis function in the SEM – the modal basis and the nodal basis. Unlike the modal SEM, which is based on the Lobatto polynomials, the Lagrange polynomials associated with the Gauss-Lobatto-Legendre or Chebyshev quadrature nodes are defined as the basis functions of the nodal SEM [33]. The solutions that come from the modal scheme is the summation of polynomials multiplied by the modal coefficients. Moreover, for nodal scheme, the solutions are directly defined on multiple nodes. That is to say, the solution can be immediately obtained by multiplying the right hand side of the

equation by the inverse of the system matrix. The basis functions of the modal SEM are shown in **Figure 2-3** as an example.

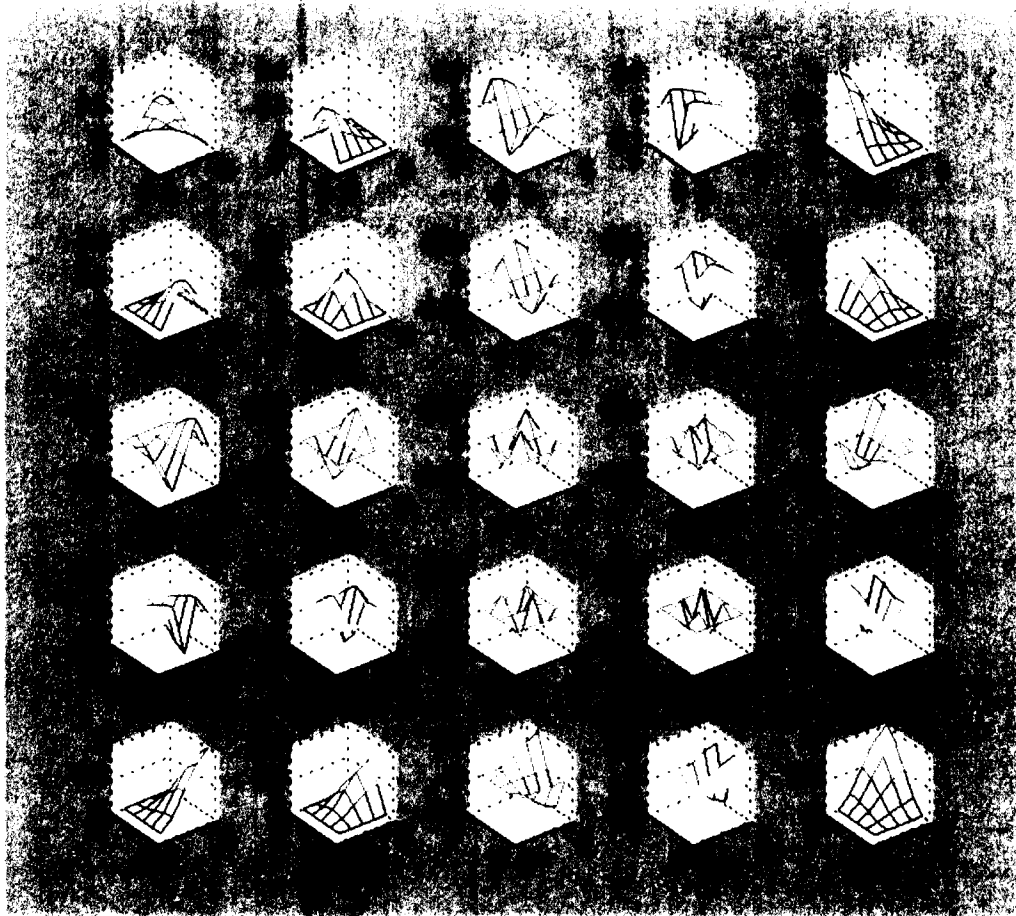


Figure 2-3: The Lobatto polynomials as the basis functions of the modal SEM.

For the modal basis, the n^{th} order Jacobi polynomial is represented by:

$$P_n^{\alpha,\beta}(x) = \frac{(-1)^n}{2^n n!} (1-x)^{-\alpha} (1+x)^{-\beta} \frac{d^n}{dx^n} [(1-x)^{\alpha+n} (1+x)^{\beta+n}] \quad \text{Eq. 2-1}$$

$$\alpha, \beta > -1,$$

then for the Legendre polynomial ($\alpha = \beta = 0$) $\rightarrow L_n(x) = P_n^{0,0}$, and for the Chebychev

polynomial ($\alpha = \beta = -\frac{1}{2}$) $\rightarrow T_n(x) = \frac{2^{2n}(n!)^2}{(2n)!} P_n^{-\frac{1}{2},-\frac{1}{2}}(x)$.

For the nodal basis, the n^{th} order of Lagrange polynomial ($\alpha = \beta = 0$) is represented by:

$$h_j(x) = \begin{cases} \frac{P_n^{\alpha,\beta}(x)}{[P_n^{\alpha,\beta}(x_j)]'(x-x_j)} & \text{when } x \neq x_j \\ 1 & \text{when } x = x_j \end{cases} \quad \text{Eq. 2-2}$$

In my research, the nodal SEM is chosen with Legendre polynomials. The recursion relation between Jacoby polynomials of different orders is indicated as below, and the Matlab code for this part is shown in Appendix A.

$$\begin{aligned} P_0^{\alpha,\beta}(x) &= 1, \\ P_1^{\alpha,\beta}(x) &= \frac{1}{2}[\alpha - \beta + (\alpha + \beta + 2)x], \\ a_n^1 P_{n+1}^{\alpha,\beta}(x) &= (a_n^2 + a_n^3 x)P_n^{\alpha,\beta}(x) - a_n^4 P_{n-1}^{\alpha,\beta}(x), \\ a_n^1 &= 2(n+1)(n+\alpha+\beta+1)(2n+\alpha+\beta), \\ a_n^2 &= (2n+\alpha+\beta+1)(\alpha^2 - \beta^2), \\ a_n^3 &= (2n+\alpha+\beta)(2n+\alpha+\beta+1)(2n+\alpha+\beta+2), \\ a_n^4 &= 2(n+\alpha)(n+\beta)(2n+\alpha+\beta+2). \end{aligned} \quad \text{Eq. 2-3}$$

Simultaneously, the first derivative of $P_n^{\alpha,\beta}(x_j)$ is achieved as the following, and the Matlab code is shown in Appendix B.

$$\begin{aligned} b_n^1(x) [P_n^{\alpha,\beta}(x)]' &= b_n^2(x) P_n^{\alpha,\beta}(x) + b_n^3(x) P_{n-1}^{\alpha,\beta}(x) \\ b_n^1(x) &= (2n+\alpha+\beta)(1-x^2) \\ b_n^2(x) &= n[\alpha - \beta - (2n+\alpha+\beta)x] \\ b_n^3(x) &= 2(n+\alpha)(n+\beta). \end{aligned} \quad \text{Eq. 2-4}$$

In Eq. 2-2, we suppose that $P_n(x)$ is the polynomial of order n with zeros at the $(n+1)$ nodal points x_j ($j = 0, \dots, n-1$). The zeros-finding algorithm is applied to the equation:

$$\frac{f_{n-m}(x)}{f'_{n-m}(x)} = \frac{P_n^{\alpha,\beta}(x)}{[P_n^{\alpha,\beta}(x)]' - P_n^{\alpha,\beta}(x) \sum_{i=0}^{m-1} [1/(x-x_i)]}. \quad \text{Eq. 2-4}$$

The Matlab code for **Eq. 2-4** is shown in Appendix C. Moreover, since the Gauss-Lobatto integration requires the nodal points including both ends of the integration interval, which means that for the standard interval (the values of x are defined between -1 to 1), the points $x = \pm 1$ will be included. So, the zeros points and weights for Gauss-Lobatto-Jacobi formulae are described in **Eq. 2-5** and **Eq. 2-6**, respectively:

$$x_i = \begin{cases} -1 & i = 0 \\ x_{i-1,Q-2}^{\alpha+1,\beta+1} & i = 1, \dots, Q-2, \\ 1 & i = Q-1 \end{cases} \quad \text{Eq. 2-5}$$

$$\omega_i^{\alpha,\beta} = \begin{cases} (\beta+1)C_{0,Q-2}^{\alpha+\beta} & i = 0 \\ C_{i,Q-2}^{\alpha,\beta} & i = 1, \dots, Q-2. \\ (\alpha+1)C_{Q-1,Q-2}^{\alpha,\beta} & i = Q-1 \end{cases} \quad \text{Eq. 2-6}$$

The $C_{i,Q-2}^{\alpha,\beta}$ is determined by:

$$C_{i,Q-2}^{\alpha,\beta} = \frac{2^{\alpha+\beta+1} \Gamma(\alpha+Q) \Gamma(\beta+Q)}{(Q-1)(Q-1)! \Gamma(\alpha+\beta+Q+1) [P_{Q-1}^{\alpha,\beta}(x_i)]^2}. \quad \text{Eq. 2-7}$$

Meanwhile, the Matlab code for zeros and weights are shown in Appendix the subroutines GLJzp.m and GLJwe.m. When all the zeros and weights are calculated, the two-dimensional and three-dimensional cases are implemented by the inner product of one-dimensional Legendre polynomial in standard interval.

2.1.2 System Matrices

In the last section, we briefly described how to generate the basis functions, zeros and weights in the SEM. Now we need to analyze the procedures of building mass and stiffness matrices.

Let us take two-dimensional case as an example. The tensor product of two one-dimensional Lagrangian $h(\xi)$ and $h(\eta)$ will be used to present as the basis functions of a single element. The local mass matrix is calculated as **Eq. 2-8**:

$$\begin{aligned}
 M^e[i][j] &= (\Phi_i, \Phi_j)_{\Omega_e} = \int_{\Omega_{st}} l_i(\xi, \eta) l_j(\xi, \eta) d\xi d\eta \\
 &\approx \sum_{k=0}^n \left[\omega_k \sum_{i=0}^n h_i(\xi_k) \sum_{j=0}^n h_j(\xi_k) J_{\xi,k} \right] \otimes \sum_{k=0}^n \left[\omega_k \sum_{i=0}^n h_i(\eta_k) \sum_{j=0}^n h_j(\eta_k) J_{\eta,k} \right] \quad \text{Eq. 2-8} \\
 &= \left[\sum_{j=0}^n \sum_{i=0}^n \left(\sum_{k=0}^n \omega_k \delta_{ik} \delta_{jk} J_{\xi,k} \right) \right] \otimes \left[\sum_{j=0}^n \sum_{i=0}^n \left(\sum_{k=0}^n \omega_k \delta_{ik} \delta_{jk} J_{\eta,k} \right) \right],
 \end{aligned}$$

in which the diagonal mass matrix of two-element 15th order Helmholtz case is taken as an example shown in **Figure 2-4**: Mass matrix of Helmholtz equation solving by the nodal SEM. M^e is the elemental mass matrix, Ω_e is the elemental region, $u(\Phi_p, \Phi_q)$ is the inner product of two one-dimensional basis, ξ and η are the values of x and y from an arbitrary element project to the standard quadrilateral element. The local stiffness matrix is generated as **Eq. 2-9**:

$$\begin{aligned}
 L^e[i][j] &= (\Phi_i, \Phi_j)_{\Omega_e} = \int_{\Omega_{st}} l'_i(\xi, \eta) l'_j(\xi, \eta) d\xi d\eta \\
 &\approx \sum_{k=0}^n \left[\omega_k \sum_{i=0}^n h'_i(\xi_k) \sum_{j=0}^n h'_j(\xi_k) J_{\xi,k} \right] \sum_{k=0}^n \left[\omega_k \sum_{i=0}^n h'_i(\eta_k) \sum_{j=0}^n h'_j(\eta_k) J_{\eta,k} \right]. \quad \text{Eq. 2-9}
 \end{aligned}$$

Based on the equations from **Eq. 2-1** to **Eq. 2-9**, the stiffness matrix, which is shown as a diagonal matrix, and the mass matrix, which in the SEM is presented as a symmetric

matrix can be obtained. The stiffness matrix from the same case as **Figure 2-4** is shown in **Figure 2-5**.

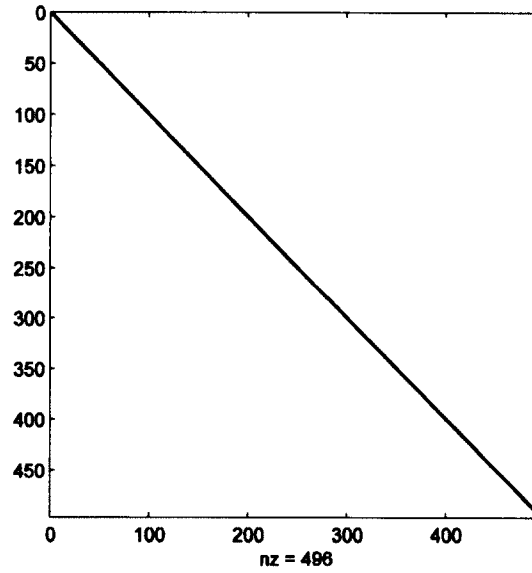


Figure 2-4: Mass matrix of Helmholtz equation solving by the nodal SEM.

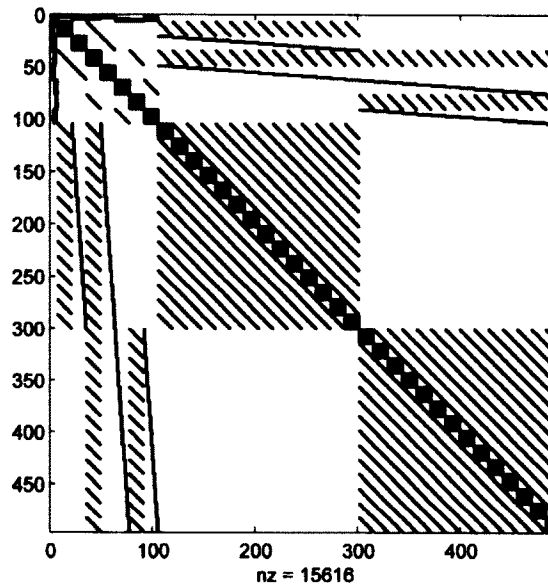


Figure 2-5: Stiffness matrix of Helmholtz equation solving by the nodal SEM.

2.1.3 Time Splitting

The Adams-Bashforth method is used for time splitting. Before the third time step, the first and the second order Adams-Bashforth method are implemented, and after that the third order scheme is fixed for time integration.

When the time step = 1, the first order Adams-Bashforth Method (Euler Method) is carried out:

$$y_{n+1} = y_n + hf(t_n, y_n). \quad \text{Eq. 2-10}$$

When the time step = 2, the second order Adams-Bashforth Method is used:

$$y_{n+2} = y_{n+1} + h \left[\frac{3}{2}f(t_{n+1}, y_{n+1}) - \frac{1}{2}f(t_n, y_n) \right]. \quad \text{Eq. 2-11}$$

When the time step is larger than 2, the third order is implemented:

$$y_{n+3} = y_{n+2} + h \left[\frac{23}{12}f(t_{n+2}, y_{n+2}) - \frac{4}{3}f(t_{n+1}, y_{n+1}) + \frac{5}{12}f(t_n, y_n) \right]. \quad \text{Eq. 2-12}$$

2.2 Discontinuous Galerkin Finite Element Method

In these problems of which the convection plays a role of importance, such as aero acoustics, water jet flow, weather forecasting and gas dynamics, the SEM becomes less efficient for the reasons that the discontinuities appear in the exact solutions of the convective problems; meanwhile, the numerical solutions near these discontinuities might show a rich and complicated structure [34]. To overcome this challenge, a numerical method with the requirement of physically relevant discontinuities in the approximate solutions, and guarantee of avoiding spurious oscillations, as well as maintenance of sufficient accuracy is introduced and named as the Discontinuous Galerkin Finite Element Method (DG-FEM). The DG-FEM incorporates the numerical flux, filter and slope limiter from the FEM and the FVM into the FEM framework [35-37]. With the

combination of the FDM, the FVM and the FEM, it is capable of the following merits: firstly, this method is an hp-refinement scheme. Moreover, it is highly parallelizable due to the block diagonal of the mass matrix. Thirdly, the DG-FEM can deal with models of complex geometries with simple treatment of the boundary conditions.

Table 2-1 shows the cumulative error of hp-convergence of Poisson equation with L^2 log scale, in which k is the polynomial order, N is the number of element.

Table 2-1: Two-dimensional Poisson equation with exact solution of $\sin(xy)$.

$N \backslash k$	5	10	20	30	40
3	-2.3903	-3.2204	-4.0911	-4.6239	-5.0125
4	-3.5533	-4.9640	-6.3292	-7.1225	-7.6847
5	-4.7104	-6.1254	-7.5692	-8.4348	-9.0595
6	-6.0874	-8.1074	-10.0774	-11.2142	-11.5642
7	-7.3647	-9.3716	-11.3097	-11.5255	-11.0523
8	-8.8821	-11.4950	-12.1599	-12.0845	-11.1563
9	-10.2532	-12.3747	-11.4703	-11.0284	-11.1151

After the hp-analysis of Poisson equation, the one-dimensional Burger's equation:

$$\frac{\partial y}{\partial t} + \frac{\partial}{\partial x}(y^2) = 0, \quad x \in [-1, 1],$$

with the CFL = 0.25 and the discontinuous initial condition:

$$y_0(x) = y(x, 0) = \begin{cases} 2, & x \leq -0.5 \\ 0, & x > -0.5 \end{cases}$$

The solution from the fifth order nodal DG-FEM with 40 elements is shown in **Figure 2-6** below.

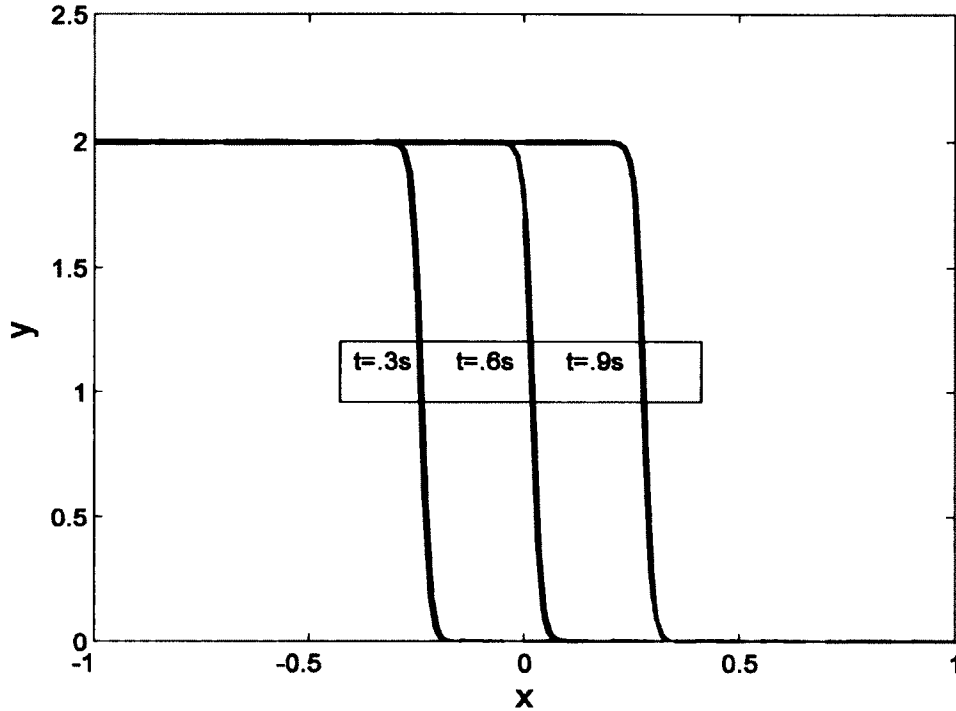


Figure 2-6: Numerical solution of one-dimensional Burger's equation.

2.2.1 Numerical Flux

The numerical flux f^* is highly related to the accuracy of simulations of purely convective fluids. **Eq. 2-13** gives its expression:

$$f^* = (au)^* = \{\{au\}\} + |a| \frac{1-\alpha}{2} \llbracket u \rrbracket, \quad \text{Eq. 2-13}$$

in which a is a parameter to reflect the boundary conditions. In the case of $a > 0$, the left side flux is $f_L = 0$ and the right side flux is $f_R = au_h(x_r^K)$. When $a < 0$, we have $f_L = -au_h^1(x_l^1)$ and $f_R = au_h(x_r^K)$. The α is defined in the interval $[0,1]$. If $\alpha = 0$, the flux only takes information from its upwind, and if $\alpha = 1$, the flux is the arithmetic

average of the two solutions. The $\{\{au\}\} = a \frac{u^- + u^+}{2}$ is the average of the interior (u^-) and exterior (u^+) information of the local solution. The jump along a normal, $\hat{\mathbf{n}}$, is defined as $[[u]] = \hat{\mathbf{n}}^- u^- + \hat{\mathbf{n}}^+ u^+$.

2.2.2 Basis Functions

The same as the SEM, there are also the nodal and modal DG-FEM. In this dissertation, the nodal DG-FEM is chosen. According to [37], in the triangle scheme, the nodal basis functions are built with the assistance of the modal bases. First of all, for an element of arbitrary triangle, a group of points with equal space will be projected to the isosceles' right triangle with Eq. 2-14:

$$(\lambda_1, \lambda_3) = \left(\frac{i}{N}, \frac{j}{N} \right), \lambda_2 = 1 - \lambda_1 - \lambda_3, (i, j) \geq 0, i + j \leq N, \quad \text{Eq. 2-14}$$

$$\begin{pmatrix} r \\ s \end{pmatrix} = \lambda_2 \begin{pmatrix} -1 \\ -1 \end{pmatrix} + \lambda_3 \begin{pmatrix} 1 \\ -1 \end{pmatrix} + \lambda_1 \begin{pmatrix} -1 \\ 1 \end{pmatrix}.$$

Then the Lagrangian polynomial $l(r, s)$ is constructed from the modal bases $\Phi(r, s)$ through the Vandermonder matrix \mathbf{V} , according to Eq. 2-15:

$$V_{ij} = \Phi_{j-1}(r, s)_i, \quad \text{Eq. 2-15}$$

$$\mathbf{V}^T l(r, s) = \Phi(r, s),$$

in which, $a = 2 \frac{1+r}{1-s} - 1$, $b = s$; r and s are the coordinates of the two right-angle sides,

and the Jacobi polynomial $\Phi_n(r, s)$ is calculated by Eq. 2-16:

$$\Phi_n(r, s) = \sqrt{2} P_i^{\alpha, \beta}(a) P_j^{2i+1, 0}(b) (1-b)^i. \quad \text{Eq. 2-16}$$

The nodal basis functions are shown in Figure 2-7[21].

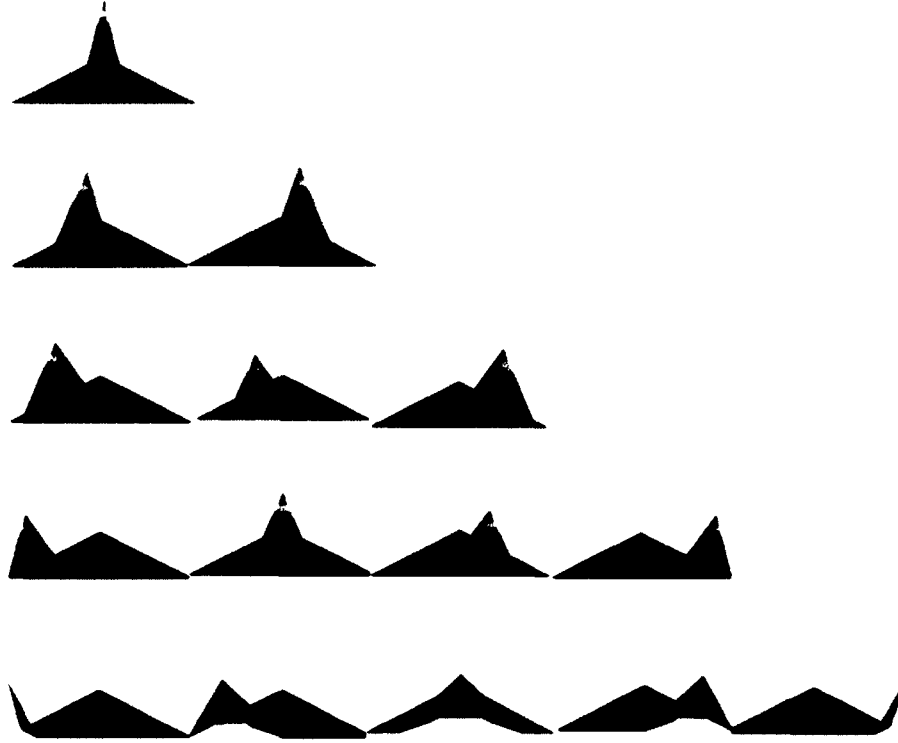


Figure 2-7: The nodal basis functions in the triangle element.

2.2.3 Elemental Matrix

The local mass matrix is generated as:

$$\begin{aligned}
 \mathbf{M} &= (\Phi_i(r, s), \Phi_j(r, s))_{\Omega_e} = \int_{\Omega_{st}} l_i(\xi, \eta) l_j(\xi, \eta) J \, d\xi d\eta \\
 &\approx \sum_{k=0}^N \left[w_k \left(\sum_{i=0}^N h_i(\xi_k) \sum_{j=0}^N h_j(\xi_k) \right) J_{\xi, \eta} \right] \otimes \sum_{k=0}^N \left[w_k \left(\sum_{i=0}^N h_i(\eta_k) \sum_{j=0}^N h_j(\eta_k) \right) J_{\eta, k} \right] \quad \text{Eq. 2-17} \\
 &= \left\{ \sum_{j=0}^N \sum_{i=0}^N \left[\sum_{k=0}^N w_k \delta_{ik} \delta_{jk} J_{\xi, k} \right] \right\} \otimes \left\{ \sum_{j=0}^N \sum_{i=0}^N \left[\sum_{k=0}^N w_k \delta_{ik} \delta_{jk} J_{\eta, k} \right] \right\}.
 \end{aligned}$$

2.2.4 Time splitting

The Low-storage Runge-Kutta scheme [38, 39] is chosen for the time integration.

The coefficients are shown as below [37]:

$$\text{rk4a} = [0.0, -0.417890, -1.192152, -1.697785, 1.514183],$$

$$\text{rk4b} = [0.149659, 0.379210, 0.822955, 0.699450, 0.153057],$$

$$\text{rk4c} = [0.0, 0.149659, 0.370401, 0.622256, 0.958282].$$

CHAPTER 3

THE NAVIER-STOKES EQUATIONS

AND SIMULATIONS OF ENVIRONMENTAL FLOWS

3.1 The Navier-Stokes Equations

In this chapter, the Navier-Stokes equations are solved to simulate the cases of environmental flows. The Navier-Stokes equations, which are named after Claude-Louis Navier and George Gabriel Stokes, describe many physical phenomena in the computational fluid dynamics, such as the ocean current, air flows, and water in a specific channel. The Navier-Stokes equations are defined with varieties of boundary and initial conditions, unknown variables and body forces.

For the incompressible flow, the Navier-Stokes equations are shown as follows.

The Momentum equation:

$$\rho \left(\frac{\partial \mathbf{u}}{\partial t} + (\mathbf{u} \cdot \nabla) \mathbf{u} \right) = -\nabla p + \mu \nabla^2 \mathbf{u} + \mathbf{f}, \quad \text{Eq. 3-1}$$

with the Continuity equation:

$$\nabla \cdot \mathbf{u} = 0, \text{ on } \partial\Omega. \quad \text{Eq. 3-2}$$

For the compressible flow, the Navier-Stokes equations are shown below.

The Momentum equation:

$$\frac{\partial}{\partial t} (\rho \mathbf{u}) + \rho \mathbf{u} \cdot \nabla \mathbf{u} = -\nabla p + \mu \nabla^2 (\mathbf{u}) + \mathbf{f}, \quad \text{Eq. 3-3}$$

with the Continuity equation:

$$\frac{\partial \rho}{\partial t} + \nabla \cdot (\rho \mathbf{u}) = 0. \quad \text{Eq. 3-4}$$

Meanwhile, if the energy conservation needs to be considered, then the Energy equation (Eq. 3-5) is shown:

$$\frac{\partial E}{\partial t} + \nabla \cdot (E\mathbf{u} - \sigma\mathbf{u} + \mathbf{q}) = \mathbf{f} \cdot \mathbf{u}, \quad \text{Eq. 3-5}$$

where \mathbf{f} is the external force defined by different nodes, σ is the stress tensor determined by Eq. 3-6, and \mathbf{q} is the heat flux vector calculated by Eq. 3-7 as follows:

$$\sigma = -p\mathbf{I} + \mu[\nabla\mathbf{u} + (\nabla\mathbf{u})^T] + \zeta(\nabla \cdot \mathbf{u})\mathbf{I}, \quad \text{Eq. 3-6}$$

$$\mathbf{q} = -k\nabla T, \quad \text{Eq. 3-7}$$

where \mathbf{I} is the unit tensor, k is the thermal conductivity, which is actually a tensor of a function of the temperature T . Moreover, the part of the second coefficient of viscosity ζ is determined by the Stokes hypothesis: $2\mu + 3\zeta = 0$.

Taking the two-dimensional compressible Navier-Stokes equations with Energy equation, which is an equation set of Eq. 3-3, Eq. 3-4 and Eq. 3-5, as an example, there are four equations with six unknown variables: $\mathbf{u}(x, y)$, p , ρ , E , and T . So the compressible fluid is treated as the ideal gas, the energy is re-written in the form of $E = \frac{p}{\gamma-1} + \frac{\rho}{2} \mathbf{u} \cdot \mathbf{u}$, and the pressure is calculated as: $p = \rho RT$. R is the ideal gas constant, the ratio of specific heats $\gamma = \frac{c_p}{c_r}$, the c_p and c_r are the specific heat capacity with constant pressure and volume conditions respectively. Simultaneously, the heat capacity ratios for some gases are shown in **Table 3-1**.

Table 3-1: Heat Capacity Ratio for Some Gases [40, 41].

Temp(°C)	Gas	γ	Temp(°C)	Gas	γ
20	H ₂	1.410	0	Dry Air	1.403
100		1.404	20		1.400
400		1.387	100		1.401
20	He	1.660	200		1.398
20	H ₂ O	1.330	400		1.393
100		1.324	1000		1.365
200		1.310	2000		1.088
-181	O ₂	1.450	0	CO ₂	1.310
-76		1.415	20		1.300
20		1.400	100		1.281
100		1.399	400		1.235
200		1.397	1000		1.195
400		1.394	CH ₄	20	1.410

3.2 Simulations with Incompressible Navier-Stokes Equations

In this section, two models of flows in the channels of complex geometries are presented to show the numerical solutions of Navier-Stokes equations without body force and slip boundary conditions. The first simulation shows the fluid goes through a rectangular channel with a submerged cylinder inside. And the second model shows the water flows inside a L-turn channel.

3.2.1 Submerged Cylinder in Rectangular Channel

The first example is a submerged cylinder in a rectangular channel. This is the model built as simulation cases try to publish in [19]. The dimensionless sizes of the models are set as $[-3, 3]$, $[-3, 3]$, and $[-4, 10]$ on x , y , z direction, respectively; the radius of the cylinder is 1.0. The model has the element number of 1928, and polynomial order of four with the periodic boundary condition on $y = \pm 3.0$, the wall's boundary condition on the cylinder's surface, and the v boundary condition on $x = \pm 3.0$, the xy -crosssection at $z = -4.0$ is set as the inlet with the Reynolds number of 20, the scaled density ρ and dynamic viscosity μ equal to 1, non-driven force and the initial velocity on z -direction from 10.0 linearly decreasing to 0.0 along the top to the bottom of the x -direction, and the xy -plane at $z = 10.0$ is set as the outlet with a Neumann boundary condition of $\frac{\partial w}{\partial z} = 0$.

The model is shown in **Figure 3-1**, in which the mesh is divided into eleven blocks: two at the inlet and outlet presented as dark blue and orange, respectively, four around the cylinder, and five on top of the cylinder. **Figure 3-2** shows the slices of mesh, and **Figure 3-3** shows the contour of the velocity on z -direction in different layers.

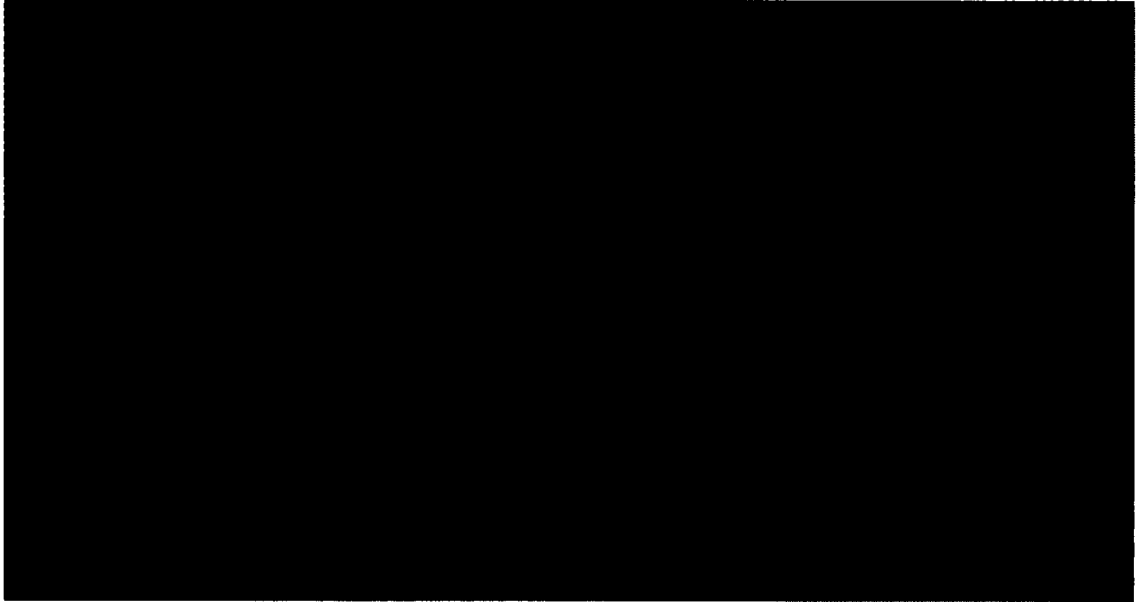
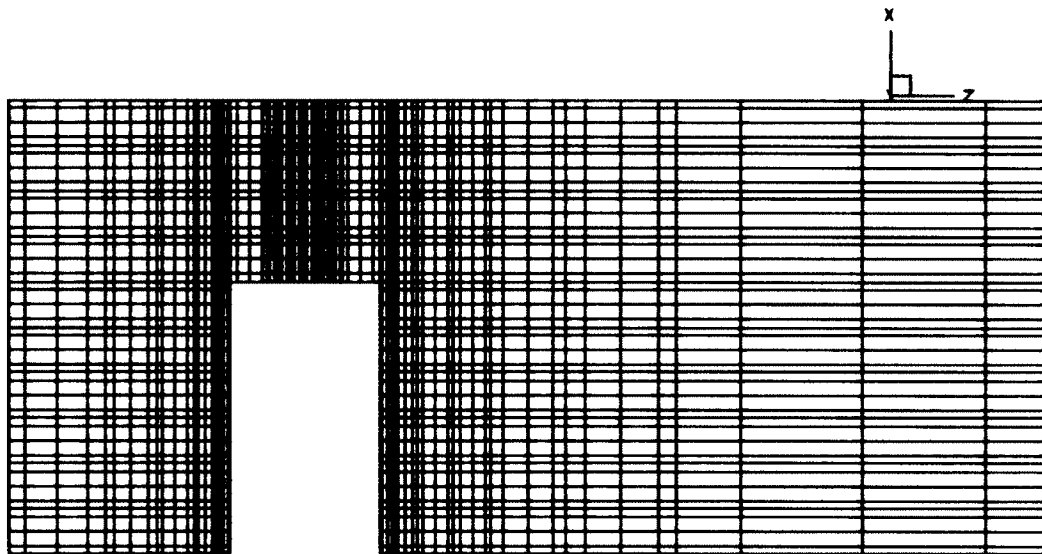
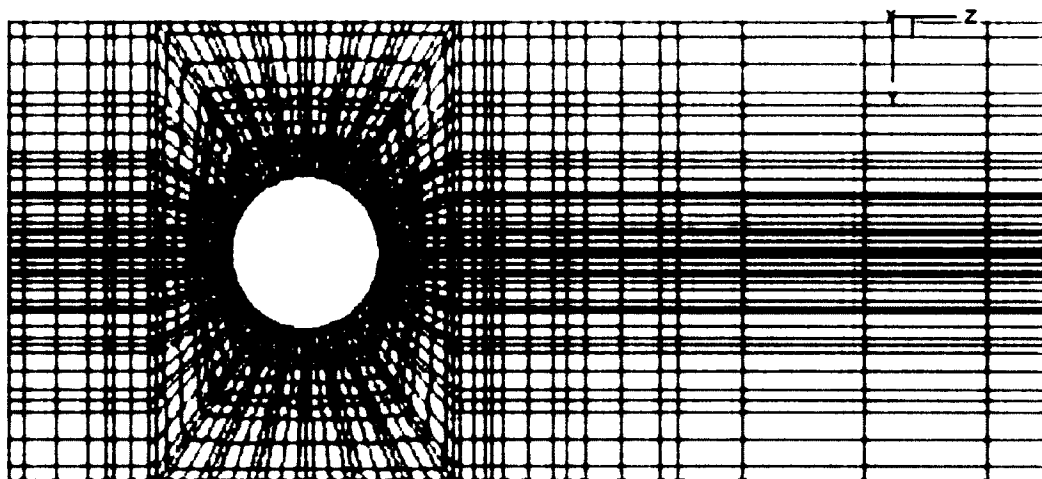


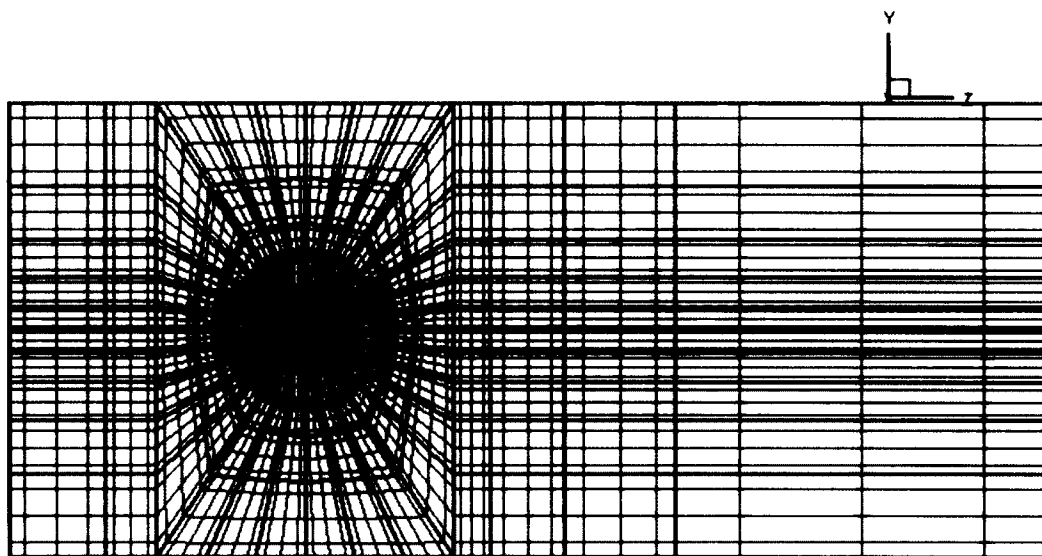
Figure 3-1: The three-dimensional environment flow in rectangular channel.



(a): The mesh of layer on xz-crosssection at $y = 0.01$.



(b): The mesh of layer on yz-crosssection at $x = 0.01$.



(c): The mesh of layer on yz-crosssection at $x = 5.01$.

Figure 3-2: The three-dimensional environmental flow-meshes on xz- and yz-crosssections at $y = 0.01$, $x = 0.01$ and $x = 5.01$, respectively.

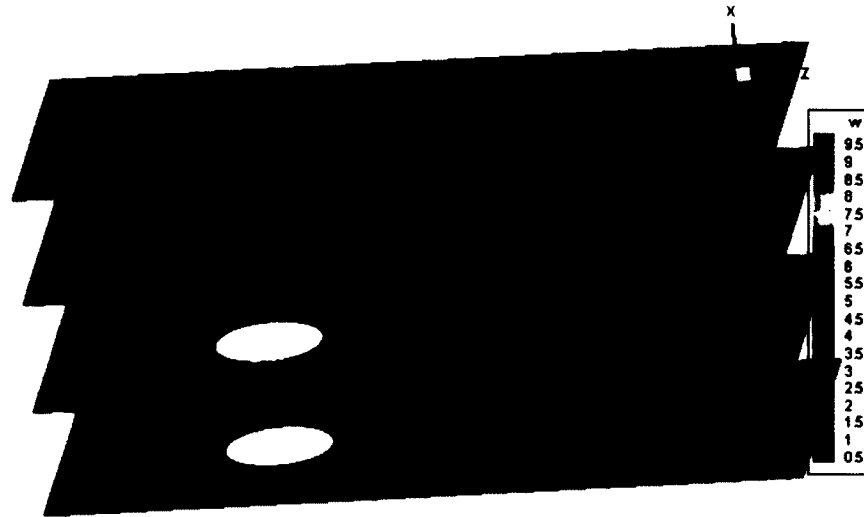


Figure 3-3: The three-dimensional environmental flow-velocity contour on z-direction in yz-planes of $x = 0.01, 1.99, 4.01,$ and 5.99 .

Besides the fourth order scheme, the third and fifth order schemes are also run with the same element number. From the third to fifth order test of 10,001 time steps, the models are performed on a single Fedora 23 system with Intel i-5 2320 processors and 16 GB RAM with running times of 0:37:34, 0:58:50, and 3:02:18. The dimensionless drag force on top of the cylinder is convergent to -314.201 on the y-direction.

3.2.2 A sphere inside an L-turn channel

Here, another model of a sphere inside an L-turn channel is simulated as shown in **Figure 3-4**. The fluid channel on three dimensions is defined as $-3.3566 \leq x \leq 14.1100, -2 \leq y \leq 2, -14.1100 \leq z \leq 3.3566$, with the internal radius $R_i = 7.46$ and the external radius $R_o = 11.46$. Meanwhile, the center of a sphere with radius $r = 1.0$ is located at $x = 3.4734, y = 0,$ and $z = -0.0840$. At the inlet, which is the zy-cross section at $z = -14.1100$, the initial velocities are set as $\mathbf{u}_x = 0, \mathbf{u}_y = 0,$ and $\mathbf{u}_z = 10(3.3566 + x)(0.6434 - x)/4$, so the maximum initial velocity $\mathbf{u}_{x-max} = 10$ is imposed at the

middle layer. At the outlet, which is the yz-cross section at $x = 14.1100$, the Neumann boundary condition of the velocity is $\frac{\partial u}{\partial n} = 0$, and the Dirichlet boundary condition of pressure $p = 0$. The mesh is divided into eight blocks - the inlet and the outlet blocks and another six blocks around the sphere as shown in **Figure 3-7**. The mesh around the sphere is refined, which means the sizes of the element are reduced while they are getting closer to the surface of the sphere. Moreover, in **Figure 3-6**, three different layers for contours of velocity on x are as shown. Simultaneously, the pressure and the velocities on x, y, z directions in the form of u, v, w are presented in **Figure 3-5**.

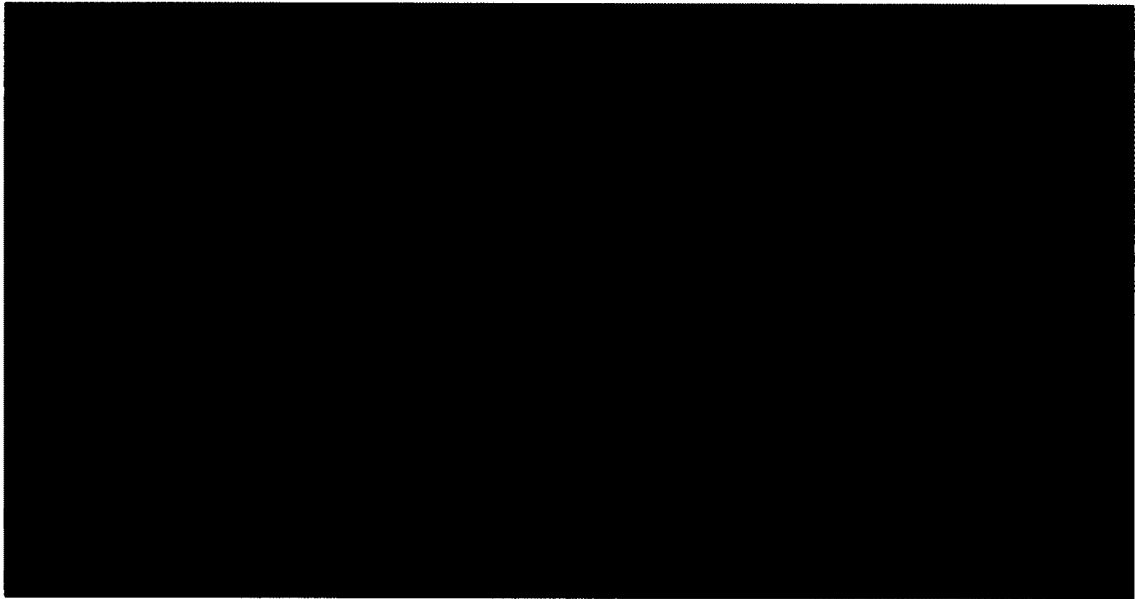


Figure 3-4: The three-dimensional environmental flow in a rectangular L-Turn channel.

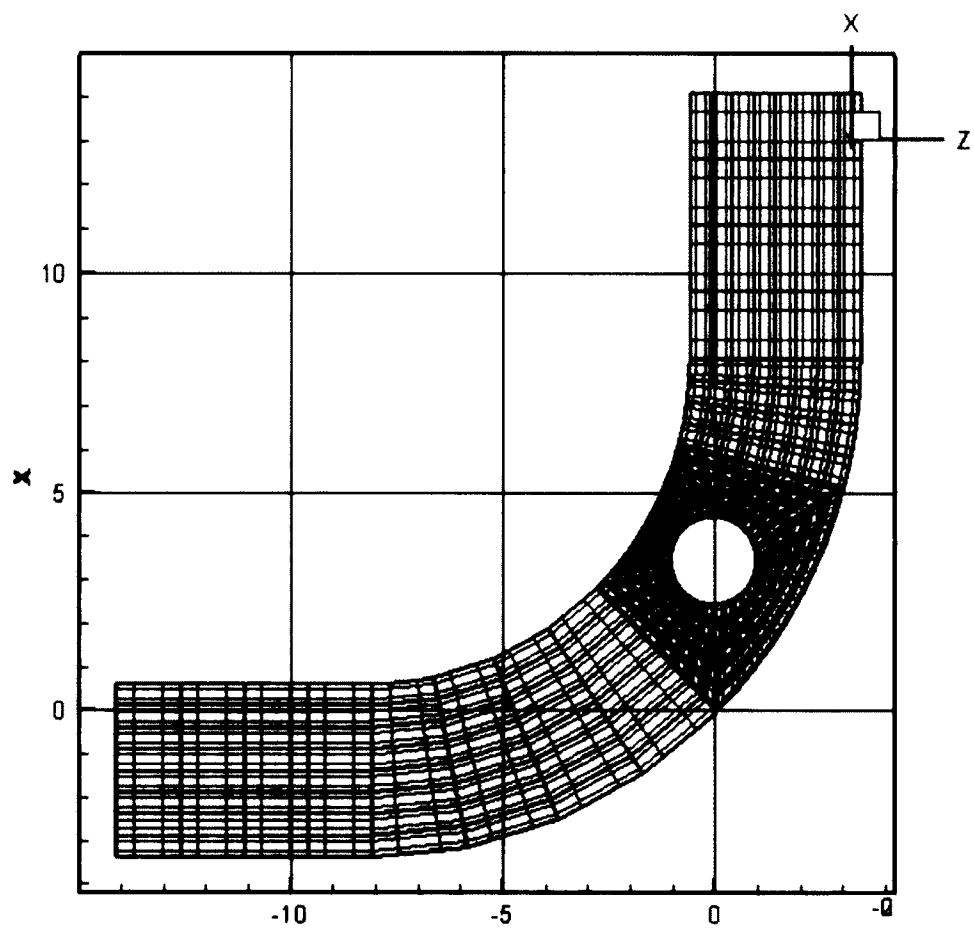


Figure 3-5: The mesh of the three-dimensional environmental flow in a rectangular L-Turn channel at xz -cross section on $y = 0.01$.

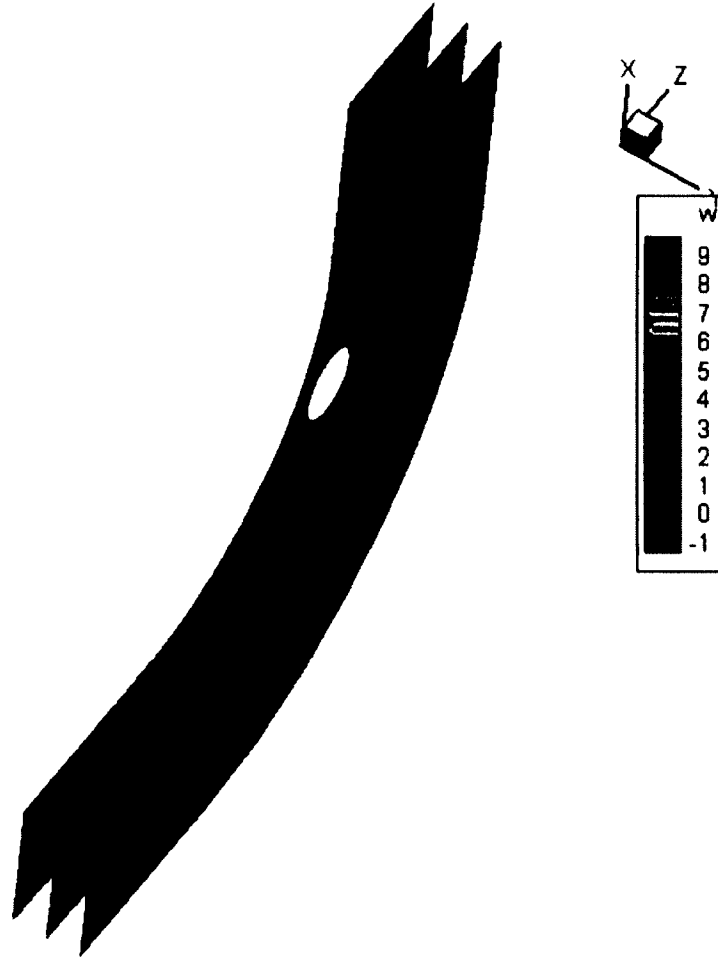


Figure 3-6: The velocity on z-direction of a three-dimensional environmental flow in a rectangular L-Turn channel at xz-cross section on $y = 0.01, 1.01, \text{ and } 1.99$.

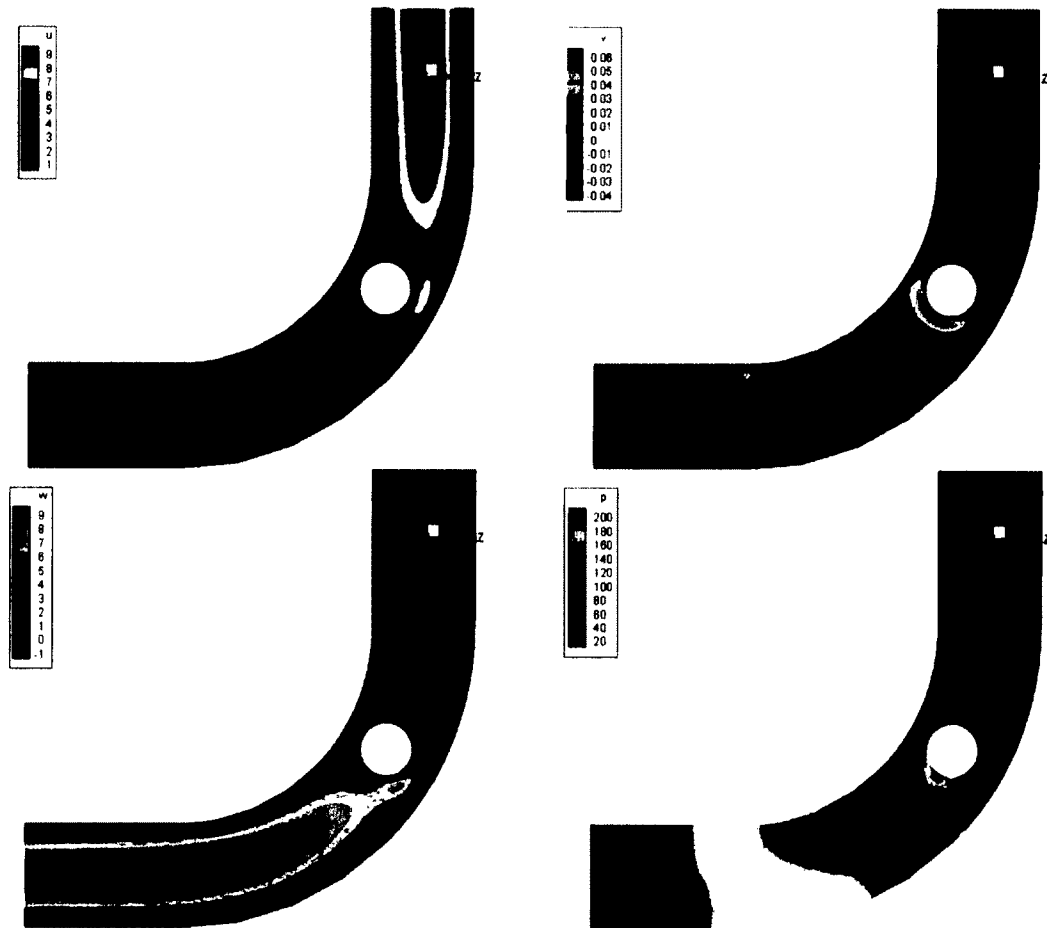


Figure 3-7: The contours of velocities on x, y, z direction (u, v, w) and the pressure (p) of three-dimensional environmental flow in a rectangular L-Turn channel at xz-cross section on $y = 0.01$.

Besides the case with the polynomial order of three, the cases with various element numbers and orders are also shown in **Table 3-2**. When we built a model with element number of 2944, the time consuming increased from about two hours to more than seven hours. To get results with higher resolution, the cost for personal computer seems too expensive. The high performance computing is needed in our future models.

Table 3-2: The comparison of the numerical solutions with 20,001 time steps.

Number of Element	Polynomial Order	Maximum Drag Force	Time consuming	Number of nodes
768	3	28.8582	00:50:02	26112
768	4	29.6857	03:42:37	96000
2944	3	29.5515	01:56:43	188416
2944	4	29.6113	07:12:16	368000

CHAPTER 4

ELECTROSMOTIC DRIVEN

MICRO FLOWS

4.1 Introduction

Applications of the micro-scale flow widely exist in our daily life. As the rapid development in micro fabrication technologies, to observe and simulate the phenomenon of this kind of flow, many mathematical models and numerical methods have been founded and carried out, for example, the finite difference method [42], the Lattice Boltzmann method [43], the DSMC method [44], and the spectral element method [45]. Micro flow system can be found in medical, biological, pharmaceutical, micro-electronic, and environmental monitoring applications. Examples of these applications are diagnosing medical conditions on earth and in space studied by NASA, micro flow imaging (MFI) in pharmaceutical companies, research on DNA computer [46, 47], and miniaturized flow cytometer in a microgravity environment. The design and development of these experiments are all based on the theoretical and experimental foundation of the micro fluids. Meanwhile, researches in [48-50] about micro flow for both numerical simulations and applications have been published in recent years.

The electroosmotic flow, which is a particular example in the micro flow regime, was first reported in 1809 [51], then experiments and studies for this topic were carried out. In 1879, Helmholtz [52], in his classic theoretical analysis of the streaming potential concept, developed the electric double layer theory. According to his theory, in 1977, the

Boltzmann distribution of the ion density variation was discovered due to statistical mechanical consideration [53]. Then the Poisson-Boltzmann equation becomes part of the body force when solving the Navier-Stokes equation of the electroosmotic flow. The paper [54, 55] indicated how the PB equation was linearized based on Debye-Huckel linearization. Based on the linearization, the numerical simulation of complex geometries for T-junctions and Y-splitting electrokinetically driven micro flow are analyzed in [56, 57].

The mathematic model of our micro flow systems is the numerical solution of compressible Navier-Stokes equation with the spectral element method. The spectral element method in CFD has been explained in [15]. For each model, a two-dimension domain is broken into small elements, which is the same as the finite element method (p refinement); however, meshes are provided with the basis functions of Legendre polynomials (h refinement). A spectral expansion defined by Gauss-Lobatto-Legendre points is used to represent fields and data.

In this chapter, complex geometries with Knudsen numbers ($Kn = \frac{\lambda}{L}$) of values between 0.01 to 10, which contain slip flow and transitional flow with electroosmotic body force, are chosen. The mean free path (λ) is the average distance of a moving particle travelled through successive impacts which can affect its energy, velocity and other properties, and the L is the representative physical length scale. Detail explanation of micro scheme of this flow is introduced in [45]. Our research is focusing on the continuum and slip regimes with the micro system and electro kinetic models.

4.2 Methodology

There are four categories of electrokinetic phenomena [58]: the Electrophoresis, the Streaming Potential, the Sedimentation Potential and the Electroosmosis, in which the electroosmotic flow is generated due to the interaction between the external applied electric field and the electric double layer (EDL). The body force is created when the external electric field has an effect on the charged ions in the EDL. In this chapter, the compressible Navier-Stokes equations with electroosmotic body force are taken as the governing equations:

$$\frac{\partial(\rho_f \mathbf{u})}{\partial t} + \rho_f \mathbf{u} \cdot \nabla \mathbf{u} = -\nabla p + \mu \nabla^2 \mathbf{u} + \rho_e \mathbf{E}, \quad \text{Eq. 4-1}$$

$$\frac{\partial \rho_f}{\partial t} + \nabla \cdot (\rho_f \mathbf{u}) = 0, \quad \text{Eq. 4-2}$$

$$\frac{\partial U}{\partial t} + \nabla \cdot (U \mathbf{u} - \sigma \mathbf{u} + \mathbf{q}) = \rho_e \mathbf{E} \cdot \mathbf{u}, \quad \text{Eq. 4-3}$$

in which **Eq. 4-1** and **Eq. 4-3** are the compressible continuity equation (**Eq. 3-4**), and the compressible Momentum equation (**Eq. 3-3**) and the Energy equation (**Eq. 3-5**) with electro osmotic body force. According to Santiago [59], the governing equations can be normalized as below:

$$t' = \frac{t}{t^*}, \mathbf{x}' = \frac{\mathbf{x}}{d}, \mathbf{u}' = \frac{\mathbf{u}}{V}, \rho_f' = \frac{\rho_f}{\rho},$$

$$p' = \frac{pd}{\mu V}, \mathbf{E}' = \frac{\mathbf{E}}{E^*}, \rho_e' = \frac{\rho_e d}{E^* \epsilon},$$

where $t, \mathbf{x}, \mathbf{u}, \rho_f, \mathbf{E}$, and ρ_e are time, position vector, velocity vector, fluid density, pressure, electric vector field and net electric charge density, respectively. All these variables are nondimensionalized by $t^*, d, V, \rho, \mu, E^*$, and ϵ , which are characteristic time

scale, microchannel hydraulic diameter, characteristic flow velocity, characteristic fluid density, dynamic viscosity, characteristic electric field, and electrical permittivity.

The electric double layer, which is the region of mobile ions near the interface, is formed because of the chemical equilibrium between the boundary and the electrolyte solution. As the thickness of the EDL is very small, when compared with the width of the channel, we reduce the element size beside the boundary and also try to use the basis functions with a higher order. In **Figure 4-1**, the boundary conditions are set the same on each side of the cross section, and the values of the electro-osmotic potential are normalized by its maximum value, the difference of the external electric potential is determined as 100 V/m to show as an example. **Figure 4-2** has the same boundary condition but with opposite values on each side. Since the EDL double layer is too thin, we set the thickness of EDL to 1/10 of the width of the cross section to make it easy for observing.

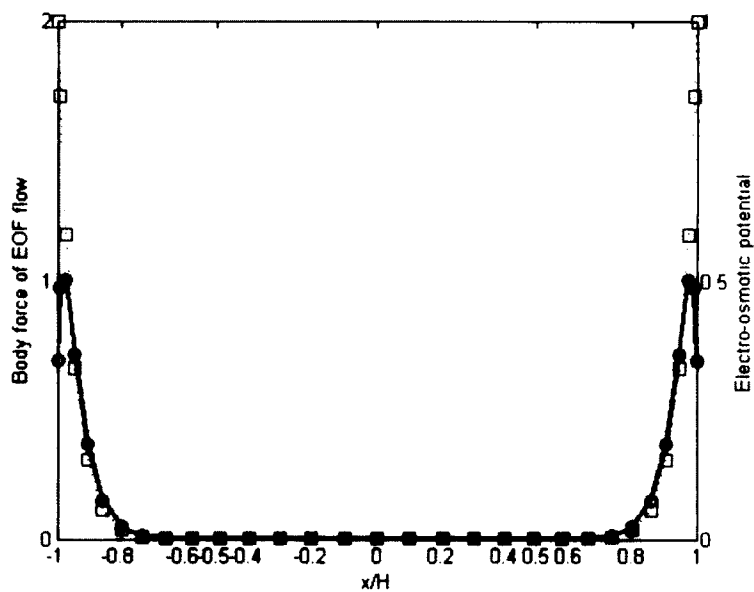


Figure 4-1: Normalized Electro-osmotic potential and its related body force on cross section of wall boundary.

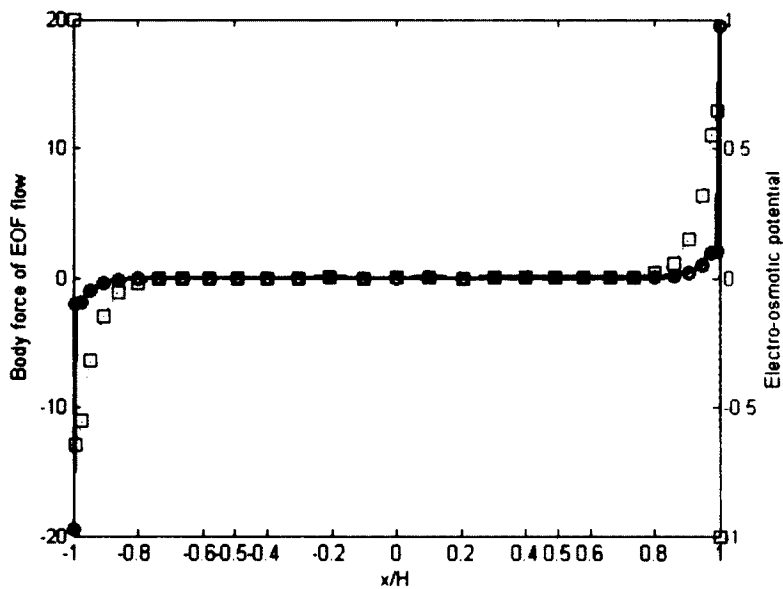


Figure 4-2: Normalized Electro-osmotic potential with opposite values on each side and its related body force on the cross section of wall's boundary.

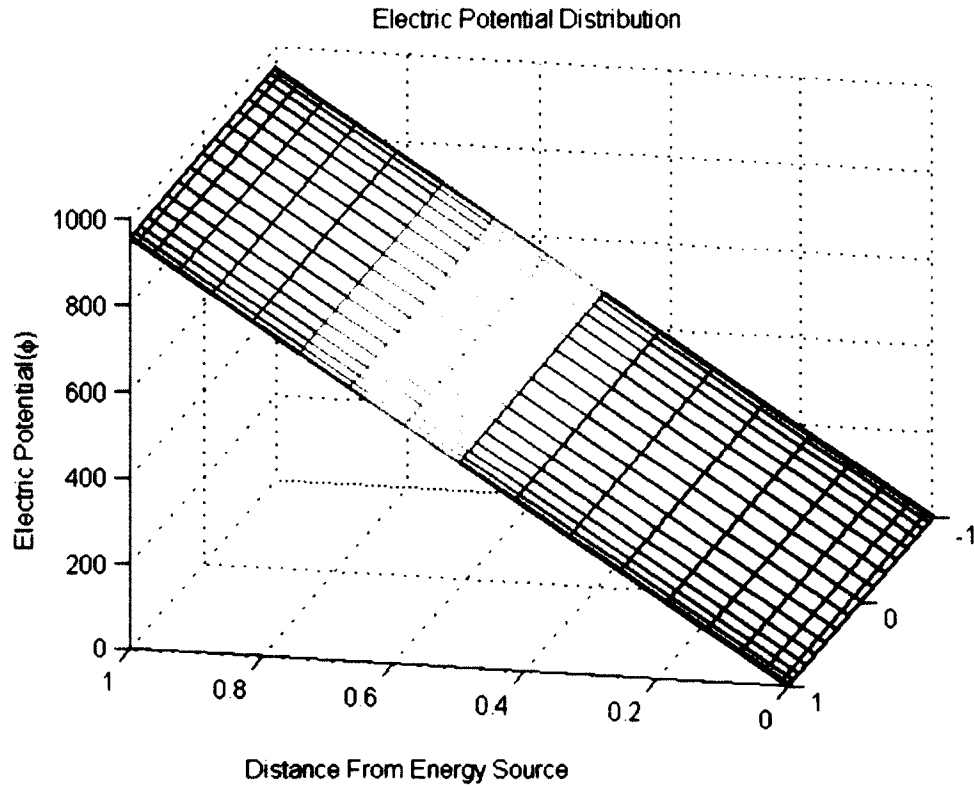


Figure 4-3: The numerical solution of the electric potential on a rectangular area.

It seems that **Eq. 4-5** is a Poisson equation with Dirichlet boundary conditions. The numerical solution shows the driving force caused by electrical potential is linearly dependent with the absolute distance from the electrical source. In this chapter, all these electrical potentials are set as 0.0 at the outlet. As a result, this part of the driving force at a specific node can be easily calculated by the potential multiplied by its absolute distance to the outlet. However, the other part of **Eq. 4-4** shows its difficulty. Since the driving force of the electro osmotic flow is generated by the external electric field (normally on the input and output of flow) that interacts with the EDL, its body force is a function of the net electric charge density on the surface and electric field. As a result, the velocity of this flow is very slow [60]. The body force is combined with a function of E' and ρ'_e , which are determined by Poisson-Boltzmann equation as follows:

$$\mathbf{E}' = -\nabla(\phi + \psi), \quad \text{Eq. 4-4}$$

$$\nabla^2 \phi = 0, \quad \text{Eq. 4-5}$$

$$\nabla^2 \psi = -\frac{\rho'_e}{\varepsilon}, \quad \text{Eq. 4-6}$$

as \mathbf{E}' in Eq. 4-4 can be divided into two parts where ϕ and ψ stand for the electric potential of the fluid, and the electro osmotic potential. Eq. 4-5 is a Poisson equation with Dirichlet boundary conditions, which is easy to solve, and Eq. 4-6 is one equation with two unknown variables that cannot be solved directly. Its simplification and linearization is shown below.

By the physical definition, the charge density can be represented as:

$$\rho_e = \sum_i c_i z_i F, \quad \text{Eq. 4-7}$$

where c_i , z_i , and F are the molar concentration of species i (mol/L), the net quantity of the electric charge and the elementary electric charge (charge/mol), respectively. In Eq. 4-7, by Boltzmann relation:

$$c_i = c_{i\infty} \exp\left(-\frac{e}{RT}\right), \quad \text{Eq. 4-8}$$

in which $c_{i\infty}$ is the ambient concentration of the i -th ion species far away from the particles; e is the molar potential energy; T is Kelvin temperature; R is the universal molar gas constant. For these parameters, $c_{i\infty}$ and T are known for the given solution, R is constant, and e can be represented as:

$$e = z_i F \psi. \quad \text{Eq. 4-9}$$

When combining Eq. 4-7 with Eq. 4-9, the Poisson-Boltzmann equation is shown as:

$$\nabla^2\psi = -\frac{1}{\varepsilon} \sum_i \left[c_{i\infty} \exp\left(\frac{-z_i^2 F^2 \psi}{RT}\right) \right]. \quad \text{Eq. 4-10}$$

Then according to Debye-Huckel approximation, if in Eq. 4-10, $F^2\psi \ll RT$, the linearized Poisson-Boltzmann equation is obtained:

$$\nabla^2\psi = \frac{F^2\psi}{\varepsilon RT} \sum_i (c_{i\infty} z_i^2) = k^2\psi, \quad \text{Eq. 4-11}$$

where the k^2 and ρ_e can be obtained by:

$$k^2 = \frac{F^2\psi}{\varepsilon RT} \sum_i (c_{i\infty} z_i^2), \quad \text{Eq. 4-12}$$

$$\rho_e = -\varepsilon k^2 \psi, \quad \text{Eq. 4-13}$$

since Eq. 4-11 is the linear form of Poisson-Boltzmann equation. The Reynolds number (Re) and Strouhal number (St) are defined as:

$$Re = \frac{\rho V d}{\mu}, \quad \text{Eq. 4-14}$$

$$St = \frac{d}{V t^*}. \quad \text{Eq. 4-15}$$

Then the nondimensionalized form of the momentum equation becomes:

$$St Re \frac{\partial(\rho_f' \mathbf{u}')}{\partial t'} + Re \mathbf{u}' \cdot \nabla' \mathbf{u}' = -\nabla' p' + \nabla'^2 \mathbf{u}' + Re \frac{\varepsilon E^{*2}}{\rho_f V^2} \rho_e' E'. \quad \text{Eq. 4-16}$$

4.3 Results and Discussion

In this section, two different models with compressible electro osmotic flow are presented: (1) straight channel with a width of 100 μm with a narrower length of the channel of 50 μm by 50 μm in the middle, and (2) a channel with a curvature wall boundary. The first case is used to test the effect of the density change and electro osmotic driving force on flow rate. The second case is used to check the simulation for

the model with a curvature boundary. A two-dimensional C++ code is developed to simulate all these models. The main subroutines of this code are presented in Appendices F-O, and **Table 4-1** below shows their functions. Appendix F is a library function that can generate the Gauss-Lobatto-Legendre points and weights. The function ZWGLL can be called with three variables: zeros points, weights and the polynomial order.

Appendices G-K are called in Appendix L to calculate the coefficients which are needed to build system matrix. Appendices M and O are the processes of nondimensionalization and recovery of nondimensional values to dimensional ones. Appendix N is the function that finds the CFL condition in the models. When the value of the CFL condition is larger than reference number, a warning will be shown in the screen to indicate that the initial conditions or the mesh may need to be refined.

Table 4-1: The important subroutines used for solving the compressible Navier-Stokes equations by the SEM.

Name	Appendix number	Function
ZWGLL.h	F	Gauss-Lobatto-Legendre points and weights
DGLL	G	GLL derivative matrix
HGLL	H	GLL lagrangian interpolant
IGLLM	I	Interpolation operator
PNLEG	J	Generate Legendre polynomial of degree N
PNDLEG	K	Derivative of Legendre polynomial of degree N
COEF	L	Compute coefficients needed in code
FORTIC	M	Nondimensionalization
DTDECIDE	N	Compute CFL condition
POST	O	Recover the nondimensional values to dimensional ones

4.3.1 Grooved-channel

In this case, we choose the model with obvious density changes. At the middle of the channel, the width of the channel directly decreases to half at the inlet and outlet. We adjust the strength of the external electric field as well as the density at the input and output to simulate the process of electro osmotic phenomenon. The boundary conditions are set as the wall during the narrow part and period at the other sides. **Figure 4-4** is the result of the sixth order spectral nodal element method with the electric field lines at critical part.

It seems that when the driving force from pressure gradient is large, the effect from electro osmosis field can be ignored. That is to say the electro osmosis phenomenon is a slow process which can be covered by the large value of input velocity, pressure gradient, and all the parameters that make the model a quick process. In **Figure 4-4** the densities of fluid are set as 1.0 and 0.9, respectively, at the inlet and outlet. Point A and E are all at the middle of the channel. A is at the middle near the inlet. There is no slip boundary condition, and the driving forces caused by density change and electro osmosis field are not large. This point can be used as a reference for the other points. Point E is at the middle of the narrow part. The velocity of E is the highest in all points. Point B, as it is shown in **Figure 4-4**, is located near the dead end along the velocity direction.

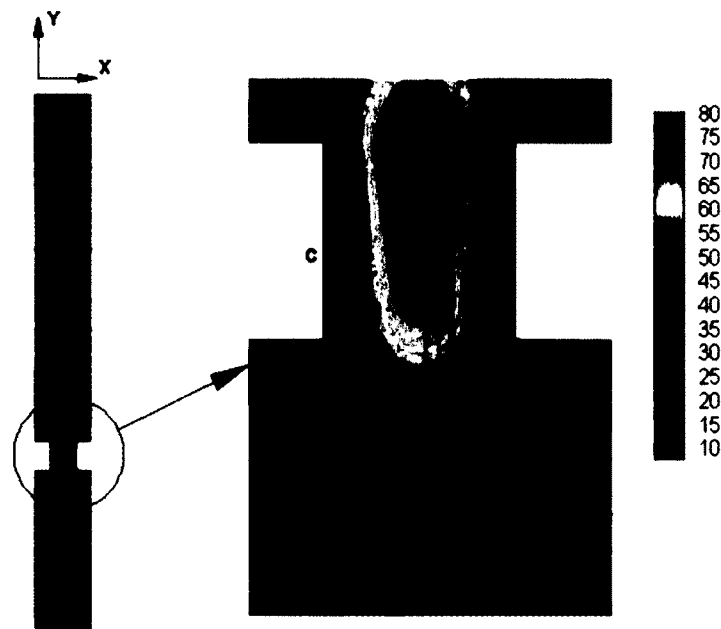


Figure 4-4: The lines of the electric field and velocity contour for the model of Grooved-channel on y-direction.

The points from A to E are the history points tracked in **Figure 4-5**. When the input velocity is large, the effect of the electro osmotic driving force can be ignored. The value of the input velocity and external electric field are set to 0.0 m/s and 10 KV/m. We zero the initial velocity because the velocity of pure electro osmosis flow is very small, then the large input velocity will cover the velocity change due to electro osmosis field. Test run shows that the convergent results (including energy, velocity, pressure, temperature) of the fixed points under the compressible flow model and compressible electro osmosis flow model almost have no difference when the compressibility ratio is larger than 1:0.85-density of 1.0 at inlet and 0.85 at outlet. That is to say, in these situations, the effect of the driving force from the electro osmosis field is overlapped by pressure gradient. The difference between these two models is about 0.1%.

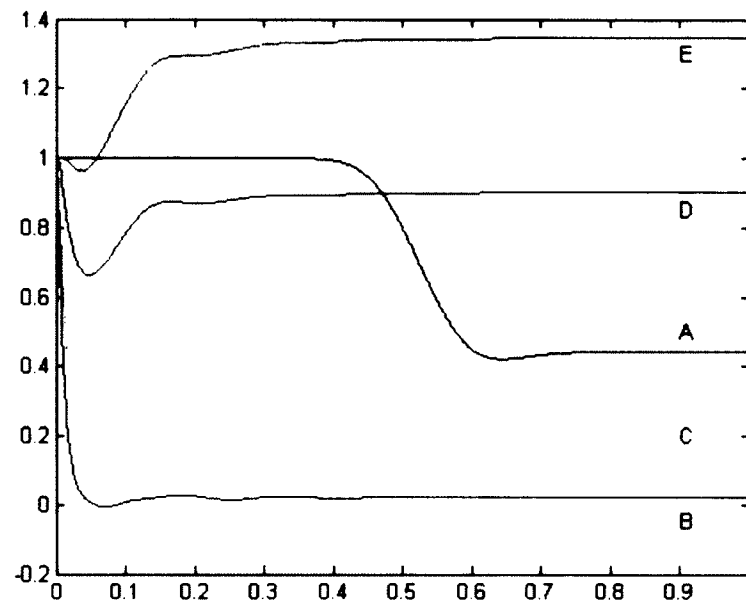


Figure 4-5: Velocities track over five history points.

As a result, the velocity at this point is nearly 0.0. For point C, this point is near the wall inside the EDL, on which both slip boundary condition and electro osmosis field have an effect. Slip boundary condition decreases velocity and electro osmosis field, works with external electric potential, and increases velocity. Simultaneously, due to the compressibility of the fluid at this part, pressure gradient also provides the driving force. The velocity for point C is relatively smaller than the point near the inlet and outlet of the EDL. Point D is outside of the EDL between point E and C, the velocity of which is larger than C and smaller than E. Simultaneously, the contours for velocities on x directions (v), density (Rho), energy (e) and temperature ($Temp$) are shown as follow in **Figure 4-6**.

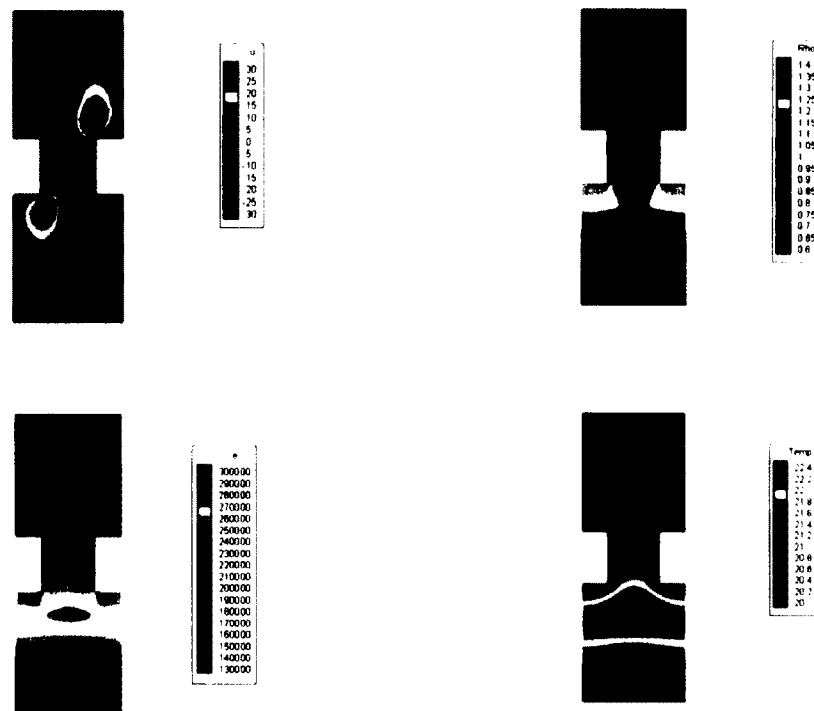


Figure 4-6: The contours for velocity of y-direction (u), density (Rho), energy (e), and temperature ($Temp$) at critical area.

4.3.2 Curvature-channel

According to the discussion of case 1, we set the same boundary and initial conditions. The density at the inlet and outlet is set as 1.0 and 0.9 with the channel aspect ratio of 20:1. The purpose of this model is to test the compressible electro osmosis flow in a rough channel, and to reduce the density change caused by geometry. In **Figure 4-7**, there are 80 elements in the whole model, and only 2 elements in the cross section. We reduce the number of elements and increase the polynomial order of the basis function to 10; that is to say there are 121 zero points in each element.

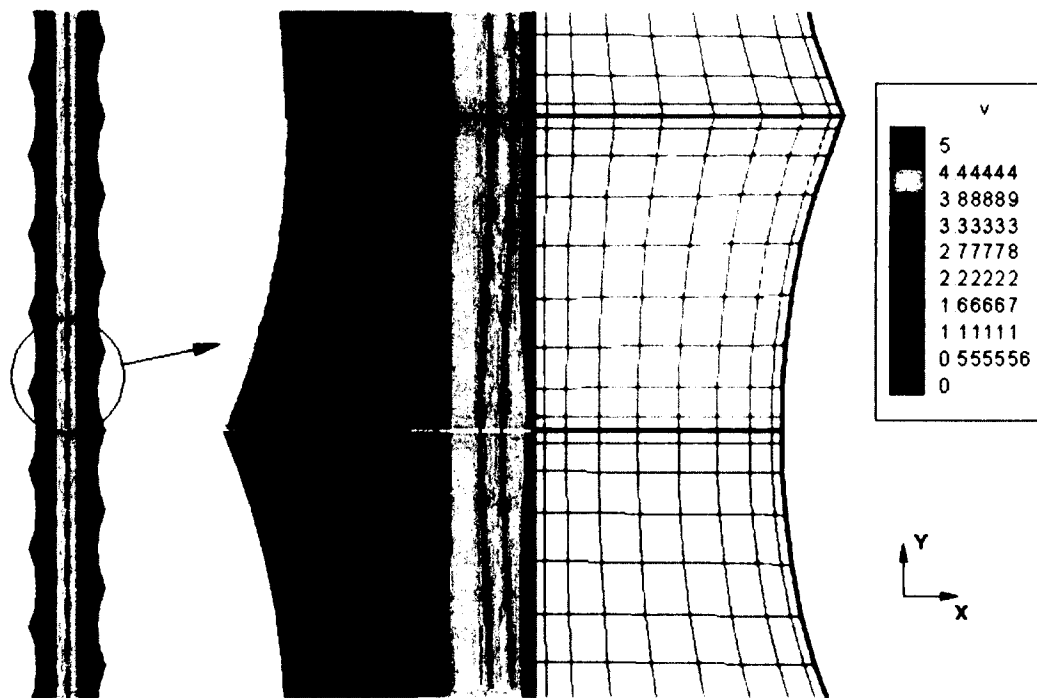


Figure 4-7: Electric field and contour for velocity on y-direction.

In this case, the initial velocity is set as 0, and the driving forces come from the pressure caused by the density change at the inlet and the outlet, and the electrical potential. The results show the contour for velocity on y-direction. It seems that although on the boundary value of the electro osmotic potential reaches maximum, the drag force imposed by the slip boundary still reduces the velocity near the wall, which means even when the external driving force is larger in the area near the wall than that in the middle of the channel, it still cannot overcome the drag force of the slip layer. As a result, the flow rate near the boundary is almost zero, which is the same as what happened in case 1. Therefore, the velocity for the whole flow field is very slow. With the electrical field of 10 kV/m, the max velocity is only 0.374 mm/s.

4.4 Conclusions

In electro osmotic flows, the thickness of the electric double layer is much smaller than both the characteristic length of the channels and the curvature radius of the models. Since they are compressible models, the numerical simulations for mix electro osmotic and the pressure driving flow are discussed. The effect on the flow rate from pressure change is much larger than the electro osmotic driving force. For the pure electro osmotic driving flow, the velocity field can be divided into inner and outer flow regions due to the slip boundary layer. Inside the inner region, the driving force caused by the electro osmotic potential and the shear force results in slip boundary condition (including velocity gradient, thermal creep and temperature jump) need to be considered. For the out region, the main driving force is generated by pressure because of volume change and velocity gradient.

To get results with higher accuracy, firstly, the h/p refinement is carried out. Near the wall's boundary regions, the mesh elements should be smaller than those in the middle, and the polynomial order of the basis function can be set as 5 or 6. Secondly, since for the flow rate the effect of density change is more serious than the electro osmotic force, if the density change is too large, its effect will cover the effect which is caused by the electro osmotic force. Normally, the mobilities of pure electro osmotic flow are the order of $10^{-8} \text{ m}^2\text{V}^{-1}\text{s}^{-1}$ by electrical field strength of 5 to 20 kV/m [60]. The flow rate is relatively very small when compared to the large electric potential.

As a result, for the compressible flow, we need to reduce the inlet and outlet velocity or the driving force to see the electro osmotic phenomenon. All in all, due to the lack of physics model and experiment for compressible electro osmotic flow, we are trying to simulate the complex geometries with density change, slip boundary conditions, and electro osmotic effect for future applications.

CHAPTER 5

CONTINUOUS AND DISCRETE SIMULATIONS OF MICRO-NEEDLES FOR EPIDERMAL DRUG DELIVERY

5.1 Introduction

Traditional injection uses a syringe to insert liquid into the body. The purpose of medical injection is to pierce the material into the sufficient depth of the skin. This kind of injection needs to use a large number of syringe needles, and according to [61], clients reported that an average of 8.7% of injections employed shared syringe needles. Data from the Coalition for safe Community Needle Disposal showed that in 2011, 13.5 million people in the United States produced 7.8 billion used sharps (needles, syringes, etc.) outside the traditional healthcare, and 1 million to 1.5 million of needles were used for illegal drug injections. Since blood borne infections, like HIV, HBV, and HCV, can be commonly spread by sharing intravenous syringes, a large number of substandard and illegal use of needles compares to the shared rate of 8.7%; the potential spread of these infections cannot be ignored. On the other hand, the application of the micro needle can to a large extent eliminate this from its source.

Micro needles, which are recently developed by the Georgia Institute of Technology and the Centers for Disease Control and Prevention (CDC) [62, 63], are small patches that can be administered by untrained users. Small needles are placed on the patch of about one square centimeter. Instead of asking a nurse for a muscle injection,

only with a press of a thumb, this kind of needle can be used for vaccine inoculation and local anesthesia.

In this paper, both the spectral element method and the smoothed particle hydrodynamics method are applied to simulate the models of the micro needle. The Spectral element method used in computational fluid dynamics is explained in [15] and [45]. For spectral element models of the micro needle, the process is divided into two parts, the model of the flow in the micro-needle and the model of the solution flux inside human skin. Incompressible Navier-Stokes equations with slip boundary condition are solved inside the micro needle. The human skin is treated as porous media, so the Darcy-Brinkman equation is solved to simulate this process. At the same time, the output data of the micro needle are taken as the initial conditions of the Darcy-Brinkman model.

SPH was first proposed in 1977 by Gingold, Monaghan and Lucy. At the beginning, this method was used to solve the problem of high-speed collisions of astrophysics. After that, the method has been applied to solve fluid dynamics and solid mechanics problems. Presently, depending on its advantages in incompressible flows, fluid-solid interaction, solid mechanics, and explosion simulation, SPH was widely used [64]. The SPH method is suitable for solving an expanding range of applications in the field of Computation Fluid Dynamics. Particles are used to represent interactions between flow and structures, as well as the flow of large deformation with moving boundaries.

The mesh free method for large deformation problems of fluid simulation compared with the traditional grid method has obvious advantages, the traditional method unable to deal with a large deformation problem of fluid, because the local grid deformation is too large and will cause the computation result to distort. This simulation

uses the SPH algorithm to simulate the movement of a drug's molecule in the porous medium of the dermis after a single micro needle pierced skin. Micro needle compared with the traditional needle injection has obvious merits. Besides reducing the piercing pain, the drug will penetrate more uniform and faster. Two models illustrate these characteristics. Some of the original data come from students' report [71], and all the parameters shown in **Table 5-1** are confirmed from their citations.

Table 5-1: Reference parameters of simulations.

Convection and Diffusion	
Diffusivity Coefficient of Lidocaine, D	$1.38 \times 10^{-8} \text{ m}^2/\text{s}$ [65]
Fluid Flow	
Density of Lidocaine, ρ	$999 \text{ kg}/\text{m}^3$ [66]
Dynamic Viscosity of Lidocaine, η	$0.001 \text{ Pa} \cdot \text{s}$ [67]
Porosity, Φ	0.5 [68]
Intrinsic Permeability of Skin, k	10^{-17} m^2 [69]
Minimum Concentration Required at Nerves	$0.004267 \text{ mol}/\text{m}^3$ [70]
Initial Concentration at output of needle	$42.67 \text{ mol}/\text{m}^3$ [71]

5.2 Methodology

5.2.1 Continuous Modeling

The Spectral Element Method is chosen to build and solve the continuous modeling system of the micro needle. The first part of our spectral element model is the simulation of the solution inside the micro needle. Slip boundary condition is considered

in this model with incompressible Navier-Stokes equations. After moving out of the needle, the process of solution diffusing inside human skin is built as the second model.

5.2.1.1 Part 1: Medicine Liquid Flow through Micro-needle

In a three-dimensional domain Ω , the incompressible Navier-Stokes equations are written as:

$$\rho \left(\frac{\partial \mathbf{u}}{\partial t} + (\mathbf{u} \cdot \nabla) \mathbf{u} \right) = -\nabla p + \mu \nabla^2 \mathbf{u} + \mathbf{f}, \quad \text{Eq. 5-1}$$

$$\nabla \cdot \mathbf{u} = 0, \text{ on } \partial\Omega, \quad \text{Eq. 5-2}$$

where $\mathbf{u} = (u, v, w)$ is the fluid velocity, p represents the pressure, and μ is the dynamic viscosity of the fluid. There are four equations with four unknown variables: u , v , w , and p . The energy equation is ignored in this case. The boundary and initial conditions are shown as follows:

$$\mathbf{u}(\text{needle wall}, t) = \mathbf{0},$$

$$\mathbf{u}(\text{needle inlet}, t = 0) = \mathbf{0},$$

$$\mathbf{u}(\text{inside needle}, t = 0) = \mathbf{0},$$

$$p(\text{needle inlet}, t) = P_{\text{Applied}} = 10 \text{ kPa},$$

$$p(\text{needle boundary}, t) = 0.$$

For Part 1, The Navier-Stokes equations are normalized as follows:

$$t' = \frac{t}{t^*}, x' = \frac{x}{d},$$

$$\mathbf{u}' = \frac{\mathbf{u}}{U}, p' = \frac{pd}{\mu U},$$

where t , x , \mathbf{u} , and p are time, position vector, velocity vector, and pressure, respectively.

These variables are non-dimensionalized by t^* , d , U , and μ , which are characteristic time

scale, micro-channel hydraulic diameter, characteristic flow velocity, and dynamic viscosity.

5.2.1.2 Part 2: Medicine Diffusion Under Skin

In this part, human skin is treated as porous media. The outputs of the previous model are used as the input initial conditions of this section. Moreover, the process of solution diffusing under the skin is simulated by the Darcy-Brinkman equations:

$$\mathbf{u} = \frac{k\Phi}{\mu} [-\nabla p + \mu_e \nabla^2 \mathbf{u}], \quad \text{Eq. 5-3}$$

$$\nabla \cdot \mathbf{u} = 0, \quad \text{Eq. 5-4}$$

and the mass transport equation:

$$\frac{\partial c}{\partial t} + \mathbf{u} \cdot \nabla c = D \nabla^2 c, \quad \text{Eq. 5-5}$$

where p , \mathbf{u} , k are pressure, superficial velocity vector, and permeability of porous medium, respectively, Φ is porosity, and μ_e is dynamic viscosity for Brinkman term. When we compare Eq. 5-1 with Eq. 5-3 and Eq. 5-5, it seems that Eq. 5-3 and Eq. 5-5 are modified and simplified forms of the Navier-Stokes equation. In Eq. 5-3, the convection part and external force have been ignored, the variation of velocity has been changed to steady form, and some coefficients are replaced to satisfy the porous medium. In Eq. 5-5, the convection and pressure part have also been canceled, and the velocity in the diffusion and variation term is replaced with the concentration.

The boundary and initial conditions for the Darcy-Brinkman equations are shown as:

$$\mathbf{u} (\text{skin boundary}, t) = \mathbf{0},$$

$$\mathbf{u} (\text{skin top wall}, t) = \mathbf{0},$$

$$\mathbf{u} (\text{skin inlet}, t = 0) = \mathbf{u}_{\text{Applied}} = \mathbf{u}_{\text{NeedleOutlet}},$$

$$p (\text{skin boundary}, t) = 0 \text{ kPa},$$

$$p (\text{skin inlet}, t = 0) = p_{\text{Applied}} = p_{\text{NeedleOutlet}},$$

and for the Mass Transport equation, the boundary and initial conditions are:

$$c (\text{skin bottom wall}, t = 0) = 0 \text{ mol/m}^3,$$

$$\frac{\partial c}{\partial z} (\text{skin boundary}, t) = 0,$$

$$c (\text{skin tissue}, t = 0) = 0 \text{ mol/m}^3,$$

$$c (\text{skin inlet}, t = 0) = 42.67 \text{ mol/m}^3.$$

5.2.2 Discrete Modeling

The Smoothed Particle Hydrodynamics is a weighted interpolation method [72] used to describe the motion of solid, liquid or gas in space with a discrete interpolation.

The interpolating function is denoted as $W(r - r', h)$ where h is the radius of the influenced region around position r' . The interpolating function is essentially a probability density function [73]:

$$\int W(r - r', h) dr' = 1, \quad \text{Eq. 5-6}$$

$$\lim_{h \rightarrow 0} W(r - r', h) = \delta(r - r'), \quad \text{Eq. 5-7}$$

when limitation of h equals to 0.0, the equation can be simplified to $\delta(r - r')$. Based on the above functions, a property I at location r could be described as [73]:

$$I(r) = \int I(r') W(r - r', h) dr' = \int \frac{I(r')}{\rho(r')} W(r - r', h) \rho(r') dr', \quad \text{Eq. 5-8}$$

$$I(r) \approx \sum_{r' \rightarrow 0} m(r') \frac{I(r')}{\rho(r')} W(r - r', h). \quad \text{Eq. 5-9}$$

The gradient of I at the point could be computed as [74]:

$$\nabla I \approx \sum_{r' \rightarrow 0} m(r') \frac{I(r')}{\rho(r')} \nabla W(r - r', h). \quad \text{Eq. 5-10}$$

Because both the Interpolating function and I approach to 0, the surface integral term could be eliminated [75].

5.2.2.1 Drug Particles

The Navier-Stokes equations are written in the Lagrange form:

$$\frac{\partial \mathbf{v}}{\partial t} = -\frac{1}{\rho} \nabla P + \mu \Delta \mathbf{v} + \mathbf{f}_{ex}, \quad \text{Eq. 5-11}$$

where P , \mathbf{f}_{ex} , ρ are pressure, external force, and fluid density. For stability and other considerations, the pressure term is changed to

$$\frac{1}{\rho} \nabla P + \mu \Delta \mathbf{v} = -\nabla \left(\frac{P}{\rho} \right) - \frac{P}{\rho^2} \nabla \rho + \mu \Delta \mathbf{v}. \quad \text{Eq. 5-12}$$

Now the Navier-Stokes equations are in its discrete form [76] as shown below:

$$\frac{\partial v_i}{\partial t} = \sum_j m_j \left(\frac{p_i}{\rho_i^2} + \frac{p_j}{\rho_j^2} + \prod_{ij} \right) \nabla_i W_{ij} + f_{i,ex}, \quad \text{Eq. 5-13}$$

where i and j are indices of current fluid particles within the radius of influence and neighbor particles, respectively. Density and pressure are given as the following [77]:

$$\rho = \sum_j m_j W_{ij}, \quad \text{Eq. 5-14}$$

$$P_i = \frac{\rho_0 c_0^2}{7} \left[\left(\frac{\rho_i}{\rho_0} \right)^7 - 1 \right], \quad \text{Eq. 5-15}$$

where \prod_{ij} is the viscous pressure [78]

$$\prod_{ij} = \begin{cases} \frac{-\alpha c \tilde{\mu}_{ij} + \beta \tilde{\mu}_{ij}^2}{(\rho_i + \rho_j)/2}, & \text{if } \mathbf{v}_{ij} \cdot \mathbf{r}_{ij} < 0, \\ 0, & \text{otherwise} \end{cases} \quad \text{Eq. 5-16}$$

$$\begin{cases} \alpha = 0, 0 < \beta < 1, \text{ for low Mach number flow} \\ \alpha = 0, \quad \beta > 1, \text{ for high Mach number flow.} \end{cases} \quad \text{Eq. 5-17}$$

5.2.2.2 Solid Particles

In this two-dimensional micro needle model, we use fixed points which are randomly distributed to represent the porous media of the dermal layer. Molecules move into a porous medium dermis, collide with porous media, and disperse in the dermis layer gradually. Human dermal thickness is generally around 2 mm; the model of the porous media thickness is 4 mm; the length of the micro needle is 600 μm ; the base diameter is 400 μm . When the depth of molecular particles is around 2 mm, they have entered subcutaneous tissue and capillaries, and throughout the blood flow. By measuring the number of particles beyond 2 mm, we can calculate the concentration of the drug molecules in units of blood.

The momentum equation, containing stress tensor σ , in the component form is shown as the following [79]:

$$\frac{dv^a}{dt} = \frac{1}{\rho} \frac{\partial \sigma^{ab}}{\partial x^b} + f^a, \quad \text{Eq. 5-18}$$

where a, b stand for Cartesian components, f^a is the body force, and the tensor stress σ^{ab} is consisted of the deviatoric stress S^{ab} and the volumetric stress $P\delta^{ab}$. Since the volumetric stress is easy to calculate, occurs the following equation describes how the change rate of the deviatoric stress occurs

$$\frac{dS^{ab}}{dt} = 2\mu \left(\dot{\epsilon}^{ab} - \frac{1}{3} \delta^{ab} \dot{\epsilon}^{ab} \right) + S^{ac} \Omega^{bc} + \Omega^{ac} S^{cb}, \quad \text{Eq. 5-19}$$

in which Ω^{ab} and $\dot{\epsilon}^{ab}$ are calculated by

$$\epsilon^{ab} = \frac{1}{2} \left(\frac{\partial v^a}{\partial x^b} + \frac{\partial v^b}{\partial x^a} \right), \quad \text{Eq. 5-20}$$

$$\Omega^{ab} = \frac{1}{2} \left(\frac{\partial v^a}{\partial x^b} - \frac{\partial v^b}{\partial x^a} \right). \quad \text{Eq. 5-21}$$

The derivatives of velocity in Eq. 5-20 and Eq. 5-21 are calculated according to [80]:

$$\left(\frac{\partial v^a}{\partial x^b} \right)_i = - \sum_j \frac{m_j}{\bar{\rho}_{ij}} (v_i^a - v_j^a) \frac{\partial W_{ij}}{\partial x_i^b}, \quad \text{Eq. 5-22}$$

where $\bar{\rho}_{ij} = \frac{\rho_i + \rho_j}{2}$.

The momentum equation for the SPH scheme is:

$$\frac{dv_i^a}{dt} = \sum_j m_j \left(\frac{\sigma_i^{ab}}{\rho_i^2} + \frac{\sigma_j^{ab}}{\rho_j^2} \right) \frac{\partial W_{ij}}{\partial x_i^b} + f^a. \quad \text{Eq. 5-23}$$

5.2.2.3 Particles Interaction

Interactions between particles are described with a pair-wise force field similar to the Lennard-Jones potential [80]:

$$\mathbf{f}_{ij} = C_0 \left[\left(\frac{r_0}{|\mathbf{r}_{ij}|} \right)^{p_1} - \left(\frac{r_0}{|\mathbf{r}_{ij}|} \right)^{p_2} \right] \frac{\mathbf{r}_{ij}}{|\mathbf{r}_{ij}|}, \quad \text{Eq. 5-24}$$

where $\mathbf{r}_{ij} = \mathbf{r}_i - \mathbf{r}_j$, r_0 is the initial distance between two different particles i and j . In this case, $p_1 = 12$, $p_2 = 6$, C_0 is an adjustable constant.

5.2.2.4 Velocity Evaluation

The motion of the particle i is described in the equation below[82]:

$$\frac{dr_i}{dt} = v_i + \epsilon \sum_j m_j \left(\frac{v_j - v_i}{\bar{\rho}_{ij}} \right) W_{ij}, \quad \text{Eq. 5-25}$$

in which, ϵ ($0 \leq \epsilon \leq 1$ according to different case) is a factor that averages the velocity of influence.

5.3 Results and Discussion

The three-dimensional model of the anesthetic injection was developed according to the procedures detailed in the Introduction. This section will discuss the results from the Spectral Element Method (SEM) and the Smoothed Particle Hydrodynamics (SPH) Method.

5.3.1 Results for the SEM

As it is mentioned before, the simulation of the solution flowing from the syringe into human skin is divided into two parts. In this section the shape of the needle and some suitable models for porous media will be determined by comparing the numerical results and their costs.

5.3.1.1 Solution for Simulation of Micro-Needle

In the first part, the length of the needle is set at 1 mm, the radii are set as 50 μm at the bottom and 25 μm at the sharp (for rectangular cross-section, the widths of bottom and sharp are set as 50 μm and 25 μm). We set the flow as the pressure driven flow. As a result, the initial velocity at the inlet is set at 0.0, the pressure of the inlet is set at 10.0 kPa, and the outlet is imposed with the Neumann boundary condition.

Figure 5-1 shows the models of the needles with circular and rectangular cross sections. By comparing the results from both of these two models, and mapping their data as the initial conditions to our second part of the simulation, numerical solution of the Darcy-Brinkman equations, the results are almost the same. In this section, we take the data of the pressure and velocity from the circular cross-section.

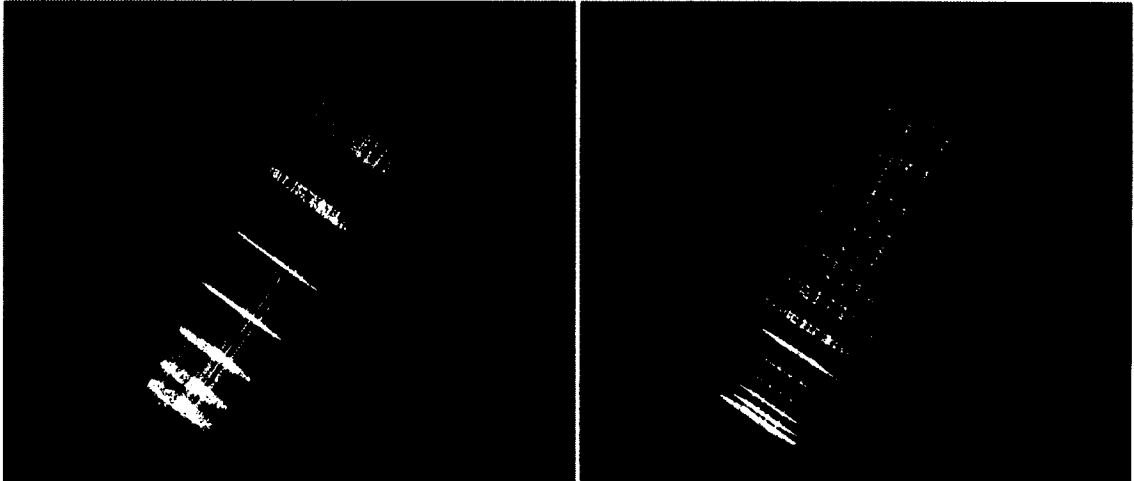


Figure 5-1: The models of needles with circular and rectangular cross sections.

After the results are converged, **Figure 5-2** shows the velocity contour on xz-cross section, with the initial pressure of 10 kPa, the normalized velocity comes with a maximum value of 35.9 at the outlet.

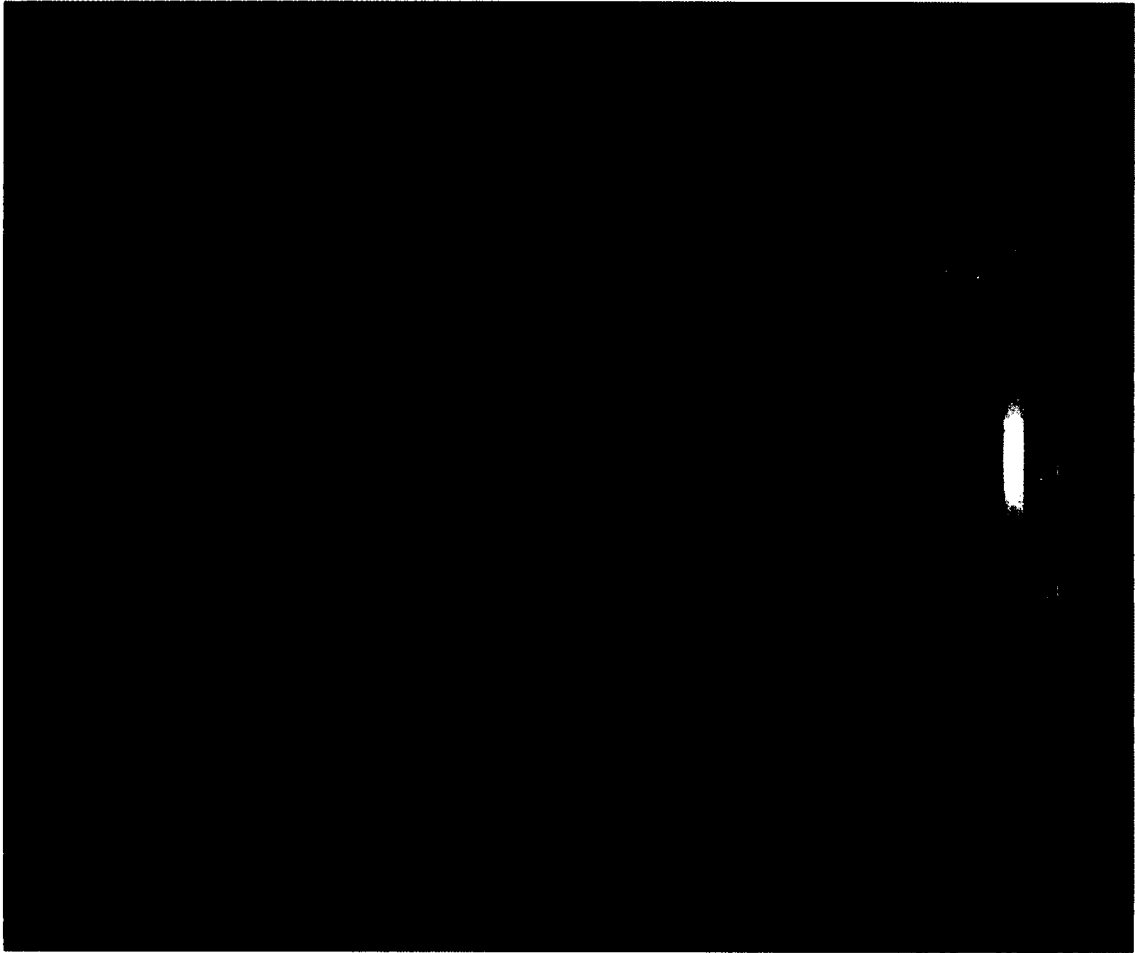


Figure 5-2: The velocity on z direction on xz-cross section.

Figure 5-3 shows the contour of pressure on the xz-cross section. Since the pressure is the only driving force of this model, the pressure reduced from its maximum value from the inlet to its minimum value at the outlet.



Figure 5-3: The pressure on xz-cross section.

Figure 5-4 shows the normalized velocity of z-direction at the inlet and the outlet. Due to the slip boundary conditions, the velocity near the wall is much smaller than at the middle area.

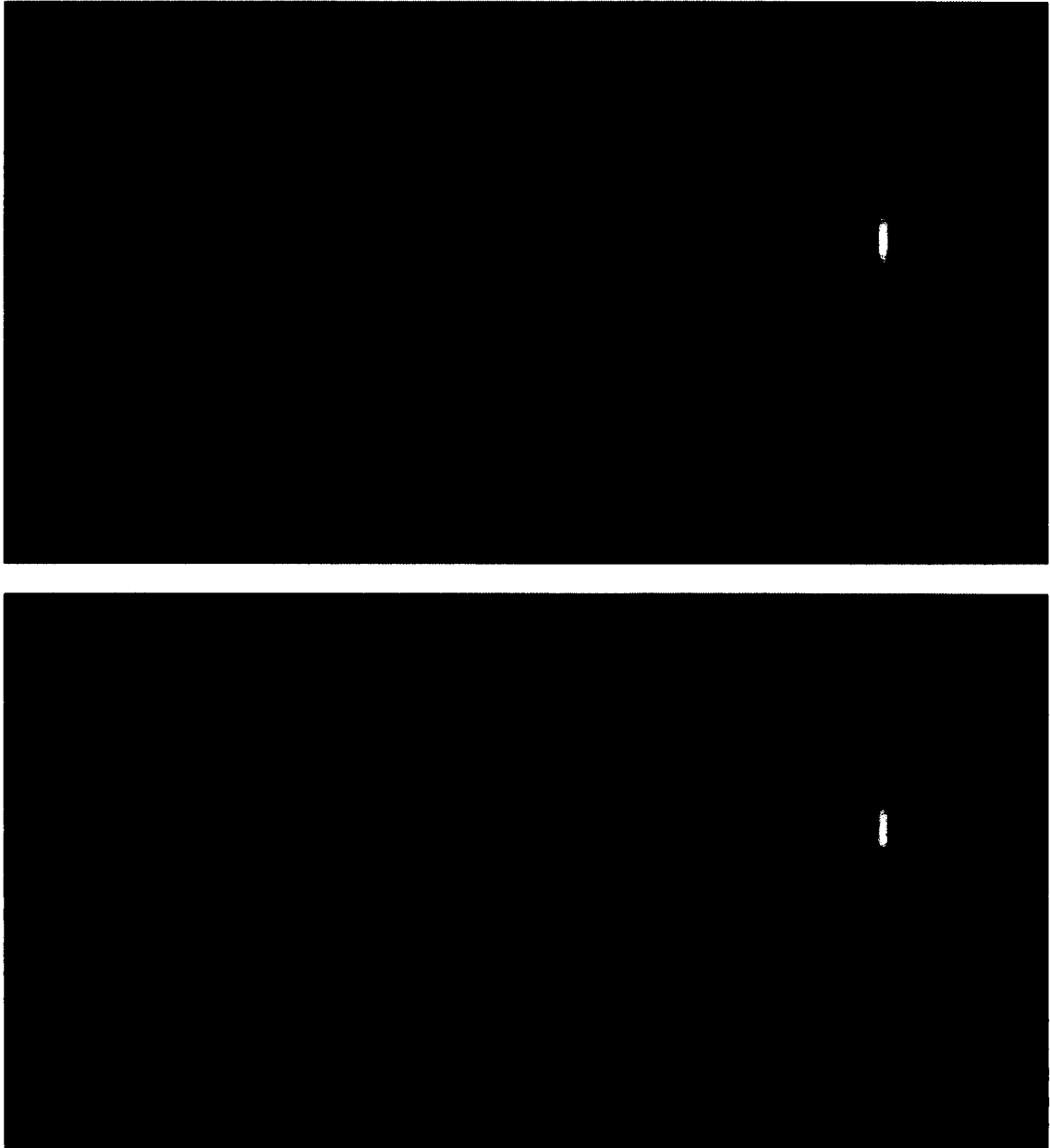


Figure 5-4: The contours of velocity on z-direction at the inlet (up) and outlet (down).

Figure 5-5 shows the contours of pressure at the inlet and outlet of the needle. **Figure 5-2** to **Figure 5-5** come from the simulation of the model with third order. As mentioned before, the data from the outlet of the needle will project to become the input boundary and initial conditions of the next model. The polynomial order of the

basis functions need to be the same. For example, the third order scheme of the needle can only match the third order model of human skin. When the fifth order simulation for human skin is analyzed, the order for the needle will also be increased to the fifth order.

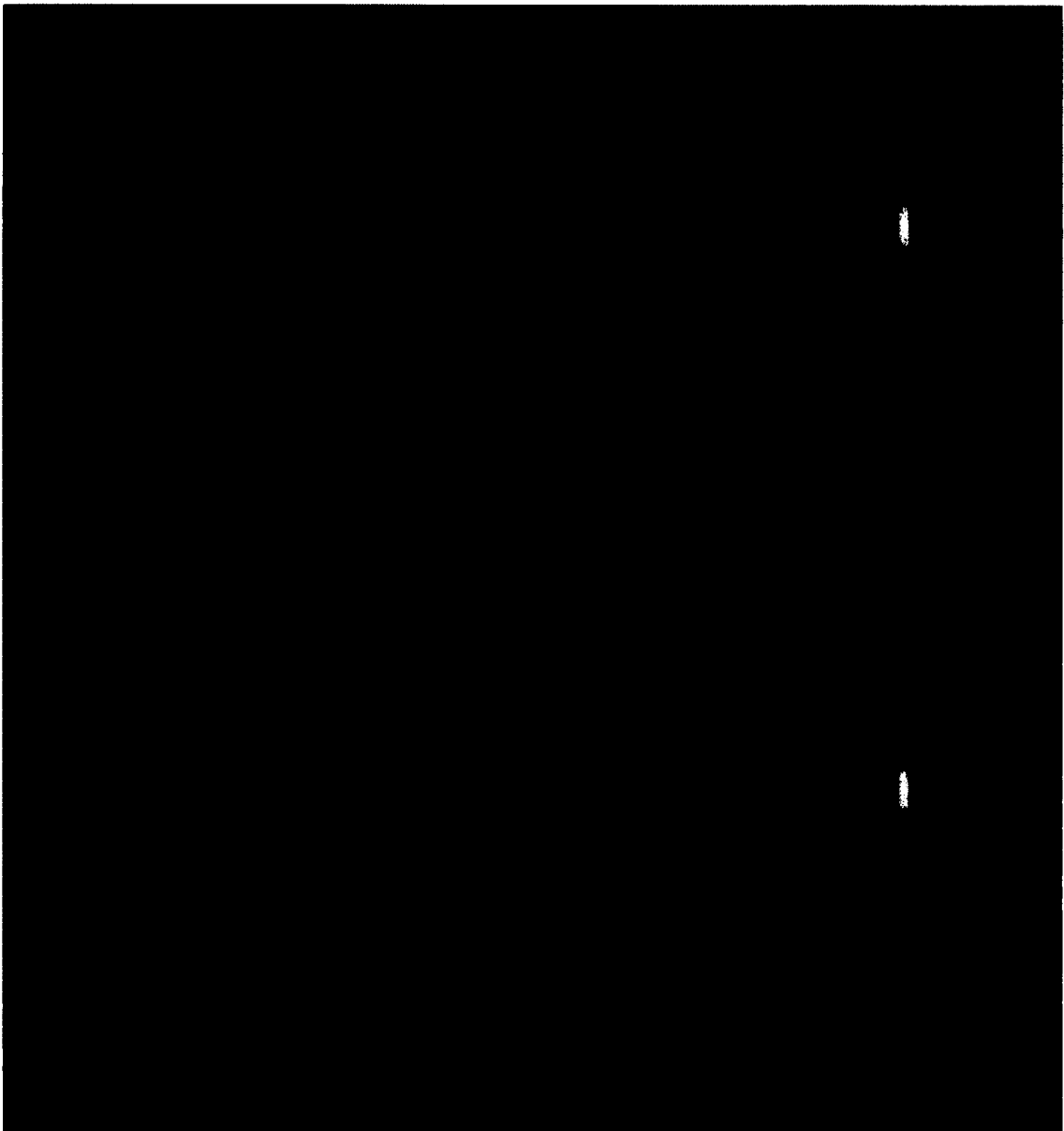


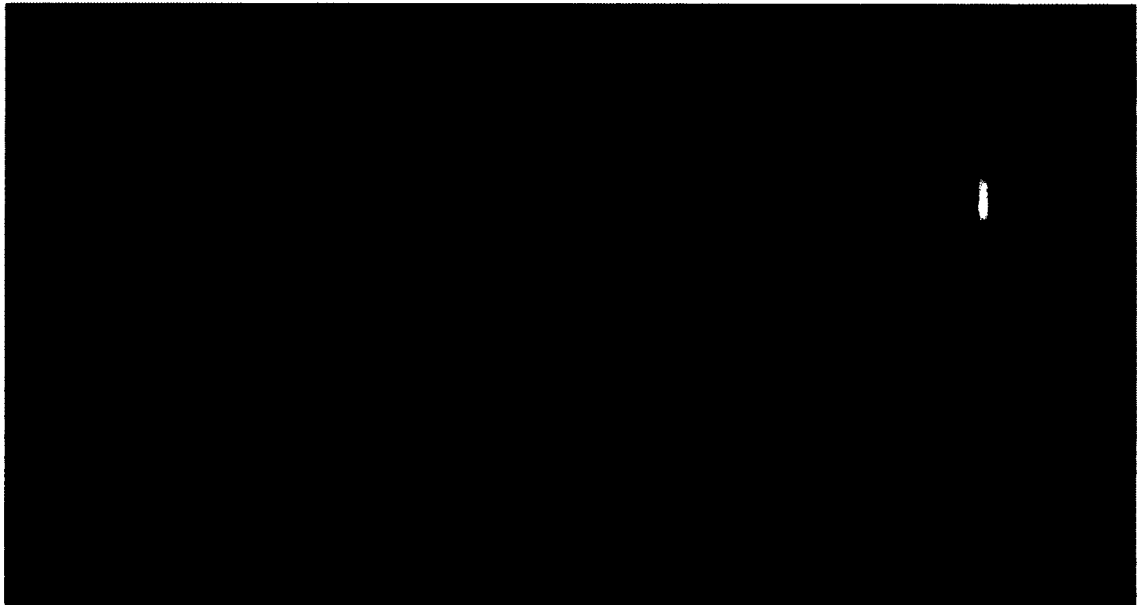
Figure 5-5: The contours of pressure at the inlet (up) and outlet (down).

5.3.1.2 Solution for Simulation of Human Skin

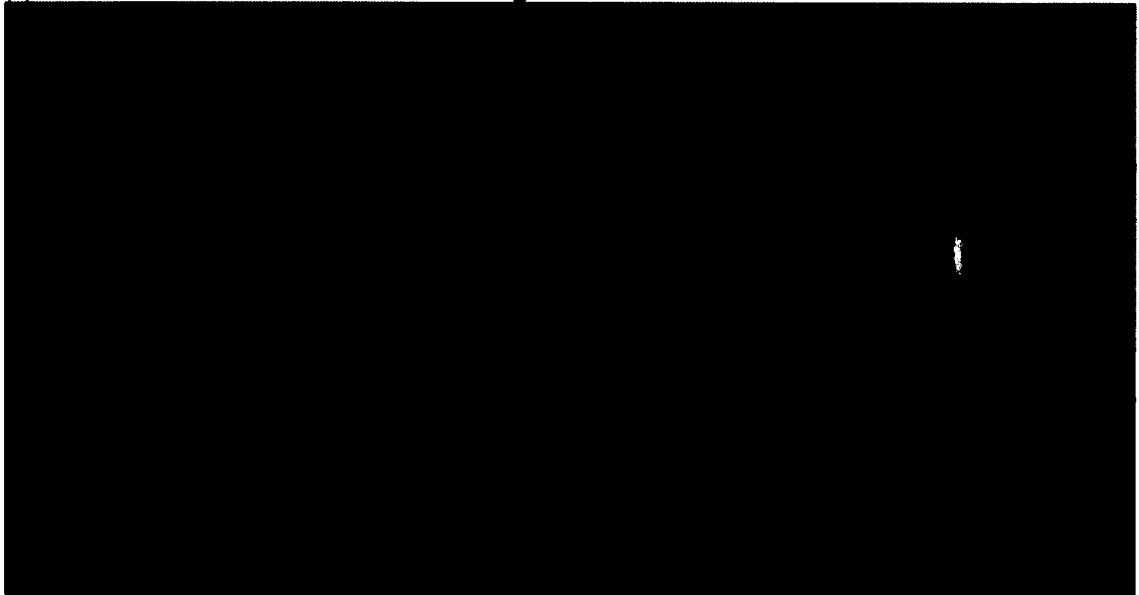
In this section, human skin is simplified as a cylinder. The top of the cylinder is treated as the cross section of the skin where needle pierces. The bottom represents the interface of dermis and fat layer. In this case, we do not need to simulate all these areas from the surface of the skin to the bottom of the fat layer. It can largely reduce the number of elements in our models, which in turn will save time on running the code. There are two different schemes for simulation. The first one is single needle with the same number of elements and different order of the basis functions and initial conditions. The other one is multiple needles with a different number of elements, and the same order of the basis functions and initial conditions.

5.3.1.2.1 Single Needle

Figure 5-6(a) shows the contour map of the initial concentration for the single needle case. At time = 0, the initial concentration at the surface of the skin is set at 42.67 mol/m³ according to **Table 5-1**. By doing some tests on different models, we find that by changing the ratio of the needle's input area to the area of the x-y cross section of the model, the result's range (maximum and minimum values of models) will also be seriously changed (see **Figure 5-7**). The result will become convergent when the ratio decreases to about 0.05. However, if we built models with a ratio of 0.05 or less, it will largely increase the number of elements or the order of the basis functions, which will take a much longer time to run our codes.

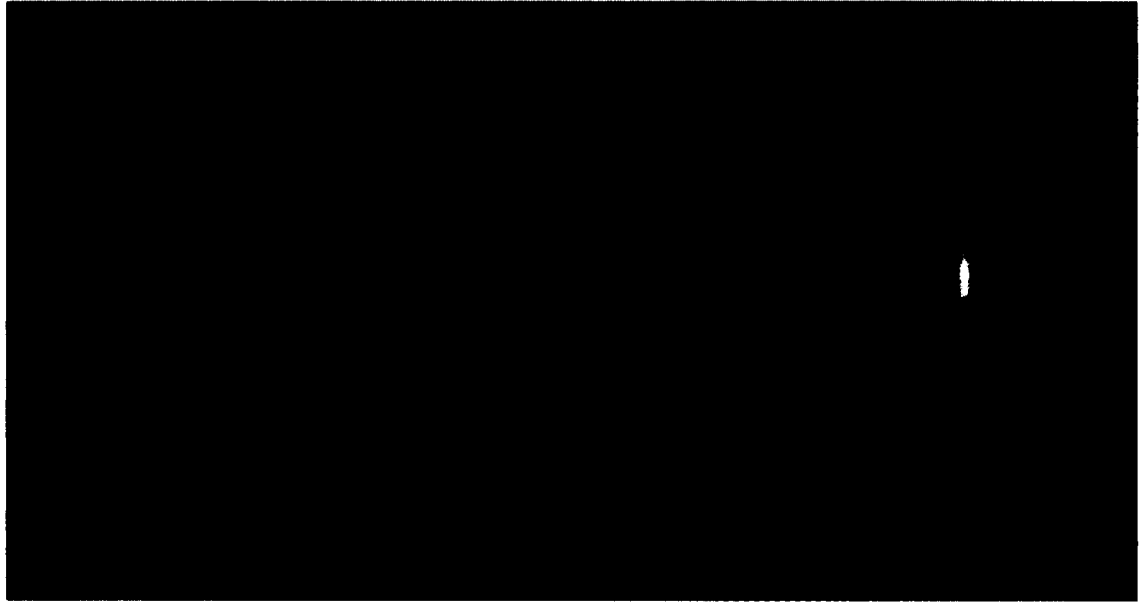


(a): The model of human skin with a single needle at a ratio of 0.05.

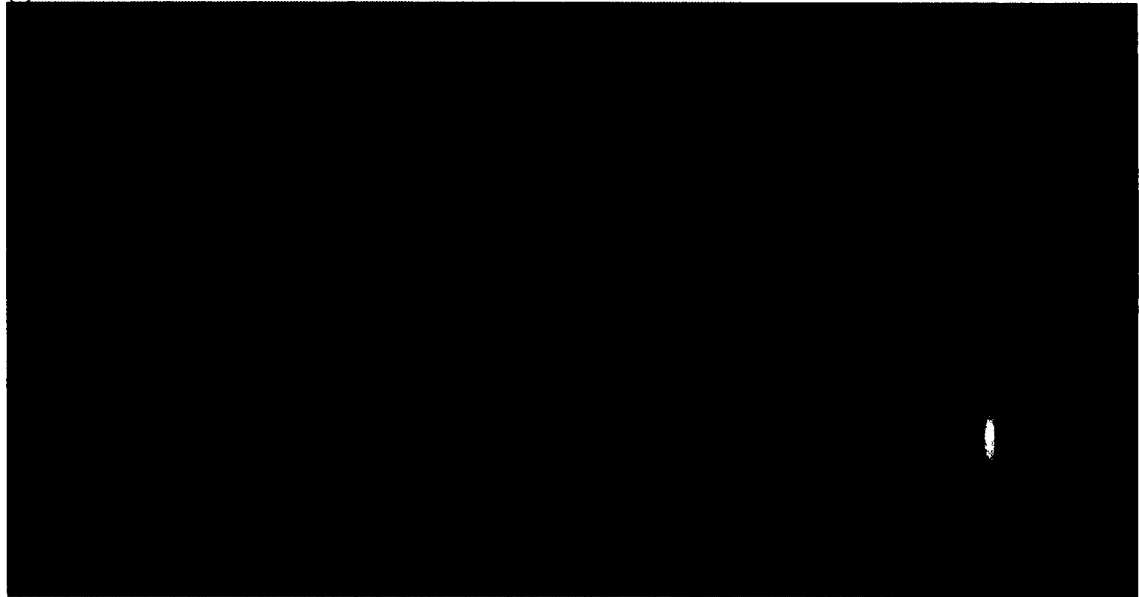


(b): The model of human skin with a single needle at a ratio of 0.1.

Figure 5-6: The initial contours of concentration with a different ratio of a needle's input area to the area of x-y cross section of model.



(a): The concentration of fourth order bases and 75 elements with a ratio of 0.05.



(b): The concentration of sixth order bases and 45 elements with a ratio of 0.1.

Figure 5-7: Contour maps for single-needle model at $t = 60$ sections with different ratios of needle input area to the area of the x-y cross section.

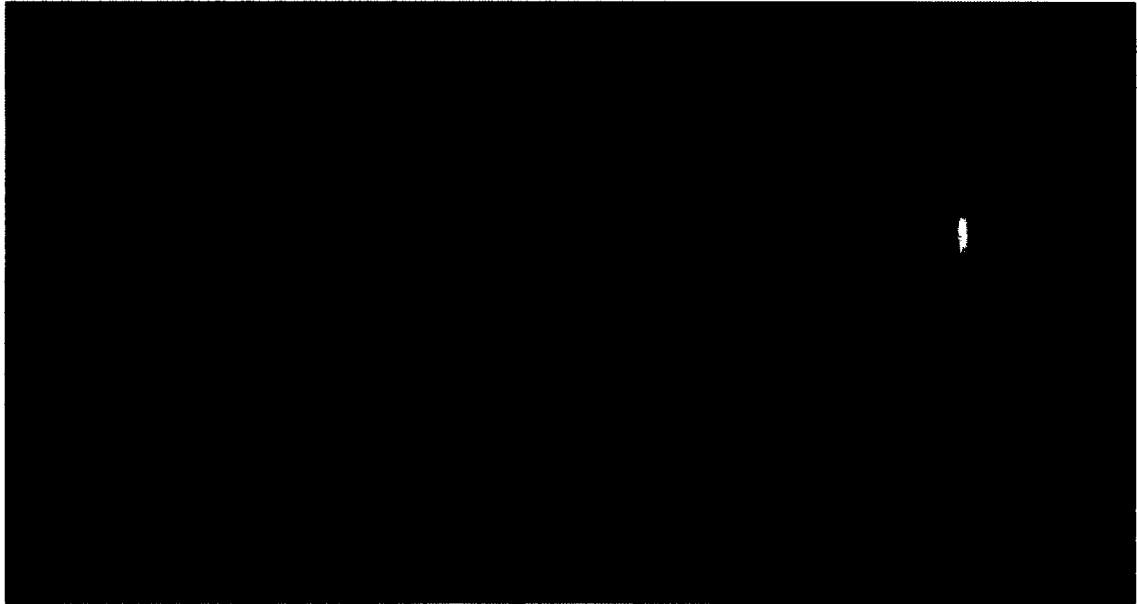
In **Figures 5-7 (a)** and **(b)**, the maximum and minimum concentrations of the first cases are 6.730×10^{-4} and 1.000×10^{-5} mol/m³. On the other hand, for the second case the maximum and minimum concentrations are 7.318×10^{-4} and 5.843×10^{-4} mol/m³, respectively. It seems that for this type of model, with every parameter

due to references, the result for the concentration is much less than its necessary value $4.267 \times 10^{-3} \text{ mol/m}^3$. Since the critical area for this model is the concentration at the interface between the dermis and the fat layers, we decide that instead of reducing the ratio, we will focus on the concentration of the critical area directly under the needle. To improve the result for our model, there are two possible ways. The first one is increasing the initial concentration, and the second way is keeping the sizes of the model but using multiple needles. Since even if the concentration requirement can be achieved by the first approach, the practical application needs not only concentration, but also enough dose. We decide to develop a model with four micro needles on top. Simultaneously, in this model, the critical area is the cross section of the dermis-fat layer interface under and between the needles. We try to find the concentration of the drug in this area, which is affected by multiple needles. The following paragraph will discuss the results from the models with four needles.

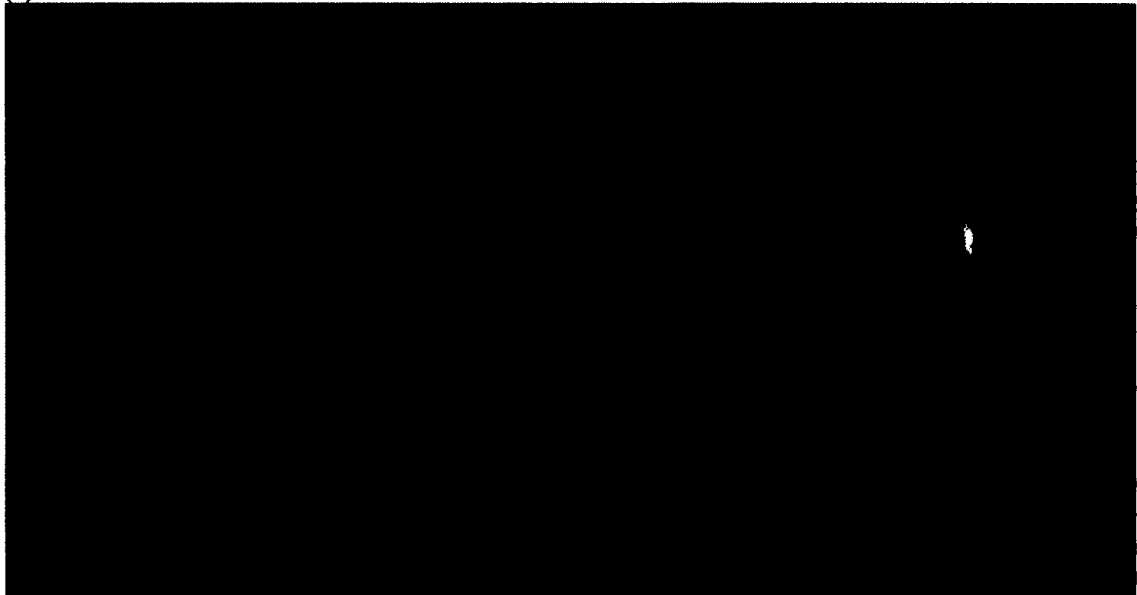
5.3.1.2.2 Multiple Needles

Based on the Single-Needle model, we develop another model with 4 needles.

Figure 5-8 shows the modified models of the sixth order bases with 75 and 243 elements. By comparing the results from these two models, the maximum and minimum concentration have the differences of 4.32% and 4.12%; however, the running time of the code increased from 2:28:37 to 5:54:13. Due to this fact, it seems unnecessary to increase the number of elements or the order of the basis functions anymore.



(a): The model with 75 elements.

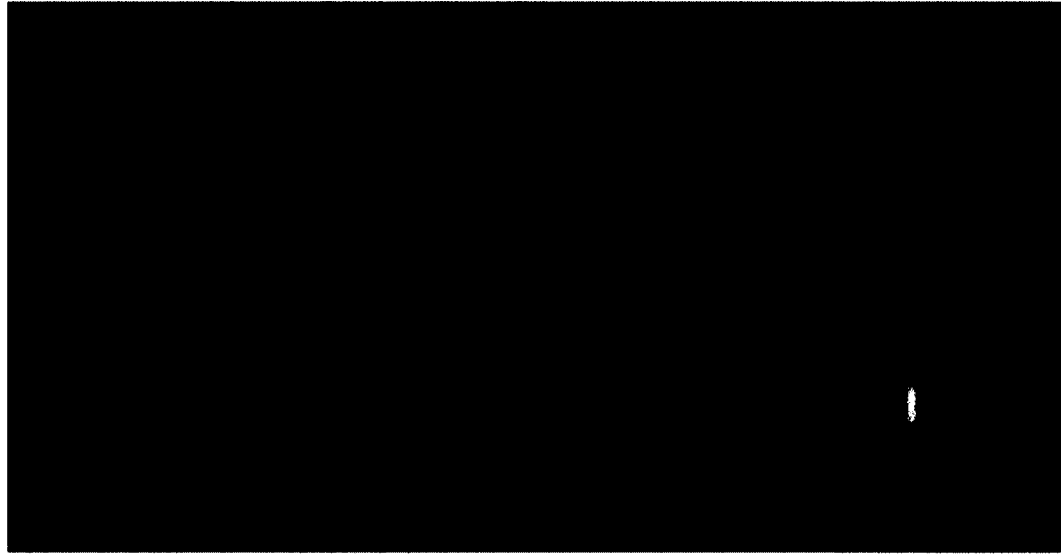


(b): The model with 243 elements.

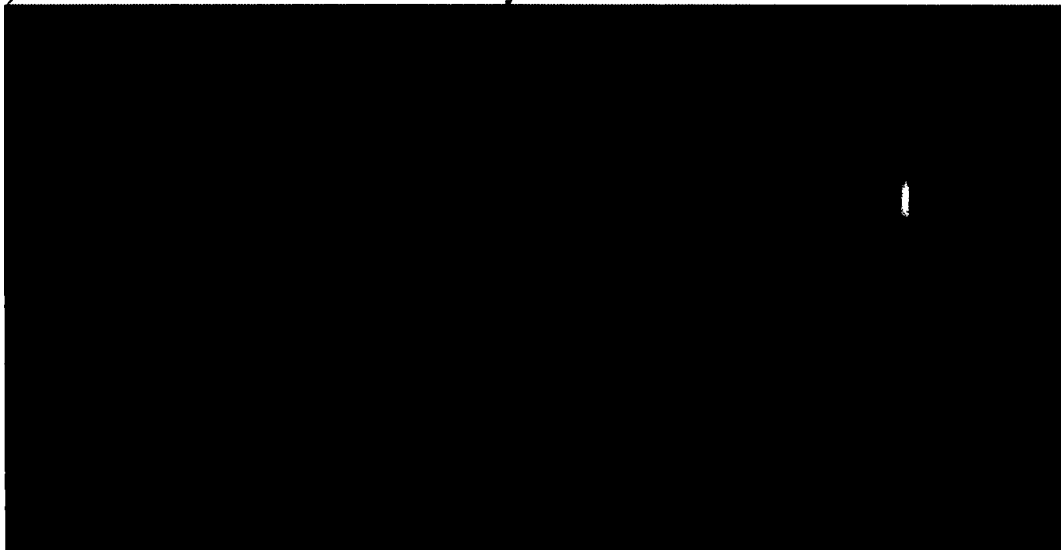
Figure 5-8: The initial models of human skin with 4 needles.

After the result converges, the contour maps of concentration with the 6th order accuracy are shown in **Figure 5-9**. In **Figure 5-9(a)**, the minimum value of concentration is $1.670 \times 10^{-3} \text{ mol/m}^3$, which is lower than the minimum necessary value, while the maximum concentration is $5.296 \times 10^{-3} \text{ mol/m}^3$, which is beyond the required value.

Moreover, from **Figure 5-9(b)**, the highest concentration located at the middle of the critical layer is also the middle of the 4 needles. The value is $5.151 \times 10^{-3} \text{ mol/m}^3$, which is 20.71% larger than the required concentration.



(a) Concentration with 6th order accuracy.



(b) Concentration at interface of the dermis and the fat layer.

Figure 5-9: Contour maps for 4-needle model at $t = 60$ sections.

5.3.2 Results for SPH

In this section, we simulate a two-dimensional SPH model for the micro needle and compare the results with other modeling data. The total number of drug particles is

1200. Due to the effect of body fluids, a 0.0005 N downward force is added on the drug particles. The drug particles and porous media particles have the same value of the mass. Blue particles are used to represent drug molecules, while white particles as a random distribution of the fixed point are used to simulate the porous medium. After the micro needle pierces the surface of the skin, particles of the internal drug will go through the porous medium and then get into the capillaries and transport to all parts of the body via blood flow. **Figure 5-10(a)** indicates the initial conditions for the micro needle simulation. In **Figure 5-10(b)** and **Figure 5-10(c)**, drug particles dispersed in most of the upper part. With time increasing **Figure 5-10(d)**, drug particles dispersed everywhere in the porous medium. **Figure 5-11** is the number of particles with a depth beyond 2000 μm , which equals to the concentration change in the lower part of the middle. It is similar compared with [71] which come from the spectral element method. SPH model has a 0.0005 N downward force which signifies this model is closer to the actual situation. There are still some reasons that cause system errors. Firstly, error is caused by using fixed random distribution particles to build the dermal layer of the porous medium structure. Secondly, due to random distribution of the particles, the results have small differences every time. Thirdly, for the continuous modeling, the permeability of the skin can be defined exactly by a parameter; however, for the discrete modeling, it is hard to control this parameter with accurate measurement.

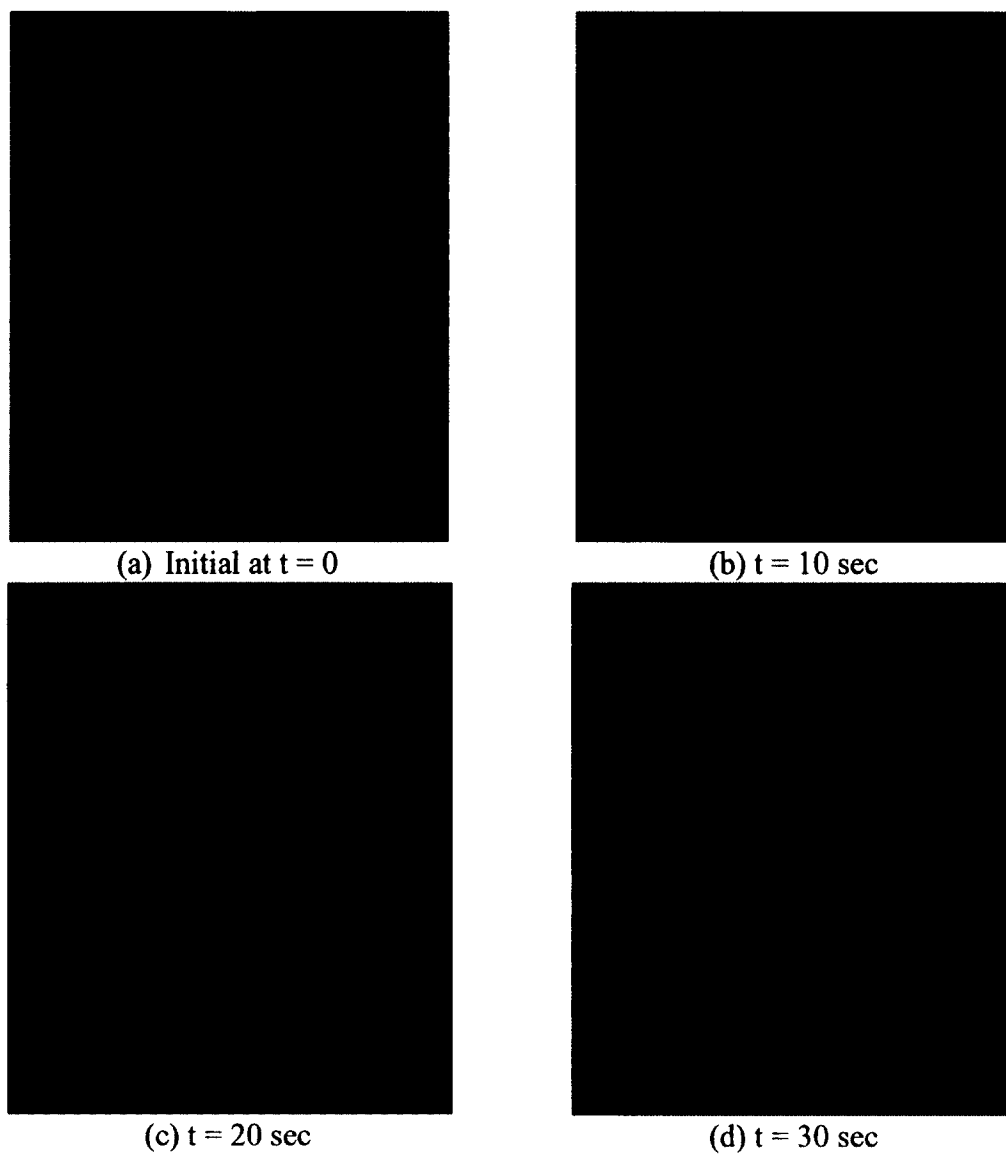


Figure 5-10: The motion process of drug molecules.

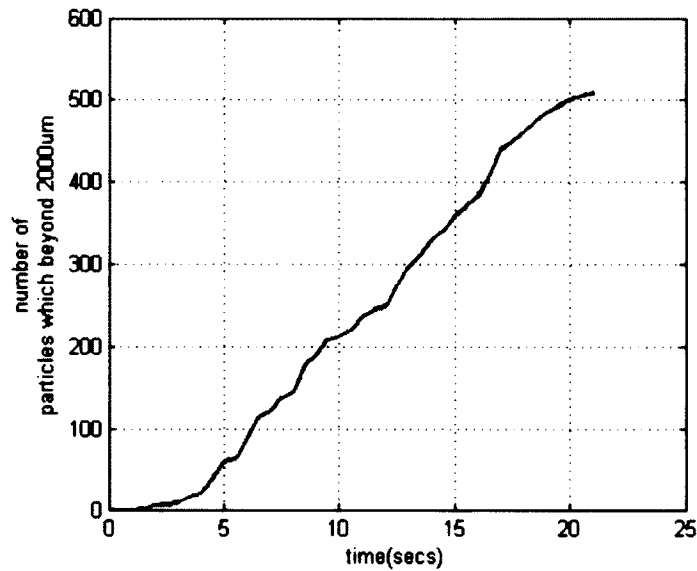


Figure 5-11: The number of particles that has a depth beyond 2000 μm .

5.4 Conclusions

Compared with traditional injection syringes, micro needles are painless, easy to operate, and a possible alternative to avoid the spreading of blood borne infections. To search online, there are already micro needle products. Different kinds and shapes of needles [81, 82] and their clinical trials [83] are discussed in detail based on experimental tests and investigations. In this paper, numerical methods with high order accuracy are conducted to show a good agreement with these reference experimental data.

This paper developed virtual models to simulate the flux of Lidocaine from the needle into human skin. The drug in the micro needle is simulated as pressure driven Navier-Stokes equations with slip boundary condition. Also drug spread in human skin is treated as the Darcy-Brinkman equations. Since there are not too many numerical results to compare with, we do convergent tests for both h-refinement, p-refinement (SEM), and

discrete method (SPH). The result shows the micro needle patch that with the current parameters, the drug can fully transfer to the required concentration.

At the same time, our two-dimensional model of the SPH method also shows the match of concentration at the interface of the dermis and the fat layers with SEM and reference. The differences happen due to the initial setting of the model. Since there is a very small initial and boundary condition of pressure, all the drag particles are driven towards for the bottom of the model. To minimize the error occurring by this setting, we just account for the number of particles moving through the critical section during 0 to 25 seconds. The results show that at 20 seconds, the number of drag particles below the interface satisfies the requirement.

CHAPTER 6

DISCONTINUOUS GALERKIN SIMULATION OF HYPERBOLIC FLOW

6.1 Introduction

The DG-FEM in this chapter is used to simulate the models with incompressible Navier-Stokes equations [84]. A two-dimensional case of a circle inside a straight channel, and a three-dimensional case of a sphere inside a rectangular channel will be presented.

6.2 Numerical Methods

The incompressible Navier-Stokes equations are considered in this chapter.

$$\rho \left(\frac{\partial \mathbf{u}}{\partial t} + (\mathbf{u} \cdot \nabla) \mathbf{u} \right) = -\nabla p + \mu \nabla^2 \mathbf{u} = 0, \quad \text{Eq. 6-1}$$

$$\nabla \cdot \mathbf{u} = 0, \text{ on } \partial\Omega, \quad \text{Eq. 6-2}$$

in Eq. 6-1, the body force \mathbf{f} is ignored.

6.2.1 Time Splitting

In our code, Eq. 6-1 is divided into two parts. The pressure and velocity are calculated separately by the time splitting scheme of the second order Adams-Bashforth scheme:

$$\frac{\gamma \tilde{\mathbf{u}} - \alpha_0 \mathbf{u}^n - \alpha_1 \mathbf{u}^{n-1}}{\Delta t} = -\beta_0 \nabla \cdot \mathbf{F}^n - \beta_1 \nabla \cdot \mathbf{F}^{n-1}, \quad \text{Eq. 6-3}$$

in which \mathbf{F} is the flux form of convection. The two-dimensional form as an example is shown in the equation below:

$$\mathbf{F} = \begin{bmatrix} u^2 & uv \\ uv & v^2 \end{bmatrix}. \quad \text{Eq. 6-4}$$

Therefore, the term of the internal source for pressure is solved as a Poisson equation in the function of velocity \mathbf{u} :

$$\nabla \cdot \bar{\mathbf{u}} = 0, \quad \text{Eq. 6-5}$$

$$\nabla^2 \bar{p}^{n+1} = \frac{\gamma}{\Delta t} \nabla \cdot \bar{\mathbf{u}}, \quad \text{Eq. 6-6}$$

in which the $\bar{\mathbf{u}}$ and \bar{p} are the intermediate velocity field that is updated by:

$$\gamma \frac{\bar{\mathbf{u}} - \mathbf{u}}{\Delta t} = -\nabla \bar{p}^{n+1}. \quad \text{Eq. 6-7}$$

The implicit integration of the viscous term is:

$$\gamma \frac{\mathbf{u}^{n+1} - \bar{\mathbf{u}}}{\Delta t} = \frac{\mu}{\rho} \Delta \mathbf{u}^{n+1}, \quad \text{Eq. 6-8}$$

so by combining Eq. 6-3, Eq. 6-7, and Eq. 6-8, we obtain the second order scheme in time:

$$\begin{aligned} & \frac{\gamma \mathbf{u}^{n+1} - \alpha_0 \mathbf{u}^n - \alpha_1 \mathbf{u}^{n-1}}{\Delta t} \\ & = -\beta_0 \nabla \cdot \mathbf{F}^n - \beta_1 \nabla \cdot \mathbf{F}^{n-1} - \nabla \bar{p}^{n+1} + \frac{\mu}{\rho} \Delta \mathbf{u}^{n+1}. \end{aligned} \quad \text{Eq. 6-9}$$

6.2.2 Internal Penalty Flux

As discussed in Section 2.2.1, the internal penalty flux required to analyze the jumps between the convection time steps.

6.3 Results and Discussions

6.3.1 Two-dimensional simulation of a low Reynolds number flow

In this section, a two-dimensional simulation of the flow passing around a circle inside a straight channel is presented. The model is designed with the normalized size of width 0.4, length 2.0, with a circle's diameter of 0.1. The slip boundary condition is considered at the walls of the channel and the circle's surface. The Neumann boundary condition of $\frac{\partial p}{\partial n} = 0$ is conducted on the walls and the inlet, and at the outlet, the pressure p is set at 0. For the velocity, the initial condition for the inlet is $\mathbf{u} = \sin(\pi t/8)(6y(0.4 - y), 0)$, $0 \leq y \leq 0.4$, and at the outlet, the Neumann boundary condition for velocity is $\frac{\partial \mathbf{u}}{\partial n} = 0$. The Reynolds number in this case is set at 10, with $\Delta t = 0.001$. The simulation is solved with a polynomial order of 3 and element number of 552. **Figure 6-1** to **Figure 6-3** show the velocity on the x and y direction, and the pressure at time $t = 2s$. The results are highly matched when compared with [85].

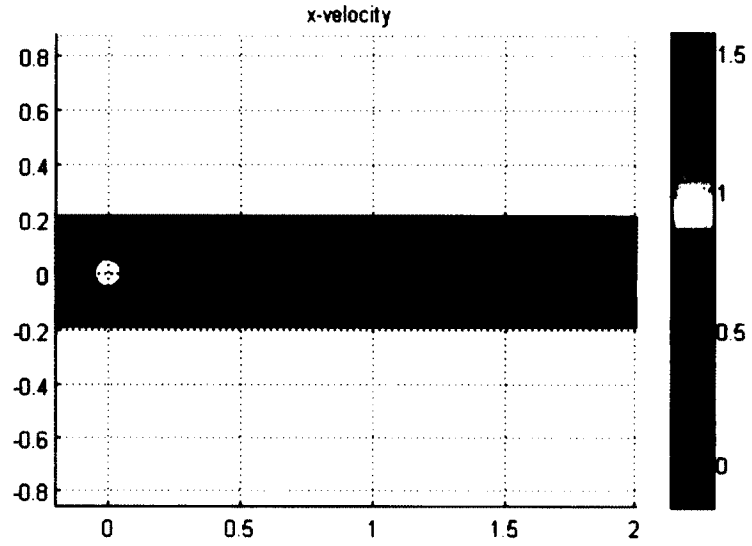


Figure 6-1: The velocity on x-direction at $t = 2s$.

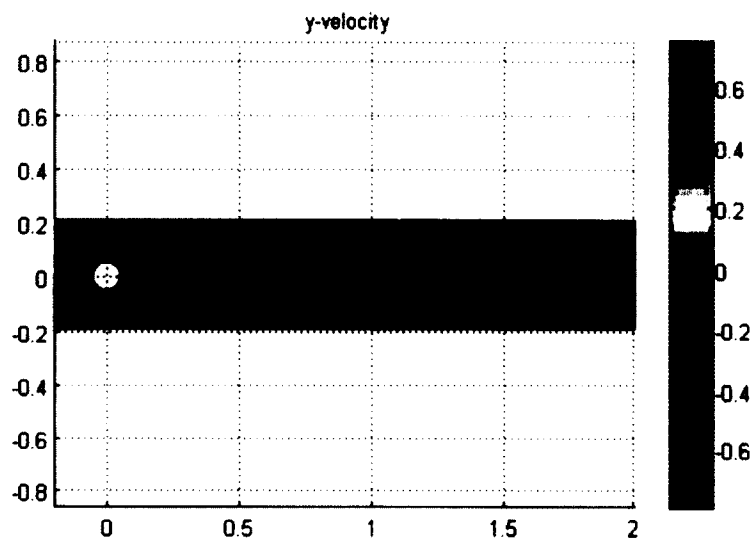


Figure 6-2: The velocity on y-direction at $t = 2s$.

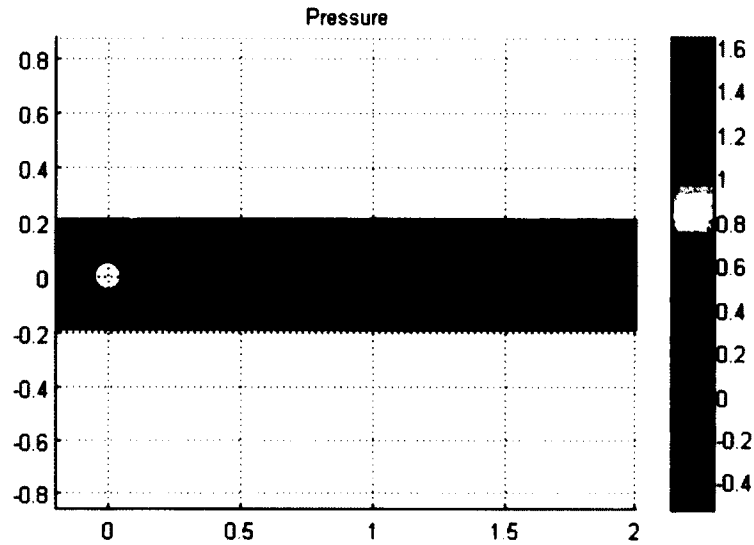


Figure 6-3: The pressure at $t = 2s$.

6.3.2 Three-dimensional Simulation with a Flow with Reynolds Number of 200

In this section, a three-dimensional model with a sphere inside a straight channel is generated. The mesh is built with $0 \leq x \leq 6$, $-3 \leq y \leq 3$, $-4 \leq z \leq 10$. A sphere with a radius of 1.0 is located at $x = 3$, $y = 0$, and $z = 0$. The non-slip boundary condition is set at the walls of the channel and the sphere. At the inlet, the velocity on z-direction is set at 10 m/s at the top and linearly reduces to 0 at the bottom. At the same time, at the inlet, the Neumann boundary condition of $\frac{\partial u}{\partial n} = 0$ is defined. For the pressure, Dirichlet boundary condition of $p = 0$ is set at the outlet, while, at the wall and inlet, the Neumann boundary condition is imposed as $\frac{\partial p}{\partial n} = 0$. **Figure 6-4** presents the contours of the velocity and pressure on the z-direction. Three slices, which are the cross section at $x = 2.99$, $y = 0.01$, and $z = 0.01$, are shown here. Moreover, when the Reynolds number is larger, we are more interested in the vorticity. **Figure 6-5** shows the contours of the

velocity on the z-direction and the related vorticity on the yz-cross section at $x = 2.99$.

There are streamlines of vorticity that can be noticed, although the Reynolds number is only 200. **Table 6-1** below shows the comparison of the results with increasing polynomial order.

Table 6-1: The maximum velocity (m/s) and pressure (Pa) on cross section of $x = 3$ due to different order of basis function.

Order	Maximum u	Maximum v	Maximum w	Maximum p
3	0.837	2.216	5.935	16.652
4	0.825	2.199	5.813	16.620
5	0.844	2.236	6.012	16.691

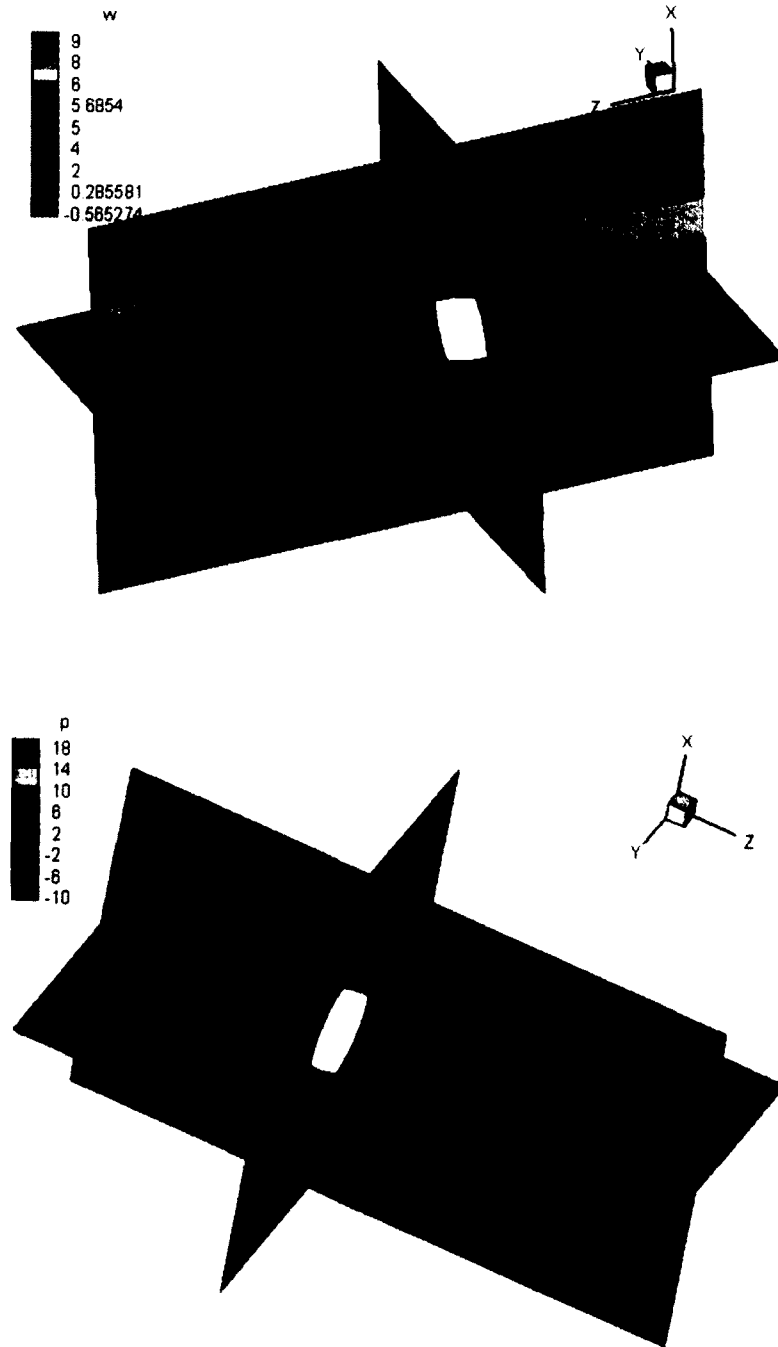


Figure 6-4: The Three-dimensional model of flow passing a sphere inside a straight channel.

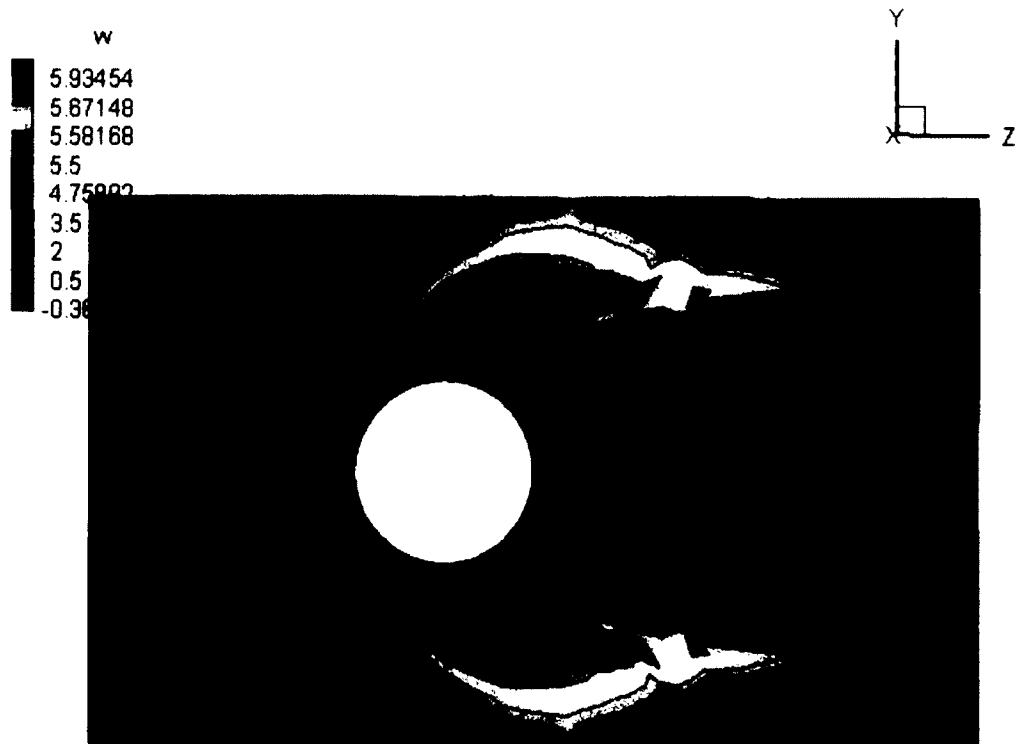


Figure 6-5: The contours of velocity on the z -direction and its streamline.

6.4 Conclusions

The two models presented in this chapter show numerical simulations solved by the DG-FEM scheme. The first case is generated with the same size and boundary and initial conditions of the existing reference data to prove the accuracy of this code. The second case shows that this scheme can simulate the model with a relatively high Reynolds number.

When the number of elements or polynomial order of the basis functions increased, the running time for simulation increased even longer. The fifth order model

with 1552 elements of three-dimensional scheme needs almost a whole day to run on an i-5 processor, with 8 GB memory. As a result, it seems that the parallel or other high performance computing will be needed if we plan to have research on models with the Reynolds number over 2000 or even larger.

CHAPTER 7

CONCLUSIONS AND FUTURE WORK

7.1 Conclusions

In this dissertation, two kinds of numerical approaches are discussed for solving flows with different boundary conditions and scales in complex geometries and for complex physics. In Chapter 2, literature reviews for both the spectral element method and the discontinuous Galerkin finite element method are discussed separately. In Chapter 3, two three-dimensional cases of the environmental flow are presented to show the high order accuracy of the SEM for solving the Navier-Stokes equations. Chapter 4 is the modeling of electro osmotic flow by the SEM. Here, the slip boundary condition and body force caused by electrical potential is imposed to the two-dimensional Navier-Stokes equations. Moreover, in Chapter 5, a three-dimensional simulation of the medical application is processed, and the result is compared with the reference data and our discrete modeling. To solve problems with a high Reynolds number, the DG-FEM scheme is chosen and discussed in Chapter 6.

7.2 Future Work

Future work will focus on the following areas:

1. The SEM solver for the micro flow problems need to be developed to three-dimensional availability;

2. The general DG-FEM solver for three-dimensional cases;
3. Research for hyperbolic flows with high Reynolds numbers is needed with the application of high performance computing.

APPENDIX

IMPORTANT FUNCTIONS AND LIBRARY

A. pabx.m

```
function f=pabx(alf,bet,ord,x)
p(1,:)=factorial(x*0);
p(2,:)=0.5*(alf-bet+(alf+bet+2)*x);
for i=1:ord-1
    a1=2*(i+1)*(i+alf+bet+1)*(2*i+alf+bet);
    a2=(2*i+alf+bet+1)*(alf^2-bet^2);
    a3=(2*i+alf+bet)*(2*i+alf+bet+1)*(2*i+alf+bet+2);
    a4=2*(i+alf)*(i+bet)*(2*i+alf+bet+2);
    p(i+2,:)=((a2+a3*x).*p(i+1,:)-a4*p(i,:))/a1;
end
f=p(ord+1,:);
```

B. dpabx.m

```
function f=dpabx(alf,bet,ord,x)
if(ord==0)
    f=x*0;
else
    f=1/2*(alf+bet+ord+1)*pabx(alf+1,bet+1,ord-1,x);
end
```

C. zeros.m

```
function f=zeros(alf,bet,ord)
for i=0:ord-1
    xz(i+1)=-cos((2*i+1)*pi/2/ord);
end

for k=1:ord
    r=xz(k);
    if(k>1)
        r=(r+xz(k-1))/2;
    end
end
```

```

for j=1:100
    s=0;
    for ii=1:k-1
        s=s+1/(r-xz(ii));
    end
    del=-pabx(alf,bet,ord,r)/(dpabx(alf,bet,ord,r)-pabx(alf,bet,ord,r)*s);
    r=r+del;
    if (del<1e-10)
        break;
    end
end
xz(k)=r;
end
f=xz;

```

D. GLJzp.m

```

function f=GLJzp(alf,bet,ord)%% calculation of the zeros points
zp(1)=-1;
zp(ord)=1;
zp(2:ord-1)=epzero(alf+1,bet+1,ord-2);
f=zp;

```

E. GLJwe.m

```

function f=GLJwe(alf,bet,ord)
zp=GLJzp(alf,bet,ord);
cord=2^(alf+bet+1)*prod(1:alf+ord-1)*prod(1:bet+ord-1)/(ord-1)/prod(1:ord-1)/prod(1:alf+bet+ord)./(pabx(alf,bet,ord-1,zp).^2);
we(2:ord-1)=cord(2:ord-1);
we(1)=(bet+1)*cord(1);
we(ord)=(alf+1)*cord(ord);
f=we;

```

F. ZWGLL.h

```

#include <stdio.h>
#include <iostream>
#include <cmath>
#include <stdlib.h>
void sort(double* zeros, unsigned int dim)
{
    for ( unsigned int i= 0; i<dim-1; i++)

```

```

        for (unsigned int j= i+1; j<dim; j++)
            if ( zeros[i] > zeros[j] )
            {
                double t= zeros[i];
                zeros[i]= zeros[j];
                zeros[j]= t;
            }
    }
double JacobiPolynomial(double alpha,double beta,int n,double _x)
{
    if( n < 0)
    {
        printf("illegal order.\n");
        exit(0);
    }
    if (n == 0)
        return 1;
    else if (n == 1)
        return 0.5*(alpha-beta+(alpha+beta+2)*_x);

    double a_1= 2*n*(n+alpha+beta)*(2*n-2+alpha+beta),
           a_2= (2*n-1+alpha+beta)*(alpha*alpha - beta*beta),
           a_3= (2*n-2+alpha+beta)*(2*n-1+alpha+beta)*(2*n+alpha+beta),
           a_4= 2*(n-1+alpha)*(n-1+beta)*(2*n+alpha+beta);
    return ((a_2+a_3*_x)*JacobiPolynomial(alpha,beta,n-1,_x)- \
           a_4*JacobiPolynomial(alpha,beta,n-2,_x))/a_1;
}

void zerosGuess( unsigned int order, double* zeros )
{
    if (order < 1)
        return;
    if (zeros == NULL )
    {
        printf("Null pointer.\n");
        exit(0);
    }

    unsigned int n= order+1; // zeros has n elements.
    zeros[0]= -1;
    zeros[order]= 1;

    for (int i= 2; i<order+1; i++)
        zeros[i-1]= (1-3*(n-2)/(8*(n-1)*(n-1)*(n-1)))*cos((4*i-3)* \
3.1415926/(4*(n-1)+1) );
    sort(zeros,order+1);
}

```

```

}

void computeZeros(unsigned int order,double* zeros)
{
    zerosGuess(order,zeros); // zeros has order+1 elements.

    unsigned int n= order+1;

    //LegendrePolynomial lp1(order-1),lp(order);

    for (unsigned int k= 1; k<order; k++)
    {
        double e= 0.0;
        double r= zeros[k];
        int MAX= 500;
        while(MAX-->0)
        {
            double y= (n-1)*(JacobiPolynomial(0.,0.,order-1,r)-
r*JacobiPolynomial(0.,0.,order,r)),
            dy= (2*r*y-(n-1)*n*JacobiPolynomial(0.,0.,order,r))/(1-r*r),
            ddy= (2*r*dy-(n*(n-1)-2)*y)/(1-r*r);

            e= 2*y*dy/(2*dy*dy-y*ddy);
            r -= e;
            if (-1e-10<e && e< 1e-10 || (MAX == 0)&&(-1e-6<e && e< 1e-6) )
            {
                zeros[k]= r;
                break;
            }
        }
        if (MAX < 0 )
        {
            printf("Root finding can not coverge. ! \n");
            exit(0);
        }
    }
    sort(zeros,n);
}

void ZWGLL(double* zeros, double* weights, unsigned int num) // For standard element
{
    if ( weights == NULL || num < 1)
    {
        printf("illegal order or empty pointer. \n");
        exit(0);
    }
}

```

```

//zeros= (double*)malloc(sizeof(double)*num);
computeZeros(num-1,zeros);

for (int i= 0; i<num; i++)
{
    double w= JacobiPolynomial(0.,0.,num-1,zeros[i]);
    weights[i]= 2./(num*(num-1)*w*w);
}
}

```

G. DGLL

```

void DGLL(double* M,double* DM,double Z[],int NZ,int NZD)
{
// Compute the derivative matrix D and its transpose DT
// associated with the Nth order Lagrangian interpolants
// through the NZ Gauss-Lobatto Legendre points Z.
// Note: D and DT are square matrices.
int i,j;
int N=NZ-1;
double W[LX1];
ZWGLL(Z,W,LX1);
if(NZ>65)
{
    printf("Subroutine DGLL\n");
    printf("Maximum polynomial degree = 64\n");
    printf("Polynomial degree      = %d\n",N);
}
if(NZ==1)
    *M=0.0;
double D0=N*(N+1.0)/4.0;
for(i=0;i<NZ;i++)for(j=0;j<NZ;j++)
{
    *(M+i*NZ+j)=0.0;
    if(i!=j)*(M+i*NZ+j)=PNLEG(Z[i],N)/(PNLEG(Z[j],N)*(Z[i]-Z[j]));
    if(i==j&&i==0)*(M+i*NZ+j)=-D0;
    if(i==j&&i==NZ-1)*(M+i*NZ+j)=D0;
    *(DM+j*NZ+i)=*(M+i*NZ+j);
}
}

double PNDLEG(double Z,int N)//p139
{
//Compute the derivative of the Nth order Legendre polynomial at Z.
//(Simpler than JACOBF)
//Based on the recursion formula for the Legendre polynomials.

```



```

double P3;
double P1=1.0;
double P2=Z;
double P1D=0.0;
double P2D=1.0;
double P3D=1.0;
int k;
double PNDLEG1;
for(k=1;k<N;k++)
{
P3=((2.0*k+1.0)*Z*P2-k*P1)/(k+1.0);
P3D=((2.0*k+1.0)*P2+(2.0*k+1.0)*Z*P2D-k*P1D)/(k+1.0);
P1=P2;
P2=P3;
P1D=P2D;
P2D=P3D;
}
PNDLEG1=P3D;
return PNDLEG1;
}

```

H. HGLL

```

double HGLL(int i,double Z,double ZGLL[],int NZ)
{
// Compute the value of the Lagrangian interpolant HGLL through
// the NZ Gauss-Lobatto Legendre points ZGLL at the point Z.
double EPS=pow(1.0,-8);
double HGLL1,ALFAN,DZ;
int N;
DZ=Z-ZGLL[i];
if(fabs(DZ)<EPS)
HGLL1=1.0;
else
{
N=NZ-1;
ALFAN=N*(N+1.0);
HGLL1=-((1.0-Z*Z)*PNDLEG(Z,N))/(ALFAN*PNLEG(ZGLL[i],N)*(Z-ZGLL[i]));
//if(fabs(DZ)<EPS)HGLL1=1.0;
}
printf("%f\n",HGLL1);
return HGLL1;
}

```

I. IGLLM

```

void IGLLM(double* I12,double* IT12,double Z1[],double Z2[],int NZ1,int NZ2,int
ND1,int ND2)
{
//Compute the one-dimensional interpolation operator (matrix) I12
// and its transpose IT12 for interpolating a variable from a
// Gauss-Lobatto Legendre mesh (1) to a another mesh M
// (INVEDG[27],LIST[20][LELT][15]2).
// Z1 : LZ1 Gauss-Lobatto Legendre points.
// Z2 : LZ2 points on mesh M.
//double I12[ND2][ND1],IT12[ND1][ND2];
//double Z1[ND1],Z2[ND2];
int i,j;
double ZI;
for(i=0;i<NZ2;i++)
{
ZI=Z2[i];
for(j=0;j<NZ1;j++)
{
if(i==j)
*(I12+i*NZ1+j)=1.0;
else
*(I12+i*NZ1+j)=0.0;
*(IT12+i*NZ1+j)=*(I12+j*NZ1+i);
}
}
if(NZ1==1)
{
for(i=0;i<NZ2;i++)for(j=0;j<NZ1;j++)
{*(I12+i*NZ1+j)=1.0;*(IT12+i*NZ1+j)=1.0;}
}
}

```

J. PNLEG

```

double PNLEG(double Z,int N)
{
// Compute the value of the Nth order Legendre polynomial at Z.
// (Simpler than JACOBFF)
// Based on the recursion formula for the Legendre polynomials.
double P1,P2,P3,PNLEG1;
int k;
P1=1.0;P2=Z;P3=P2;
for(k=0;k<N-1;k++)
{
P3=((2.0*(k+1.0)+1.0)*Z*P2-(k+1.0)*P1)/(k+1.0+1.0);
P1=P2;

```

```

    P2=P3;
  }
  PNLEG1=P3;
  return PNLEG1;
}

```

K. PNDLEG

```

double PNDLEG(double Z,int N)//p139
{
//Compute the derivative of the Nth order Legendre polynomial at Z.
//(Simpler than JACOBF)
//Based on the recursion formula for the Legendre polynomials.
double P3;
double P1=1.0;
double P2=Z;
double P1D=0.0;
double P2D=1.0;
double P3D=1.0;
int k;
double PNDLEG1;
for(k=1;k<N;k++)
{
  P3=((2.0*k+1.0)*Z*P2-k*P1)/(k+1.0);
  P3D=((2.0*k+1.0)*P2+(2.0*k+1.0)*Z*P2D-k*P1D)/(k+1.0);
  P1=P2;
  P2=P3;
  P1D=P2D;
  P2D=P3D;
}
PNDLEG1=P3D;
return PNDLEG1;
}

```

L. COEF

```

void COEF()
{
//Generate
// -Derivative operators,INVEDG[27],LIST[20][LELT][15]
// -Interpolation operators
// -Weights
// -Collocation Points
//Associated with the
// -Gauss-Legendre Lobatto Mesh (Suffix M1)
// -Gauss-Legendre Mesh (Suffix M2)

```

```

// (1) Gauss-Legendre Lobatto mesh (Suffix M1)
//   Generate collocation points and weights
ZWGLL(ZGM11,WXM1,LX1);
ZWGLL(ZGM12,WYM1,LY1);
ZWGLL(ZGM13,WZM1,LZ1);
int i,j,k;
for(j=0;j<LY1;j++)for(i=0;i<LX1;i++)
{
  W3M1[i][j]=WXM1[i]*WYM1[j];
}
//Compute derivative matrices
double *D=new double[LX1*LX1];
double *DT=new double[LX1*LX1];
DGLL(D,DT,ZGM11,LX1,LX1);
for(i=0;i<LX1;i++)for(j=0;j<LX1;j++)
{
  DXM1[i][j]=(D+i*LX1+j);
  DXTM1[i][j]=(DT+i*LX1+j);
}
DGLL(D,DT,ZGM12,LY1,LY1);
for(i=0;i<LX1;i++)for(j=0;j<LX1;j++)
{
  DYM1[i][j]=(D+i*LY1+j);
  DYTM1[i][j]=(DT+i*LY1+j);
}
DGLL(D,DT,ZGM13,LZ1,LZ1);
for(i=0;i<LZ1;i++)for(j=0;j<LZ1;j++)
{
  DZM1[i][j]=(D+i*LZ1+j);
  DZTM1[i][j]=(DT+i*LZ1+j);
}
// (1) Gauss-Legendre Lobatto mesh (suffix M2)
//   Generate collocation points and weights
ZWGLL(ZGM21,WXM2,LX2);
ZWGLL(ZGM22,WYM2,LY2);
ZWGLL(ZGM23,WZM2,LZ2);
// (3) Gauss-Legendre Lobatto mesh (suffix M3),,INVEDG[27],LIST[20][LELT][15]
//   Generate collocation points and weights
ZWGLL(ZGM31,WXM3,LX3);
ZWGLL(ZGM32,WYM3,LY3);
ZWGLL(ZGM33,WZM3,LZ3);
//for(k=0;k<LZ3;k++)
for(j=0;j<LY3;j++)for(i=0;i<LX3;i++)
  W3M3[i][j]=WXM3[i]*WYM3[j];
//Compute derivative matrices

```

```

DGLL(D,DT,ZGM31,LX3,LX3);
for(i=0;i<LX3;i++)for(j=0;j<LX3;j++)
{
  DXM3[i][j]=(D+i*LX3+j);
  DXTM3[i][j]=(DT+i*LX3+j);
}
DGLL(D,DT,ZGM32,LY3,LY3);
for(i=0;i<LY3;i++)for(j=0;j<LY3;j++)
{
  DYM3[i][j]=(D+i*LY3+j);
  DYTM3[i][j]=(DT+i*LY3+j);
}
DGLL(D,DT,ZGM33,LZ3,LZ3);
for(i=0;i<LZ3;i++)for(j=0;j<LZ3;j++)
{
  DZM3[i][j]=(D+i*LZ3+j);
  DZTM3[i][j]=(DT+i*LZ3+j);
}
// (4) GENERATE INTERPOLATION OPERATORS FOR THE STAGGERED MESH

IGLLM(D,DT,ZGM11,ZGM21,LX1,LX2,LX1,LX2);
for(i=0;i<LX1;i++)for(j=0;j<LX2;j++)
{
  IXM12[i][j]=(D+i*LX1+j);
  IXTM12[i][j]=(DT+i*LX1+j);
}
IGLLM(D,DT,ZGM12,ZGM22,LY1,LY2,LY1,LY2);
for(i=0;i<LY1;i++)for(j=0;j<LY2;j++)
{
  IYM12[i][j]=(D+i*LY1+j);
  IYTM12[i][j]=(DT+i*LY1+j);
}
IGLLM(D,DT,ZGM13,ZGM23,LZ1,LZ2,LZ1,LZ2);
for(i=0;i<LZ2;i++)for(j=0;j<LZ1;j++)
{
  IZM12[i][j]=(D+i*LZ1+j);
  IZTM12[i][j]=(DT+i*LZ1+j);
}
//NOTE: The splitting scheme has only one mesh
IGLLM(D,DT,ZGM21,ZGM11,LX2,LX1,LX2,LX1);
for(i=0;i<LX2;i++)for(j=0;j<LX2;j++)
{
  IXM21[i][j]=(D+i*LX2+j);
  IXTM21[i][j]=(DT+i*LX2+j);
}
IGLLM(D,DT,ZGM22,ZGM12,LY2,LY1,LY2,LY1);

```

```

for(i=0;i<LY1;i++)for(j=0;j<LY1;j++)
{
  IYM21[i][j]=(D+i*LY1+j);
  IYTM21[i][j]=(DT+i*LY1+j);
}
IGLLM(D,DT,ZGM23,ZGM13,LZ2,LZ1,LZ2,LZ1);
for(i=0;i<LZ2;i++)for(j=0;j<LZ1;j++)
{
  IZM21[i][j]=(D+i*LZ1+j);
  IZTM21[i][j]=(DT+i*LZ1+j);
}
//Compute interpolation operators for the geometry mesh M3
IGLLM(D,DT,ZGM11,ZGM31,LX1,LX3,LX1,LX3);
for(i=0;i<LX1;i++)for(j=0;j<LX1;j++)
{
  IXM13[i][j]=(D+i*LX1+j);
  IXTM13[i][j]=(DT+i*LX1+j);
}
IGLLM(D,DT,ZGM12,ZGM32,LY1,LY3,LY1,LY3);
for(i=0;i<LY1;i++)for(j=0;j<LY1;j++)
{
  IYM13[i][j]=(D+i*LY1+j);
  IYTM13[i][j]=(DT+i*LY1+j);
}
IGLLM(D,DT,ZGM13,ZGM33,LZ1,LZ3,LZ1,LZ3);
for(i=0;i<LZ3;i++)for(j=0;j<LZ1;j++)
{
  IZM13[i][j]=(D+i*LZ1+j);
  IZTM13[i][j]=(DT+i*LZ3+j);
}
IGLLM(D,DT,ZGM31,ZGM11,LX3,LX1,LX3,LX1);
for(i=0;i<LX1;i++)for(j=0;j<LX1;j++)
{
  IXM31[i][j]=(D+i*LX1+j);
  IXTM31[i][j]=(DT+i*LX1+j);
}
IGLLM(D,DT,ZGM32,ZGM12,LY3,LY1,LY3,LY1);
for(i=0;i<LY1;i++)for(j=0;j<LY1;j++)
{
  IYM31[i][j]=(D+i*LY1+j);
  IYTM31[i][j]=(DT+i*LY1+j);
}
IGLLM(D,DT,ZGM33,ZGM13,LZ3,LZ1,LZ3,LZ1);
for(i=0;i<LZ1;i++)for(j=0;j<LZ3;j++)
{
  IZM31[i][j]=(D+i*LZ3+j);
}

```

```

    IZTM31[i][j]=*(DT+i*LZ3+j);
  }
}

```

M. FORTIC

```

void FORTIC()
{
double PI=3.1415926536;
double VELT,VELTOT;
//Fortran function initial conditions
double AL=fabs(XM1[0][0][0]-XM1[LX1-1][0][LELT]);
int IEL,i,j,k;
double X,Y;
for(IEI=0;IEI<LELT;IEI++)for(i=0;i<LX1;i++)for(j=0;j<LY1;j++)
{
X=XM1[i][j][IEI];Y=YM1[i][j][IEI];
VX[i][j][IEI]=UO;VY[i][j][IEI]=VO;
VELTOT=VX[i][j][IEI]*VX[i][j][IEI]+VY[i][j][IEI]*VY[i][j][IEI];
TEMP[i][j][IEI]=TO;
RHO[i][j][IEI]=RO;
PR[i][j][IEI]=(GAM-1.0)*CV*RHO[i][j][IEI]*TEMP[i][j][IEI];
ENER[i][j][IEI]=RHO[i][j][IEI]*(CV*TEMP[i][j][IEI]+0.5*VELTOT);
//Now find non-dim values
VELT=pow(UO*UO+VO*VO,0.5);
AA=RO*VELT*VELT/(pow(RO,GAM));
RHO[i][j][IEI]=RHO[i][j][IEI]/RO;
PR[i][j][IEI]=RHO[i][j][IEI]/RO/VELT/VELT;
TEMP[i][j][IEI]=TEMP[i][j][IEI]/TA;
ENER[i][j][IEI]=ENER[i][j][IEI]/RO/VELT/VELT;
VY[i][j][IEI]=VY[i][j][IEI]/VELT;
VX[i][j][IEI]=VX[i][j][IEI]/VELT;
RXVEL[i][j][IEI]=VX[i][j][IEI]*RHO[i][j][IEI];
RYVEL[i][j][IEI]=VY[i][j][IEI]*RHO[i][j][IEI];
VISC[i][j][IEI]=1.0;
AMACH[i][j][IEI]=1.0/pow(GAM*(GAM-1.0)*TEMP[i][j][IEI],0.5);
}
}
}

```

N. DTDECIDE

```

void DTDECIDE(double DT,int ITER)
{
int i,j,k,IEL;
double CFL,VELMAX,VICOS,VELO,DIF;
if(ITER==0)GRIDSET(DZ);

```

```

//Choose according to CFL condition
VELMAX=-1000.0;
VICOS=2.0/REYN;
for(IEL=0;IEL<LELT;IEL++)for(i=0;i<LX1;i++)for(j=0;j<LY1;j++)
{
  VELO=pow(VX[i][j][IEL]*VX[i][j][IEL]+VY[i][j][IEL]*VY[i][j][IEL],0.5);
  VELO=VELO*(1.0+1.0/AMACH[i][j][IEL]);
  if(VELMAX<=VELO)VELMAX=VELO;
}
CFL=VELMAX*DT/DZ;
DIF=VICOS*DT/DZ/DZ;
printf("CFL,DIFF NUMBER =%f  %f\n",CFL,DIF);
}

```

O. POST

```

void POST(FILE* fp)
{
  int IEL,i,j,k;
  double VELTOT;
  for(IEL=0;IEL<LELT;IEL++)for(i=0;i<LX1;i++)
  for(j=0;j<LY1;j++)
  {
    //Turn off the energy equation
    VX[i][j][IEL]=RXVEL[i][j][IEL]/RHO[i][j][IEL];
    VY[i][j][IEL]=RYVEL[i][j][IEL]/RHO[i][j][IEL];
    VELTOT=pow(VX[i][j][IEL],2)+pow(VY[i][j][IEL],2);
    PR[i][j][IEL]=(GAM-1.0)*(ENER[i][j][IEL]-0.5*RHO[i][j][IEL]*VELTOT);
    TEMP[i][j][IEL]=(ENER[i][j][IEL]/RHO[i][j][IEL]-0.5*VELTOT);
    AMACH[i][j][IEL]=pow(VELTOT/(GAM*PR[i][j][IEL]/RHO[i][j][IEL]),0.5);
  }
}

```


BIBLIOGRAPHY

- [1] D. Gottlieb and S. A. Orszag, Numerical Analysis of Spectral Methods: Theory and Applications, SIAM-CMBS, 1977.
- [2] B. A. Szabo and I. Babuska, Finite Element Analysis, John Wiley & Sons, 1991.
- [3] C. Grossmann, H. G. Roos, and M. Stynes, Numerical treatment of partial differential equations, Springer Science & Business Media, 2007.
- [4] S. K. Lele, "Compact finite difference schemes with spectral-like resolution," *Journal of Computational Physics*, vol. 103, pp. 16-42, 1992.
- [5] W. Dai and R. Nassar, "A compact finite difference scheme for solving a one-dimensional heat transport equation at the microscale," *J. Computational and Applied Mathematics*, vol. 132, pp. 431-441, 2001.
- [6] D. Liu, W. Kuang and A. Tangborn, "High-order compact implicit difference methods for parabolic equations in Geodynamo simulation," *Advances in Mathematical Physics*, vol. 56, pp. 82-96, 2009.
- [7] J. W. Kim and D. J. Lee, "Optimized compact finite difference schemes with maximum resolution," *AIAA Journal*, vol. 34, pp. 887-893, 1996.
- [8] J. N. Reddy, An Introduction to The Finite Element Method (Third ed.), McGraw-Hill, 2006.
- [9] C. Johnson, Numerical Solution of Partial Differential Equations by the Finite Element Method, Dover, 2009
- [10] I. Babuska, "The finite element method with lagrangian multipliers," *Numerische Mathematik*, vol. 20, pp. 179-192, 1973.

- [11] F. Brezzi, "On the existence, uniqueness and approximation of saddle-point problems arising from Lagrangian multipliers," *R. A. I. R. O.*, vol. 8, pp. 129-151, 1974.
- [12] C. Canuto, M. Y. Hussaini, A. Quarteroni, and T. A. Zang Jr., *Spectral Methods in Fluid Dynamics*, Springer Science & Business Media, 2012.
- [13] A. T. Patera, "A spectral element method for fluid dynamics – Laminar flow in a channel expansion," *Journal of Computational Physics*, vol. 54, pp. 468-488, 1984.
- [14] Y. Maday and A. T. Patera, "Spectral element method for the incompressible Navier-Stokes equations," *IN: State-of-the-art surveys on computational mechanics (A90-47176 21-64)*. New York, American Society of Mechanical Engineers, 1989, p. 71-143. *Research supported by DARPA*, vol. 1, pp. 71-143, 1989.
- [15] G. Karniadakis and S. Sherwin, *Spectral / hp Element Methods for Computational Fluid Dynamics*, Oxford University Press, 2013.
- [16] S. Sherwin and G. Karniadakis, "A triangular spectral element method; applications to the incompressible Navier-Stokes equations", *Computer Methods in Applied Mechanics and Engineering*, vol. 123, pp. 189-229, 1995.
- [17] A. Beskok and T. Warburton, "An unstructured hp finite-element scheme for fluid flow and heat transfer in moving domain," *J. Comp. Phys.*, vol. 174, no. 2, pp. 492-509, 2002.

- [18] D. Liu, Q. Chen and Y. Wang, "Spectral element modeling of sediment transport in shear flows," *J. Comput. Methods Appl. Mech. Engrg.*, vol. 200, pp. 1691-1707, 2011.
- [19] D. Liu, Y. Zheng and Q. Chen, "Simulation of flow around rigid vegetation stems with a fast method of high accuracy," *Journal of Fluids and Structures*, vol. 63, pp. 1-15, 2016
- [20] G. E. Karniadakis, M. Israeli and S. A. Orszag, "High-order splitting methods for the incompressible Navier-Stokes equations," *Journal of Computational Physics*, vol. 97, pp. 414-443, 1991.
- [21] Y. Wang, Numerical Solution for Problems with Complex Physics in Complex Geometry, Louisiana Tech University, 2014.
- [22] R. J. LeVeque, Finite Volume Method for Hyperbolic Problems, Cambridge University Press, 2002.
- [23] B. Cockburn and C. Shu, The Runge-Kutta local projection P^1 -discontinuous-Galerkin finite element method for scalar conservation laws, IMA Preprint Series #388, University of Minnesota, 1988.
- [24] B. Cockburn and C. Shu, "TVB Runge-Kutta local projection discontinuous Galerkin finite element method for conservation laws II: General framework," *Mathematics of Computation*, vol. 52, pp. 411-435, 1989.
- [25] B. Cockburn, S. Lin and C. Shu, "TVB Runge-Kutta local projection discontinuous Galerkin finite element method for conservation laws III: one-dimensional systems," *Journal of Computational Physics*, vol. 84, pp. 90-113, 1989.

- [26] B. Cockburn, S. Hou and C. Shu, "The Runge-Kutta local projection discontinuous Galerkin finite element method for conservation laws IV: The multidimensional case," *Mathematics of Computation*, vol. 54, pp. 545-581, 1990.
- [27] B. Cockburn and C. Shu, "The Runge-Kutta discontinuous Galerkin method for conservation laws V: multidimensional systems," *Journal of Computational Physics*, vol. 141, pp. 199-224, 1998.
- [28] S. Sherwin and G. Karniadakis, "A triangular spectral element method: Applications to the incompressible Navier-Stokes equations," *Comp. Meth. Appl. Mech. Eng.*, vol. 123, pp. 189-229, 1995.
- [29] S. Sherwin and G. Karniadakis, "Tetrahedral hp finite element: Algorithms and flow simulations," *J. Comp. Phys.*, vol. 124, pp. 14-45, 1996.
- [30] S. J. Sherwin, T. C. Warburton and G. E. Karniadakis, "Spectral/hp methods for elliptic problems on hybrid grids," *Contemporary Mathematics*, vol. 218, pp. 191-215, 1998.
- [31] I. Lomtev, C. B. Quillen and G. E. Karniadakis, "Spectral/hp methods for viscous compressible flows on unstructured 2D meshes," *J. Comp. Phys.*, vol. 144, pp. 325-357, 1998
- [32] C. Pozrikidis, *Introduction to finite and spectral element method using MATLAB*, Taylor and Francis Group, 2005.
- [33] F. Fakhar-Izadi, "A spectral element method using the modal basis and its application in solving second-order nonlinear partial differential equations," *Mathematical Methods in the Applied Sciences*, vol. 38, pp. 478-504, 2015.

- [34] B. Cockburn, G. E. Karniadakis and C. Shu, The development of discontinuous Galerkin methods, Springer Berlin Heidelberg, 2000.
- [35] G. Chavent and B. Cockburn, "The local projection p_0 - p_1 discontinuous Galerkin finite element for scalar conservation laws," *M2AM*, vol. 23, pp. 565-592, 1989.
- [36] J. Qiu and C. Shu, "A comparison of troubled cell indicators for Runge-Kutta discontinuous Galerkin methods using WENO limiters," *SIAM J. Sci. Comput.*, vol. 27, pp. 995-1013, 2005.
- [37] J. S. Hesthaven and T. Warburton, Nodal discontinuous Galerkin methods: algorithms, analysis, and applications, Springer Science & Business Media, 2007.
- [38] J. H. Williamson, "Low-storage Runge-Kutta schemes," *Journal of Computational Physics*, vol. 35, pp. 48-56, 1980.
- [39] C. A. Kennedy, M. H. Carpenter and R. M. Lewis, "Low-storage, explicit Runge-Kutta schemes for the compressible Navier-Stokes equations," *Applied Numerical Mathematics*, vol. 35, pp. 177-219, 2000.
- [40] F. M. White, Fluid Mechanics, McGraw-Hill, 1999.
- [41] J. A. Dean, Large's handbook of chemistry, Mcgraw Hill Book Co., 1985.
- [42] G. M. Mala, D. Li and J. D. Dale, "Heat transfer and fluid flow in microchannels," *International Journal of Heat and Mass Transfer*, vol. 40, pp. 3079-3088, 1997.

- [43] C. Y. Lim, C. Shu, X. D. Niu and Y. T. Chew, "Application of lattice Boltzmann method to simulate microchannel flows," *Physics of Fluids*, vol. 14, pp. 2299-2308, 2002.
- [44] S. Colin, "Rarefaction and compressibility effects on steady and transient gas flows in microchannels," *Microfluidics and Nanofluidics*, vol. 1, pp. 268-279, 2005.
- [45] G. Karniadakis, A. Beskok, and N. Aluru, *Microflows and nanoflows: fundamentals and simulation*, New York: Springer-Verlag, 2001.
- [46] J. S. McCaskill, "Optically programming DNA computing in microflow reactors," *Biosystems*, vol. 59, pp. 125-138, 2001.
- [47] W. H. Grover and R. A. Mathies, "An integrated microfluidic processor for single nucleotide polymorphism-based DNA computing," *Lab on a Chip*, vol. 5, pp. 1033-1040, 2005.
- [48] E. Verpoote, B. Van Der Schoot and S. Jeanneret, "Three-dimensional micro flow manifolds for miniaturized chemical analysis systems," *Micromech. Microeng.*, vol. 4, pp. 246-246, 1994.
- [49] S. J. Haswell, "Development and Operating Characteristics of Micro Flow Injection Based on Electroosmotic Flow," *Analyst*, vol. 122, pp. 1-10, 1997.
- [50] H. Nakamura, Y. Yamaguchi, M. Miyazaki, H. Maeda, M. Uehara and P. Mulvaney, "Preparation of CdSe nanocrystals in a micro-flow-reactor," *Chemical Communications*, vol. 23, pp. 2844-2845, 2002.
- [51] F. F. Resuss, *Memoires de la Societe Imperiale de Naturalistes de Moscou*, Naturalistes De Moscou, 1809.

- [52] H. Helmholtz, "Studien uber electriche Grenzschichten," *Annalen der Physik*, vol. 243, pp. 337-382, 1879.
- [53] R. Feynman, R. Leighton and M. Sands, *The Feynman Lectures on Physics*, Addison-Wesley, 1977.
- [54] P. Dutta, A. Beskok and T. C. Warburton, "Electroosmotic Flow Control in Complex Microgeometries," *Journal of MicroelectroMechanical Systems*, vol. 11, pp. 36-44, 2002.
- [55] I. Borukhov, D. Andelman and H. Orland, "Adsorption of large ions from an electrolyte solution: a modified Poisson-Boltzmann equation," *Electrochimica Acta*, vol. 46, pp. 221-229, 2000.
- [56] F. Bianchi, R. Ferrigno and H. H. Girault, "Finite element simulation of an electroosmotic-driven flow division at a t-junction of microscale dimension," *Anal. Chem*, vol. 72, pp. 1987-1993, 2000.
- [57] M. J. Kim, A. Beskok and K. D. Kihm, "Electro-osmosis-driven micro-channel flows: A comparative study of microscopic particle image velocimetry measurements and numerical simulations," *Experiments in Fluids*, vol. 33, pp. 170-180, 2002.
- [58] R. F. Probstein, *Physicochemical hydrodynamics: an introduction*, John Wiley & Sons, 2005.
- [59] J. G. Santiago, "Electroosmotic flows in microchannels with finite inertial and pressure forces," *Anal. Chem.*, vol. 73, pp. 2353-2365, 2001.

- [60] D. Sinton, C. Escobedo-Canseco, L. Ren and D. Li, "Direct and Indirect Electroosmotic Flow Velocity Measurements in Microchannels," *Journal of Colloid and Interface Science*, vol. 254, pp. 184-189, 2002.
- [61] E. H. Kaplan and R. Heimer, "A model-based estimate of hiv infectivity via needle sharing," *Journal of Acquired Immune Deficiency Syndromes*, vol. 5, pp. 1116-1118, 1992.
- [62] S. Henry, D. V. McAllister, M. G. Allen, and M. R. Prausnitz, "Microfabricated microneedles: A novel approach to transdermal drug delivery," *Journal of Pharmaceutical Sciences*, vol. 87, pp. 922-925, 1998.
- [63] M. G. Allen, M. R. Prausnitz, D. V. McAllister, and F. P. M. Cros. Microneedle devices and methods of manufacture and use thereof, January 1 2002. US Patent 6,334,856.
- [64] A. J. C. Crespo and M. G. Gesteira, "User Guide for DualSPHysics code," *DualSPHysics v3.0*, pp. 1-89, 2013.
- [65] R. Pjanovic, N. Boskovic-Vragolovic, J. Veljkovic-Giga, R. Garic-Grulovic, S. Pejanovic, and B. Bugarski, "Diffusion of drugs from hydrogels and liposomes as drug carriers," *Journal of Chemical Technology and Biotechnology*, vol. 85, pp. 693-698, 2010.
- [66] G. M. T. Hare and J. C. S. Nga, "Density determination of local anaesthetic opioid mixtures for spinal anaesthesia," *Canadian Journal of Anaesthesia*, vol. 45, pp. 341-346, 1998.
- [67] J. L. Anderson, E. M. Elton, S. Pasyk, E. Patterson, A. B. Simon, W. E. Burmeister, B. R. Lucchesi, and B. Pitt, "Long-term intravenous infusion of

- antiarrhythmic drugs using a totally implanted drug delivery system,”
Canadian Journal of Anaesthesia, vol. 49, pp. 1954-1958, 1982.
- [68] Y. S. Choi, S. R. Hong, Y. M. Lee, K. W. Song, M. H. Park, and Y. S. Nam,
“Studies on gelatin-containing artificial skin: Ii. preparation and
characterization of cross-linked gelatin-hyaluronate sponge,” *Journal of
biomedical materials research*, vol. 48, pp. 631–639, 1999.
- [69] A. K. Datta, “Hydraulic permeability of food tissues,” *International Journal of Food
Properties*, vol. 9, pp. 767–780, 2006.
- [70] P. Dorian, D. Cass, B. Schwartz, R. Cooper, R. Gelaznikas, and A. Barr,
“Amiodarone as compared with lidocaine for shock-resistant ventricular
fibrillation,” *New England Journal of Medicine*, vol. 346, pp. 884–890, 2002.
- [71] R. Baddam, S. Engst, R. Meyer, and A. Rachakonda, “So many needles, so little
time: Modeling microneedle injection of anesthetics into human skin,” Project
Report, Cornell University, May 3, 2012.
- [72] G. R. Liu and M. B. Liu, *Smoothed particle hydrodynamics: A mesh-free particle
method*. Singapore: World Scientific., 2003.
- [73] J. J Monaghan, “An introduction to sph,” *Comp. Phys. Comm*, vol. 48, pp. 89-96,
1988.
- [74] D. Liu, Y. Wang, W. Ma and H. Zhang, “Mesh free gpu simulation of complex
flows in three dimensional distorting domain,” *International Journal of
Scientific and Innovative Mathematical Research*, vol. 3, pp. 6-17, 2015.
- [75] J. J Monaghan, “Simulating free surface flows with sph,” *J. Comp. Phys.*, vol. 110,
pp. 399-406, 1994.

- [76] J. J. Monaghan, "Smoothed particle hydrodynamics," *Rep. Prog. Phys.*, vol. 68, pp. 1703-1759, 2005.
- [77] J. J. Monaghan, "Smoothed particle hydrodynamics," *Annual Review of Astronomy and Astrophysics*, vol. 30, pp. 543-574, 1992.
- [78] J. P. Gray and J. J. Monaghan, "SPH elastic dynamics," *Comput. Methods Appl. Mech. Engrg.*, vol. 190, pp. 6641-6662, 2001.
- [79] H. Takeda, S. M. Miyama and M. Sekiya, "Numerical simulation of viscous flow by smoothed particle hydrodynamics," *Progress of Theoretical Physics*, vol. 92, pp. 939-960, 1994.
- [80] J. J. Monaghan and A. Kocharyan, "SPH simulation of multi-phase flow," *Computer Physics Communications*, vol. 87, pp. 225-235, 1995.
- [81] Y. Kim, J. Park and M. Prausnitz, "Microneedles for drug and vaccine delivery," *Advanced drug delivery reviews*, vol. 64, pp. 1547-1568, 2012.
- [82] K. Ita, "Transdermal delivery of drugs with microneedles potential and challenges," *Pharmaceutics*, vol. 7, pp. 90-105, 2015.
- [83] K. Ita, "Transdermal delivery of drugs with microneedles: Strategies and outcomes," *Journal of Drug Delivery Science and Technology*, vol. 29, pp. 16-23, 2015.
- [84] F. Bassi and S. Rebay, "A high-order accurate discontinuous finite element method for the numerical solution of the compressible Navier-Stokes equations," *Journal of Computational Physics*, vol. 131, pp. 267-279, 1997.
- [85] V. John, "Reference values for drag and lift of a two-dimensional time-dependent flow around a cylinder," *Int. J. Numer. Meth. Fluids*, vol. 44, pp. 777-788, 2004.